DEVELOPMENT OF A COMMERCIAL MODEL TO PREDICT STRESS CORROSION CRACKING GROWTH RATES IN OPERATING PIPELINES

Final Report
SwRI® Project 20.14080
Contract Number: DTPH 56-08-T-000001

Prepared for

U.S. Department of Transportation
Pipeline Hazardous Materials Safety Administration
400 Seventh Street, SW, Room 2103
Washington, DC 20590

Prepared by

Frank Song,[1] Baotong Lu,[1] Ming Gao[2] and Mimoun Elboujdaini[3]

[1] Southwest Research Institute®
6220 Culebra Road
San Antonio, TX 78238

[2] Blade Energy Partners
16225 Park Ten Place, Suite 450
Houston, TX 77084

[3] CANMET Materials Technology Laboratory
Natural Resources Canada – Government of Canada
568 Booth Street, Ottawa, Ontario K1A 0G1

June 2011

SOUTHWEST RESEARCH INSTITUTE®
SAN ANTONIO HOUSTON WASHINGTON, DC

DEVELOPMENT OF A COMMERCIAL MODEL TO PREDICT STRESS CORROSION CRACKING GROWTH RATES IN OPERATING PIPELINES

Final Report
SwRI® Project 20.14080
Contract Number: DTPH 56-08-T-000001

Prepared for

U.S. Department of Transportation
Pipeline Hazardous Materials Safety Administration
400 Seventh Street, SW, Room 2103
Washington, DC 20590

Prepared by

Frank Song,[1] Baotong Lu,[1] Ming Gao[2] and Mimoun Elboujdaini[3]

[1] Southwest Research Institute®
6220 Culebra Road
San Antonio, TX 78238

[2] Blade Energy Partners
16225 Park Ten Place, Suite 450
Houston, TX 77084

[3] CANMET Materials Technology Laboratory
Natural Resources Canada – Government of Canada
568 Booth Street, Ottawa, Ontario K1A 0G1

2011

APPROVED:

David Ferrill, Director
Department of Earth, Material and Planetary Sciences
Southwest Research Institute

EXECUTIVE SUMMARY

Background and Objective

Stress corrosion cracking (SCC) of buried pipelines is often categorized into two types: classic or intergranular cracking, which occurs in high pH solution near cracks in coating disbonded regions, and transgranular cracking, which occurs in near-neutral pH solution in coating disbonded regions. High pH SCC results from periodic passive film rupture and anodic dissolution, and the crack growth rate (CGR) follows Faraday's law. In contrast, near-neutral pH SCC is less well understood, although atomic hydrogen charged in the steel by corrosion reactions has been shown to play a significant role. Near-neutral pH SCC is often regarded as corrosion fatigue because constant loading rarely leads to crack growth.

CGR is a critical parameter that must be considered when the inspection interval for in-line inspection or pressure testing or the reassessment interval for SCC direct assessment (DA) is to be determined. CGR can also be a key parameter in identifying locations along a pipeline that must be given priority for SCC assessment.

The current industrial practice of estimating CGRs is based on empirical approaches, mainly relying on linear extrapolation from measured crack depth(s) over a period of time or using a conservative fixed value. Such CGR estimation that excludes the underlying cracking mechanisms can be fraught with uncertainties. This is because the often nonlinear physical crack growth is not reflected in such a method. A CGR model with embedded crack growth mechanisms is needed to more reliably predict CGR.

The main objective of this project was to develop commercial models for predicting CGRs in operating pipelines useful for prioritization of SCC susceptible locations and for establishing inspection or re-assessment intervals. For high pH SCC, the CGR models were developed based on fundamental principles and then reduced to a commercial tool suitable for practical application. Because the mechanisms of near-neutral pH SCC were not well established, the model developed in this work for this type of SCC still relied on empirical correlations of experimental data reported in the literature. Procedures for field application of the models were provided.

CGR Model for High pH SCC

Southwest Research Institute® (SwRI®) developed a comprehensive fundamental model capable of predicting the evolution of in-crack chemistry and CGRs under high pH SCC conditions. A critical review of this model led to the crack tip strain rate (CTSR) expression being modified. Extensive computations followed to investigate the effect of in-crack mass transport on CGRs when the bulk solution chemistry was a concentrated carbonate and bicarbonate buffer. Within the known range of field CGRs, mass transport was not found to be a controlling step, and thus it was neglected in the model development. Faraday's law was used as the basis for developing the CGR model. The CGR model was developed under two loading conditions: constant and cyclic loads. CTSR is a key parameter used in the CGR model.

For constant loading, two CTSR expressions in the literature were examined and each expression contains two time-dependent terms. Under practical conditions of pipe operation, one term in each of the expressions was found to be significantly greater than the other term. By using only the dominant term, the results obtained from the two expressions were similar, and consequently one of the CTSR expressions was used for the model.

For cyclic loading, several CTSR expressions exist in the literature, while only one was developed with experimental confirmation. This expression was adopted in the CGR model for cyclic loading.

Results of the CGR models developed for both constant and cyclic loading conditions were compared with experimental data under the same conditions, and agreement was shown. This suggests that the models can correctly predict the trends of CGRs; if calibrated with field data, the models can be used to predict field CGRs.

CGR Model for Near-Neutral pH SCC

For near-neutral pH SCC, an empirical model reported in the literature, which was built on extensive laboratory data, was used as the basis for the model developed in this work. This model does not effectively incorporate the obvious effect of the environment when used for predicting CGRs. This environmental effect due to the solution pH and external potential at the crack mouth was included in the model developed in this work. This work also developed procedures for field application of the model.

Procedures for Field Application of the CGR Models

A four-step procedure was developed for field applications using the CGR models developed in this work. The first step is data collection and a feasibility study to determine whether the CGR models are applicable to the conditions for prediction and whether sufficient data are available for making CGR predictions. If the models are determined to be feasible, the second step is determining the model parameters from the data collected and the actual application of the models for CGR prediction given the field conditions. A possible third step is a reality check of model predictions versus known prior CGRs or field experience, which provides suggestions for improvement of the model. The fourth step is an overall evaluation of all CGRs obtained from this and other methods (e.g., linear extrapolation or a conservative fixed rate) and making decisions on the actual CGR to be used for specific applications.

Even though the procedures developed for field application of the CGR models are straightforward, examples were provided to show how each step can be best implemented.

Conclusions

- CGR models and field procedures were developed and examples were provided to show how the models can be used for predicting field CGRs under both high pH and near-neutral pH SCC conditions.

- The high pH SCC CGR models were built on fundamental principles, and consistency between model predictions and experimental data was shown. This consistency verifies that the models are capable of predicting the trends of high pH SCC CGRs and can be used for field application once calibrated with field data.

- For high pH SCC, two CGR models were developed corresponding respectively to constant loading and cyclic loading.

- The current high pH SCC CGR model was developed assuming the chemistry at the crack mouth is known. Such chemistry in a coating disbonded region can be extremely difficult to measure in the field, and it can be very different from soil chemistry, which is easily determined. This, however, does not affect field application of the model, because this environmental effect has been implicitly embedded in the model parameters determined from field data. The field data include the past experiences of the crack.

- The near-neutral pH SCC CGR model was developed by expanding a prior empirical CGR model in the literature to further account for the effect of the external environment at the crack mouth on CGRs.

- A live on-line workshop was held by PHMSA in June 2011 open to the entire pipeline industry. The aim was to make the widest possible transfer of the technologies developed in this work to the pipeline industry.

Recommendations

- Collect and analyze field data from the pipeline industry for further model validation.

- Develop and perform critical experiments to generate high quality data to validate the current models and improve the industry's understanding of cracking mechanisms.

- Extend the current CGR model to include the specific effect of soil chemistry on CGRs.

- Improve the model for near-neutral pH SCC to include physical mechanisms of crack growth similar to the high pH SCC CGR model.

ACKNOWLEDGMENTS

The project was conducted under the Department of Transportation (DOT) Contract DTPH 56-08-T-000001.

Vincent Holohan and James Merritt of PHMSA/DOT provided management oversight for this project. This work was cosponsored by CANMET Materials Laboratory of the Natural Resources of Canada (Winston Revie), Williams Pipeline Company (Sergio Limon), and TransCanada Pipeline Company (Richard Kania and Robert Worthingham).

The project also benefited from the preliminary input of Dr. Raymond R. Fessler of BIZTEK Consulting, Inc.. Dr. Hui Yu of SwRI provided input. Technical review of this report by Dr. Lietai Yang of SwRI is appreciated.

TABLE OF CONTENTS

TABLE OF CONTENTS (CONTINUED)

LIST OF FIGURES

LIST OF TABLES

1.0 GENERAL INTRODUCTION

1.1 Background

Stress corrosion cracking (SCC) in pipelines occurs under two broad pH conditions—alkaline pH and near-neutral pH [1]. SCC can lead to leaks, sudden bursts, or explosions of gas and liquid pipelines [1-2]. Crack growth rate (CGR) is a critical parameter to be considered when the inspection interval for in-line inspection (ILI) or pressure test, or the reassessment interval for SCC direct assessment (DA) is determined. CGR can also be a key parameter in identifying locations along a pipeline that must be given priority for SCC assessment.

The current industrial practice of estimating CGRs is based on empirical approaches, such as assuming a conservative constant rate or a rate obtained through linear extrapolation from measured crack depth(s) over a period of time [2-4]. Such CGR estimation without including the underlying cracking mechanisms can be fraught with uncertainties. This is because the often non-linear nature of the physical growth of a crack is not reflected in such a method. A CGR model with the crack growth mechanisms embedded is needed for more reliable CGR prediction.

1.2 Objectives and Approach

The main objective of this project was to develop CGR models that would be based on fundamental principles and then reduced to a tool suitable for practical application. The models will be useful for prioritization of SCC susceptible locations and for establishing inspection or re-assessment intervals.

Four tasks were proposed to accomplish the goal.

Task 1 was proposed to be a literature review and development of a fundamental SCC model. The original purpose was to develop a model that would use the known soil chemistry and pipeline operating conditions as the model input to predict the chemistries inside and outside of a crack and the CGR.

For high pH SCC, the model was proposed to be built on a prior model developed earlier in a project funded internally by Southwest Research Institute® (SwRI®) [5]. This earlier model assumes a known and stable chemistry at the crack mouth and predicts the CGR and in-crack chemistry.

An examination of the earlier SwRI SCC model [6] found that the crack tip strain rate (CTSR) expression used may be more appropriately replaced with an alternative (shown in Section 2.0). After this replacement of CTSR expression, by using the initial crack chemistry as the 1N-1N carbonate-bicarbonate solution (a frequently used solution in high pH SCC tests), a series of computations was performed using the SwRI SCC model. The predicted CGRs and in-crack chemistries were examined. Within a large range of CGRs practical for the pipeline industry, the predicted chemistry within the crack did not vary appreciably as the crack grew. For such a concentrated, buffered chemistry, a much larger CGR (discussed in Section 2.0) is

required to alter the crack chemistry. Only at high CGRs sufficient corrosion species can be quickly generated to overbalance the mass transport and modify the solution chemistry at the crack tip.

Based on these results, the focus of this work on developing the high pH SCC model was shifted by ignoring the effect of in-crack chemistry on CGR. For the model of near-neutral pH SCC, because the crack growth can be significantly affected by interstitial hydrogen in steel, the hydrogen effect is included.

Task 2 was collection and analysis of full-scale laboratory test and field data. In addition, small-scale laboratory data were collected and analyzed when possible. Although the majority of the field data were not directly useful because of the lack of information required for model validation, the relevant data were selected and used for calibrating the model.

Task 3 was model validation, or a comparison of the model results with experimental data. The small-scale laboratory data were most useful with the test conditions best informed. However, full-scale laboratory test data selected in Task 2 were also used for the model.

Task 4 was simplification of the model for developing tools or guidelines for use in field applications. This was accomplished by understanding the data that can be available in the field. This type of data was specifically used as model input variables for predicting CGRs. Simple procedures were developed for the users to conveniently utilize the model.

1.3 Outline of the Report

Because the crack growth of high pH SCC and near-neutral pH SCC follows significantly different mechanisms, two separate models were developed to address these two types of SCC. Chapter 2 describes the model for high pH SCC, and Chapter 3 describes the near-neutral pH SCC model. Chapter 4 describes suggested procedures for field application of the models. Conclusions and recommendations are provided in Chapter 5.

1.4 References

1. Regulatory Support Office, National Energy Board, Stress Corrosion Cracking on Canadian Oil and Gas Pipelines, Report of the Inquiry, MH-2-95, November 1996.
2. R.R. Fessler, Research Needs on SCC of Pipelines, Presentation at DOT/RSPA, Houston, TX, December 2, 2003.
3. B.N. Leis, R.N. Parkins, Modeling Stress-corrosion Cracking of High-pressure Gas Pipelines, in: Eighth Symposium on Line Pipe Research, AGA Catalog No. L51680, 1993, 19.1-19.21.
4. T.M. Ahmed, S.B. Lambert, R. Sutherby, A. Plumtree, Corrosion 53 (7), 1997, 581-590.
5. F.M. Song, Predicting Crack Growth Rates in Pipelines for Prioritization of Stress Corrosion Cracking Locations," SwRI internal project R9639, March 2008.
6. F.M. Song, Predicting the Mechanisms and Crack Growth Rates of Pipelines Undergoing Stress Corrosion Cracking at High pH, Corrosion Science, 51, 2009, 2657-2674.

2.0 HIGH pH SCC MODELING

2.1 Technical Background and Objectives

It is well-known that the growth of stress corrosion cracks in buried pipelines at high pH follows the film rupture and anodic dissolution mechanism. SCC is caused by interactions of tensile loading, a corrosive environment, and a material susceptible to SCC in the corrosive media. These interactions are illustrated in Figure 2-1. The material-environment interactions are reflected by the cracking kinetics. The cracking kinetics can be determined by the transient anodic dissolution current density from a bare metal surface, the repassivation kinetics to repair or form the passive film after rupture, and the fracture ductility of the film. The material response to the mechanical force is reflected by the CTSR as a function of external loading, the mechanical properties of the material, and the crack geometry. The bulk stress intensity factor (SIF) is often used to describe the stress/strain field near the crack tip that controls the CTSR.

In predicting CGR, the CTSR is a frequently used key parameter. It characterizes the interactions of film repassivation kinetics, loading condition, and material properties. Following Faraday's law, the following equation can be derived:

$$\dot{a} \approx A\dot{\varepsilon}_{ct}^{n} \tag{2-1}$$

This derivation is presented in Appendix 2.A[1-5]. In Equation (2-1), $\dot{a}$, $\dot{\varepsilon}_{ct}$, and n are CGR, CTSR, and the film repassivation kinetic exponent, respectively. $A = \frac{\dot{a}^*}{1-n}\left(\frac{t_0}{\varepsilon_f}\right)^n = \frac{i_a^*}{1-n}\frac{M}{zF\rho}\left(\frac{t_0}{\varepsilon_f}\right)^n$, in which ε_f is film rupture strain; $\dot{a}^*$ and i_a^* are the CGR and anodic current density, respectively, when the metal surface is bare without a film; t_0 is incubation time before a fresh metal surface starts to repassivate; M is atomic weight of the metal; z is valency of solvated metal species; F is Faraday's constant; and ρ is the density of the metal.

Equation (2-1) has been used [6-7] to predict pipeline CGRs at high pH under constant loading. The CTSR used includes the one Shoji et al.[8] proposed.

$$\dot{\varepsilon}_{ct} = \left(2\frac{\dot{K}}{K} + \frac{\dot{a}}{r_0}\right)\frac{N^*}{N^*-1}\frac{\beta\sigma_y}{E}\left\{ln\left[\frac{\lambda}{r_0}\left(\frac{K}{\sigma_y}\right)^2\right]\right\}^{\frac{1}{N^*-1}} \tag{2-2}$$

In Equation (2-2), K and $\dot{K}$ are SIF and its derivative over time t, respectively. The definition and mathematical expression of K are given in Appendix 2.B[9-10] r_0 is specific length representing the size of plastic process zone around the crack tip, E is Young's modulus, β is Rice's coefficient, and σ_y is the steel yield strength. For the plane strain condition, $\lambda = \frac{1}{3\pi}$. The parameter N^* is a strain hardening exponent determined by the following power law:

$$\frac{\varepsilon}{\varepsilon_y} = \frac{\sigma}{\sigma_y} + \alpha^*\left(\frac{\sigma-\sigma_y}{\sigma_y}\right)^{N^*} \tag{2-3}$$

where ε and ε_y are strain and yield strain, respectively and σ is tensile stress. α^* is a strain hardening coefficient following Equation (2-3).

In using Equation (2-2), these researchers [6-7] mistreated the parameter N^* as the conventional strain hardening exponent *N* following the Ramberg-Osgood law:

$$\frac{\varepsilon}{\varepsilon_y} = \frac{\sigma}{\sigma_y} + \alpha\left(\frac{\sigma}{\sigma_y}\right)^N \tag{2-4}$$

where α is the conventional strain hardening coefficient and N is the conventional strain hardening exponent.

Comparing Equations (2-3) and (2-4) clearly shows that although N^* is related to N, they can have significantly different values. As an example, for steel, N=6 and N^*=1.6. This has been clearly shown by Shoji et al. in their latest paper [11].

The basis that Shoji [8] used to derive Equation (2-2) is the work of Gao and Hwang[12], while Hall [13] believes that the Hutchinson-Rice-Rosengren (HRR) equation better describes the dependence of CTSR on *K*. After a review of CTSR expressions published in the literature, Hall [13] presented the following alternative CTSR expression, with the aid of a later work published by Gao et al. [14]:

$$\dot{\varepsilon}_{ct} = \frac{2N}{1+N}\frac{\sigma_y}{E}\left(\frac{pK^2}{r_0\sigma_y^2}\right)^{\frac{N}{N+1}}\frac{\dot{K}}{K} + \frac{2\beta N}{N-1}\frac{\sigma_y}{E}\frac{\dot{a}}{r_0}\left\{ln\left[\frac{\lambda}{r_0}\left(\frac{K}{\sigma_y}\right)^2\right]\right\}^{\frac{N+1}{N-1}} \tag{2-5}$$

where $p = \frac{1}{I_n \alpha^{\frac{1}{N+1}}}$ if derived directly from the HRR equation and I_n is a constant depending on the strain hardening exponent. When N≈6, close to the strain hardening exponent of pipeline steels, I_n≈4.9 [15]. Note that Hall's derivation [13] missed the factor of "2" in the far right term of Equation (2-5).

Because Equation (2-5) has never been used in pipeline SCC models, it would be interesting to examine how Hall's equation is compared to that of the Shoji et al. predictions and how much the predictions deviate from each other.

In the SCC modeling for pipelines, when Equation (2-3) is used for CGR prediction, the parameter *N** in Equation (2-2) has not been properly applied. A literature review showed that no mechanistic CGR models have considered the effect of cyclic loading on pipeline high pH SCC, although the cyclic nature of loading can contribute to CGR. An objective of this project for high pH SCC is to develop a model that can predict CGRs in both constant and cyclic loading conditions. Methods for applying the model in the field will be provided in Sections 4.1 and 4.2.

2.2 High pH SCC CGR Model

The CGR model used for pipeline high pH SCC is not new; it still can be represented by Equation (2-1). Nevertheless, more appropriate CTSR expressions are used here and are further examined. These CTSR expressions can develop more detailed CGR expressions for constant and cyclic loading conditions.

2.2.1 CGR Equation Under Constant Loading

The CTSR expressions that are useful in this project for high pH SCC are Equations (2-2) and (2-5). Both equations consist of two terms, $(\frac{\dot{K}}{K})$ and $(\frac{\dot{a}}{r_0})$, resulting from the time derivatives of *K* and *r*. By using nominal values for pipelines, the magnitude of the two terms in the previous equations is compared in Appendix 2.C [8,11,13]. For both equations, the term resulting from the time derivative of r is clearly much greater than the term from the time derivative of K, and thus the term associated with the time derivative of K can be neglected.

By neglecting the term resulting from the time derivative of K, Equations (2-2) and (2-5) become, respectively,

$$\dot{\varepsilon}_{ct} = \frac{\dot{a}}{r_0}\frac{N^*}{N^*-1}\frac{\beta\sigma_y}{E}\left\{ln\left[\frac{\lambda}{r_0}\left(\frac{K}{\sigma_y}\right)^2\right]\right\}^{\frac{1}{N^*-1}} \tag{2-6a}$$

and

$$\dot{\varepsilon}_{ct} \approx \frac{\dot{a}}{r_0}\frac{2N}{N-1}\frac{\beta\sigma_y}{E}\left\{ln\left[\frac{\lambda}{r_0}\left(\frac{K}{\sigma_y}\right)^2\right]\right\}^{\frac{N+1}{N-1}} \tag{2-6b}$$

The only difference between Equations (2-6a) and (2-6b) is their exponents $[1/(N^*-1)$ vs. $(N+1)/(N-1)]$ and a term in their coefficients $[N^*/(N^*-1)$ vs. $2N/(N-1)]$. For steel with $N^* \approx 1.6$ and $N \approx 6$, the ratio of the two exponents is 1.67:1.4 and of the two coefficients is 2.67:2.4. The closeness to unity of the two ratios suggests that the two CTSR equations are quite close. Therefore, in the CGR modeling for high pH SCC, Equation (2-6b) is chosen and consistently used because the N value is commonly reported in the literature.

It is well known that there is a threshold for crack growth (K_{ISCC}). When $K \le K_{ISCC}$, it is possible that $\dot{a} \to 0$. Then, $\dot{\varepsilon}_{ct} \to 0$. By taking out the threshold from the SIF, Equation (2-6b) may be formulated as

$$\dot{\varepsilon}_{ct} \approx \frac{\dot{a}}{r_0}\frac{2N}{N-1}\frac{\beta\sigma_y}{E}\left[ln\left(\frac{\lambda(K_I^2-K_{ISCC}^2)}{r_0\sigma_y^2}\right)\right]^{\frac{N+1}{N-1}} \tag{2-7}$$

Substitution of Equation (2-7) into Equation (2-1) and reorganization yield

$$\dot{a}_s = A^{\frac{1}{1-n}}\left\{\frac{2N}{N-1}\frac{\beta\sigma_y}{E}\frac{1}{r_0}\left[ln\left(\frac{\lambda(K_I^2-K_{ISCC}^2)}{r_0\sigma_y^2}\right)\right]^{\frac{N+1}{N-1}}\right\}^{\frac{n}{1-n}} \quad (2\text{-}8)$$

Equation (2-8) is the CGR equation used in this work for constant loading.

2.2.2 Crack Growth Rate Equation Under Cyclic Loading

A number of expressions for CTSR exist [16]. A review of the expressions found that the equation of Lidbury [16] has experimental confirmation [17], and it was chosen in this project for treating high pH SCC modeling under cyclic loading:

$$\dot{\varepsilon}_{ct} = \varepsilon_0 f \Delta K^2 = \varepsilon_0 f (1-R)^2 K_{max}^2 = \xi K_{max}^2 \quad (2\text{-}9)$$

where it is defined that $\xi = \varepsilon_0 f (1-R)^2$.

After the threshold SIF is included following the rationale given in Appendix 2.D [16,18-22], Equation (2-9) becomes

$$\dot{\varepsilon}_{ct} = \xi(K_{max}^2 - K_{ISCC}^2) \quad (2\text{-}10)$$

Substitute Equation (2-8) into Equation (2-1) to yield

$$\dot{a}_c = \frac{da_c}{dt} = A\xi^n(K_{max}^2 - K_{ISCC}^2)^n \quad (2\text{-}11)$$

Equation (2-11) can be treated as the CGR model for high pH SCC when the CGR is controlled by cyclic loading.

2.2.3 Generalized CGR Model Under Constant and Cyclic Loading

An overall CTSR may be considered as the linear superposition of the two CTSRs under constant and cyclic loadings. This leads to

$$\dot{\varepsilon}_{ct} \approx \frac{\dot{a}}{r_0}\frac{2N}{N-1}\frac{\beta\sigma_y}{E}\left[ln\left(\frac{\lambda(K_{max}^2-K_{ISCC}^2)}{r_0\sigma_y^2}\right)\right]^{\frac{N+1}{N-1}} + \xi(K_{max}^2 - K_{ISCC}^2) \quad (2\text{-}12)$$

Substitute Equation (2-12) into Equation (2-1) to yield the overall CGR expression as

$$\dot{a} = A\left\{\frac{\dot{a}}{r_0}\frac{2N}{N-1}\frac{\beta\sigma_y}{E}\left[ln\left(\frac{\lambda(K_{max}^2-K_{ISCC}^2)}{r_0\sigma_y^2}\right)\right]^{\frac{N+1}{N-1}} + \xi(K_{max}^2 - K_{ISCC}^2)\right\}^n \quad (2\text{-}13)$$

Because $\dot{a}$ is also presented in Equation (2-13) to the right of the equal sign, an analytical solution can be possible when n is ½ and 2/3. When needed, an iteration method may be used to obtain the solution for $\dot{a}$.

2.3 Comparison of Model Predictions with Available Experimental Data

Limited experimental data are available and are compared with results obtained from the CGR models. The values of the model parameters were carefully chosen from the literature and listed in Table 2-1.

In Table 2-1, the repassivation kinetic exponent was determined based on experimental data Song [4] reported, and $n = 2/3 \approx 0.667$ is used. This value was taken based on the results measured at different strain rates, temperatures, and controlled potentials. Specimens used in the tests were made from pipeline steel and tested in 1N-1N carbonate and bicarbonate solution.

Parkins [1,6] suggests the relation between anodic current density and the electrochemical potential can be evaluated by polarization curves. For high pH SCC, the passive film may be considered to form on the electrode surface during the anodic polarization in the potential range where the active-to-passive transition takes place. To estimate the anodic current density over the metal surface in the potential range where the active-to-passive transition occurs, Parkins [1,6] suggested using the polarization curve measured with the potential scanning rate of 1 V/min to obtain the relatively film-free surface. Parkins [2] reported a good correlation between the anodic current densities determined by the potential scanning rate 1 V/min and the CGR in carbon steels caused by the intergranular SCC.

Figure 2-2 shows a typical polarization curve of pipeline steel in the 1N-1N carbonate and bicarbonate solution at 75 $^{\circ}$C reported by Parkins [2]. It can be seen that the anodic current density on the metal surface reaches its maximum at a potential around -0.725V vs. saturated $Cu/CuSO_4$ electrode (CSE). Slow strain rate tests suggest that at this potential, pipeline steel displays its maximum susceptibility to intergranular SCC [2]. A comparison of the polarization curves obtained by the fast potential scanning (1 V/min) reported by different researchers shows that the shapes of the polarization curves are quite similar and the peak anodic current density is generally located at the potential around $-0.725V_{CSE}$, while the values of the peak current densities vary in the range from 140 ~ 700 A/m^2 [6-7,21].

2.3.1 Model Predictions vs. Experimental Data for SCC Under Constant Loading

The anodic current density over the bare metal surface at the crack tip i_a^*, which is embedded in the variable "A" in Equation (2-8), is a function of electrochemical potential that can be affected by the solution chemistry and temperature. At the crack tip, it is dominated by the local solution chemistry and potential which, in turn, is controlled by the potential at the crack mouth, the chemical and electrochemical reactions, and mass transport within the crack. Numerical simulations conducted in this program by using an earlier software code for high pH SCC prediction [4] showed that with 1N-1N carbonate-bicarbonate solution as the bulk, the solution chemistry within the crack during crack propagation is negligible if the CGR is below 10^{-9} m/s (see Appendix 2.E[4]). Therefore, with the understanding that CGRs for high pH SCC

detected in the field fall below 10^{-11} m/s, the effect of mass transfer and potential drop within a crack for high pH SCC is neglected.

When the anodic current density at the fresh steel surface is chosen as the peak current density on the anodic polarization curve in Figure 2-2, it is approximately 400 A/m^2. Because the peak current density measured by different researchers [6-7,21] varies from 140-700 A/m^2, four current densities in this range were used for predicting CGRs and the predicted results are shown in Figure 2-3. It is clear that the magnitude of the peak anodic current density can have a significant effect on the predicted CGR. When the peak current density is 700 A/m^2, the predicted CGRs are comparable with the CGR data Parkins [21] reported.

The experimental data of Parkins and Greenwell [21] were obtained by using the same solution, same temperature and same constant loading condition. The consistency between the predicted CGRs and those experimentally measured suggests that Equation (2-8) can be used to predict the trends of CGRs.

2.3.2 Predictions vs. Experimental Data for SCC Under Cyclic Loading

For a growing crack under cyclic loading, the contributions of both crack tip advance and cyclic loading to the CTSR should be considered. Equation (2-13) is used to predict CGRs compared to a set of experimental data obtained under consistent conditions. A sensitivity analysis is provided later to compare the deviation between Equations (2-11) and (2-13).

Using parameters in Table 2-1, the predicted CGRs are shown in Figure 2-4. The experimental data obtained under cyclic loading conditions Pilkey et al. [22] reported are also shown. A comparison of predicted CGRs obtained from Equation (2-13) and experimental data shows consistencies between them. In the CGR prediction, K_{ISCC} = 25MPam$^{1/2}$ reported by the authors was used. The peak anodic current density of the polarization curve at -0.725V$_{CSE}$ is assumed here to be 200 A/m^2, which falls in the range of peak anodic current densities measured by the potentiodynamic experiments [6-7,21].

2.4 Sensitivity Analysis of the Model

2.4.1 Potential and Anodic Current Density at the Bare Steel Surface

For high pH SCC under cyclic loading, SCC and loading fluctuation contribute to CGR, and their relative significance is analyzed with the aid of a polarization curve (peak current density at 200 A/m^2) [2], assuming K_{max}=30 MPam$^{0.5}$ and ξ=3×10^{-8} (MPa)$^{-2}$m^{-1} where $\xi = f\varepsilon_0(1-R)^2$. This comparison is shown in Figure 2-5, where the red solid line represents the combined CGR under cyclic loading ($\dot{a} = \frac{da}{dt}$) from Equation (2-13), the broken blue line stands for the CGR under constant loading only [$\dot{a}_s = da/dt_{(s)}$ from Equation (2-8)], and the green line is the component of CGR by loading fluctuation only [$\dot{a}_c = da/dt_{(c)}$ from Equation (2-11)]. With the embedded simple relation between CGR and electrode potential, which is assumed to follow the polarization curve irrespective of the loading being steady or cyclic, the predicted CGRs under all three conditions follow the same pattern as the polarization curve. However,

their magnitudes are smaller than rates converted from the polarization curve due to passivity of the steel surface.

Figure 2-6(a) is a log-log plot to show the relation between normalized CGRs under constant and cyclic loading vs. the upper limit CGR: $\dot{a}^* = i_a^* M/zF\rho$, ceiling CGR. Regardless of the loading type, the maximum normalized CGR is unity by definition. The normalized cyclic CGR $\dot{a}_c/\dot{a}^*$ is shown as a group of horizontal lines, and the distance between adjacent lines represents the ratio of ξ^n, which characterizes the dependence of CTSR on cyclic loading. The line representing $\dot{a}_s/\dot{a}^*$ is a straight line with a slope of $n/(1-n)$ following Equation (2-8). For a given $\dot{a}^*$, which is controlled by the corrosivity of the solution at the crack tip and temperature, this line of $\dot{a}_s/\dot{a}^*$ separates the chart into two regions. Above this line, cyclic loading. Below this line, the constant loading portion mainly contributed to CGR. This is more clearly demonstrated in Figure 2-6(b).

In Figure 2-6(b), the two lines representing $\dot{a} = 2\times10^{-12}$ m/s and $\dot{a} = 2\times10^{-11}$ m/s are depicted. The former corresponds to the crack growth life around 50 years [i.e., a crack will take 50 years to penetrate 50% thickness of pipe wall (w = 0.375"≈ 10 mm)], and the latter will stand for the 5-year crack growth life. The average crack velocities observed in the field often fall between these two values. The two shaded regions illustrate which portion of the cyclic load (constant portion or loading fluctuations) more dominates the CGRs. In the upper left portion, the CGR is low when the crack tip surface is bare. This can results from a benign local solution or low temperature. In this condition, the crack tip is more readily passivated and the cyclic loading is more dominate. In contrast, in the lower-right region, the bare surface CGR is higher due to a more aggressive solution or a higher temperature. The crack tip may not be readily passivated, and the CGR due to constant loading is more dominant.

Figure 2-6(b) shows that in the practical range of CGRs, the contribution of the cyclic load can be ignored for service life prediction when $\xi<3\times10^{-10}$ MPa^{-2}m^{-1}s, or as an example, when R>0.9 and f<2×10^{-4} Hz. This condition is often observed for gas pipelines [23]. However, for pipelines transporting liquids, the R ratio can be as low as 0.6 and the loading frequency may be greater than 10^{-3} Hz, corresponding to $\xi \geq 3\times10^{-8}$ MPa^{-2}m^{-1}s. In this case, cyclic loading may dominate the CGR.

2.4.2 Generalized Crack Growth Rate Model vs. Superposition Model

Equation (2-13) may be compared with the superposition model. By the latter model, the overall CGR under cyclic loading $\dot{a}$ should be approximated by the CGR due to constant loading $\dot{a}_s$ and that resulting from fluctuation of the loading $\dot{a}_c$, or

$$\dot{a} \approx \dot{a}_s + \dot{a}_c \tag{2-14}$$

Figure 2-6(a) shows that the previous approximation is valid because the data calculated from the right side of Equation (2-9) (shown by empty circles) are close to the curves obtained from Equation (2-13). A more general analysis for the validity of Equation (2-14) is provided in Appendix 2.F.

In Appendix 2.F the maximum error of Equation (2-14) can be shown theoretically to occur at $\dot{a}_s = \dot{a}_c$. Shown in Figure 2-6, the maximum errors are located where the horizontal lines and the straight line of $\dot{a}_s/\dot{a}^*$ meet. The maximum error depends on the repassivation kinetic exponent "n." At n=0.667, the maximum error calculated by $(\frac{\dot{a}_s+\dot{a}_c}{\dot{a}} - 1) \times 100\%$ is 26.0%. This maximum error would be 0 at n=1, 14.9% at n=0.8, and 41.4% at n=0.5.

It appears that at n=0.67 or above, the use of Equation (2-14) would yield an error at 26% or less.

2.4.3 Effect of Repassivation Kinetics

Film repassivation kinetics is one important parameter that affects CGR for high pH SCC. A larger repassivation kinetic exponent *n* represents a stronger tendency of repassivation. Figure 2-7 shows CGR vs. *K* at different values of *n*. As expected, a larger *n* results in a lower CGR due to a smaller duration for charge transfer during a film rupture event.

Many factors may affect film repassivation kinetics. The experimental data reported on passive alloys have revealed that the values of *n* can depend on temperature, water chemistry, and potential [3]. The compositions and microstructures of steels can have also an effect. Unfortunately, abundant experimental data for pipelines are not available, so the model in this work cannot fully incorporate these effects.

2.5 Conditions for the Model to Use in the Field

The CGR model is developed for deep and active cracks. When the deep cracks are known to be dormant, the CGR needs to be adjusted to zero. In the field, many microcracks can initiate on the pipe surface, while only a few can grow into cracks that can lead to a failure [6-7]. To reliablly predict pipeline life controlled by SCC, the practical application of the model needs to be discussed.

For high pH SCC, cracks may be considered to become dormant when

$$K \leq K_{ISCC} \tag{2-15}$$

It is recognized that small cracks can initiate and propagate at *K* levels well below K_{ISCC}. However, when a crack can be detected by existing ILI tools, its size generally already exceeds 1 mm (resolution of the tool) and it is already a deep crack and the model is applicable.

The magnitude of K_{ISCC} for a given crack can depend on the surrounding environmental conditions. Using precracked specimens, Parkins et al. [6,21] measured a K_{ISCC} in 1N-1N carbonate-bicarbonate solution at 75 °C to be 21 $MPam^{1/2}$ (Figure 2-3). This threshold SIF is equivalent to a crack penetration of 1 mm into the pipe wall for an X60 pipe with a 40 in. outer diamter 0.32 in. wall thickness and operating at 70% of specified minimum yield strength (SMYS). Table 2.2 provides crack depths required to reach K_{ISCC} at 20 $MPam^{1/2}$ for several steel

pipes under different operating conditions. In general, under the threshold K_{ISCC} at 21 $MPam^{1/2}$, the crack depth exceeds 1 mm.

Under cyclic loading conditions, it is likely that the threshold is smaller than K_{ISCC}. Thus, when ILI tools detect a crack, the crack would be considered to be growing without dormancy.

2.6 Summary

Predictive models under both constant and cyclic loading conditions are proposed for predicting high pH SCC CGRs of pipelines. These models were developed assuming the effect of mass transfer in a crack can be neglected for a concentrated carbonate and bicarbonate solution buffer.

Consistency between model predictions and experimental data is shown, suggesting that the model developed can be applicable for predicting the trends of pipeline CGRs.

Cracks that can be detected by ILI tools are deep enough with their SIFs most likely greater than K_{ISCC}. The CGR can thus be estimated from the current model.

2.7 References

1. M. Sutcliffe, R. R. Fessler, W. K. Boyd, R. N. Parkins, Stress Corrosion Cracking of Carbon Steel in Carbonate Solutions, Corrosion, 28, 1972, 313-320.
2. R. N. Parkins, Strain Rate Effects in Stress Corrosion Cracking**,** Corrosion**,** 46, 1990, 178-189.
3. F. P. Ford, Quantitative Prediction of Environmentally Assisted Cracking, Corrosion, 52, 1996, 375-395.
4. F. M. Song, Predicting the Mechanisms and Crack Growth Rates of Pipelines Undergoing Stress Corrosion Cracking at High pH, Corrosion Science, 51, 2009, 2657-2674.
5. R. W. Staehle, Transient Stability of Passive Films in Aqueous Solutions, Corrosion Science, 49, 2007, 7-19.
6. R. N. Parkins, Factors Influencing Stress Corrosion Cracking Kinetics, Corrosion, 43, 1987, 130-139.
7. J. Been, F. King, L. Fenyvesi, R. Sutherby, A Modeling Approach to High pH Environmentally Assisted Cracking, International Pipeline Conference, 2004, paper # IPC04—361.
8. T. Shoji, Quantitative Prediction of Environmentally-Assisted Cracking Based on Crack Tip Strain Rate, in Proc. ASME-PVP Symposium, Predictive Capacities in Environmentally-Assisted Cracking, Miami, November 1985, 127-142.
9. H. Tata, P. Paris, G Irwin, The Stress Analysis of Cracks Handbook, second edition, 1985, 2.10-2.12.
10. X. Wang, S. B. Lambert, Stress Intensity Factors for Low Aspect Ratio Semi-Elliptical Surface Cracks in Finite-Thickness Plates Subjected to Non-Uniform Stresses, Engineering Fracture Mechanism, 51, 1995, 517-532.

11. T. Shoji, Z. P. Lu, H. Murakami, Formulating Stress Corrosion Cracking Growth Rates by Combination of Crack Tip Mechanics and Crack Tip Oxidation Kinetics, Corrosion Science, 52, 2010, 769-779.
12. Y. C. Gao, K. C Hwang, Elastic-Plastic Crack Tip Fields in Steady Crack Growth in a Strain Hardening Material, in D. Francois (Ed.), Advances in Fracture Mechanics, Vol. 2, 5th International Conference on Fracture, 1981, 669-682.
13. M. M. Hall, Jr., An Alternative to the Shoji Crack Tip Strain Rate Equation, Corrosion Science, 50, 2008, 2902-2905.
14. Y. C. Gao, X. T. Zhang, K. C. Hwang, The Asymptotic Near-Tip Solution for Mode-III Crack in Steady Growth in Power Hardening Media, Int. J. Fract., 21, 1983, 301-317.
15. J. W. Hutchinson, J. Mech. Phys. Solids, 16, 1968, 13-31.
16. D. P. G. Lidbury, Estimation of Crack Tip Strain Rate Parameters Characterising Environmental Assisted Crack Growth Data, Embrittlement by the Localized Crack Environment, Proc. Conf. AIME, ed. R. P. Gangloff, 1984, 140-172.
17. S. J. Hudak, Jr., D. L. Davidson, R. A. Page, On Role of Crack Tip Deformation in Corrosion, Embrittlement by the Localized Crack Environment, Proc. Conf. AIME, ed. R. P. Gangloff, 1984, 172-196.
18. R. O. Ritchie, Mechanisms of Fatigue-Crack Propagation in Ductile and Brittle Solids, International Journal of Fracture, 100, 1982, 55-83.
19. A. J. McEvily, R. O. Ritchie, Crack Closure and the Fatigue-Crack Propagation Threshold as a Function of Load Ratio, Fatigue and Fracture of Engineering Materials and Structures, 21, 1998, 847-855.
20. K. S. Jian, J. L. Tzou, R. O. Ritchie, Role of Crack Tip Shielding in the Initiation and Growth of Long and Small Fatigue Cracks in Composite Microstructure, Metallurgical Transactions A, Physical Metallurgy and Materials Science, 18 A, 1987, 1613-1627.
21. R. N. Parkins, B. S. Greenwell, The Interface between Corrosion Fatigue and Stress Corrosion Cracking, Metal Science, 1977, 405-413.
22. A. K. Pilkey, S. B. Lambert, A. Plumtree, Stress Corrosion Cracking of X-60 Line Pipe Steel in a Carbonate-Bicarbonate Solution, Corrosion, 51, 1994, 91-96.
23. J. Beavers, C. L. Durr, B. S. Delanty, High-pH SCC: Temperature and Potential Dependence for Cracking in Field Environments, Intern Pipeline Conf. IPC 1998, Calgary, AB, Canada, 1998, 423-437.

Table 2-1. Parameters Used in Calculation

d_n	Coefficient for CTOD calculation	0.3
E (GPa)	Young's modulus	200
F (C/mol)	Faraday's constant	96485
I_n	a constant	4.9
K_{ISCC} (MPam$^{1/2}$)	Threshold SIF for SCC	20
M (kg/mol)	Atomic mass of iron	55.845×10^{-3}
N	Repassivation kinetic exponent	0.667
N	Strain hardening exponent defined by Ramberg-Osgood law	6
N^*	Strain hardening exponent defined by $\frac{\varepsilon}{\varepsilon_y}=\frac{\sigma}{\sigma_y}+\alpha^*\left(\frac{\sigma-\sigma_y}{\sigma_y}\right)^{N^*}$	1.6
r_0 (m)	Specific length for CTSR calculation	1×10^{-6}
t_0 (s)	Incubation of repassivation	0.01
w (m)	Pipe wall thickness	0.01
Z	Number of electrons exchanged in corrosion	2
Greeks		
α	Coefficient in the Ramberg-Osgood equation	1.04
β	Rice's coefficient	5.08
ε_0 (MPa^{-2}m^{-1})	Cyclic CTSR coefficient	1.56×10^{-4}
ε_f	Rupture ductility of passive film	0.001
λ	A dimensionless constant	$1/3\pi$
ν	Poisson ratio	0.3
ρ (kg/m^3)	Density of iron	7.847×10^{6}
σ (MPa)	Stress	$0.5\sigma_y$
σ_y (MPa)	Yield strength	384

Table 2-2. Crack Depth (mm) Required to Meet K_{max}=20MPam$^{1/2}$

σ_{hoop} /SMYS	Pipeline steel	X52	X60	X65	X70
72%	40"OD/0.32"w	1.2	0.95	0.85	0.75
72%	20"OD/0.24"w	1.1	0.9	0.75	0.71
50%	10"OD/0.12"w	1.1	1	0.92	0.86

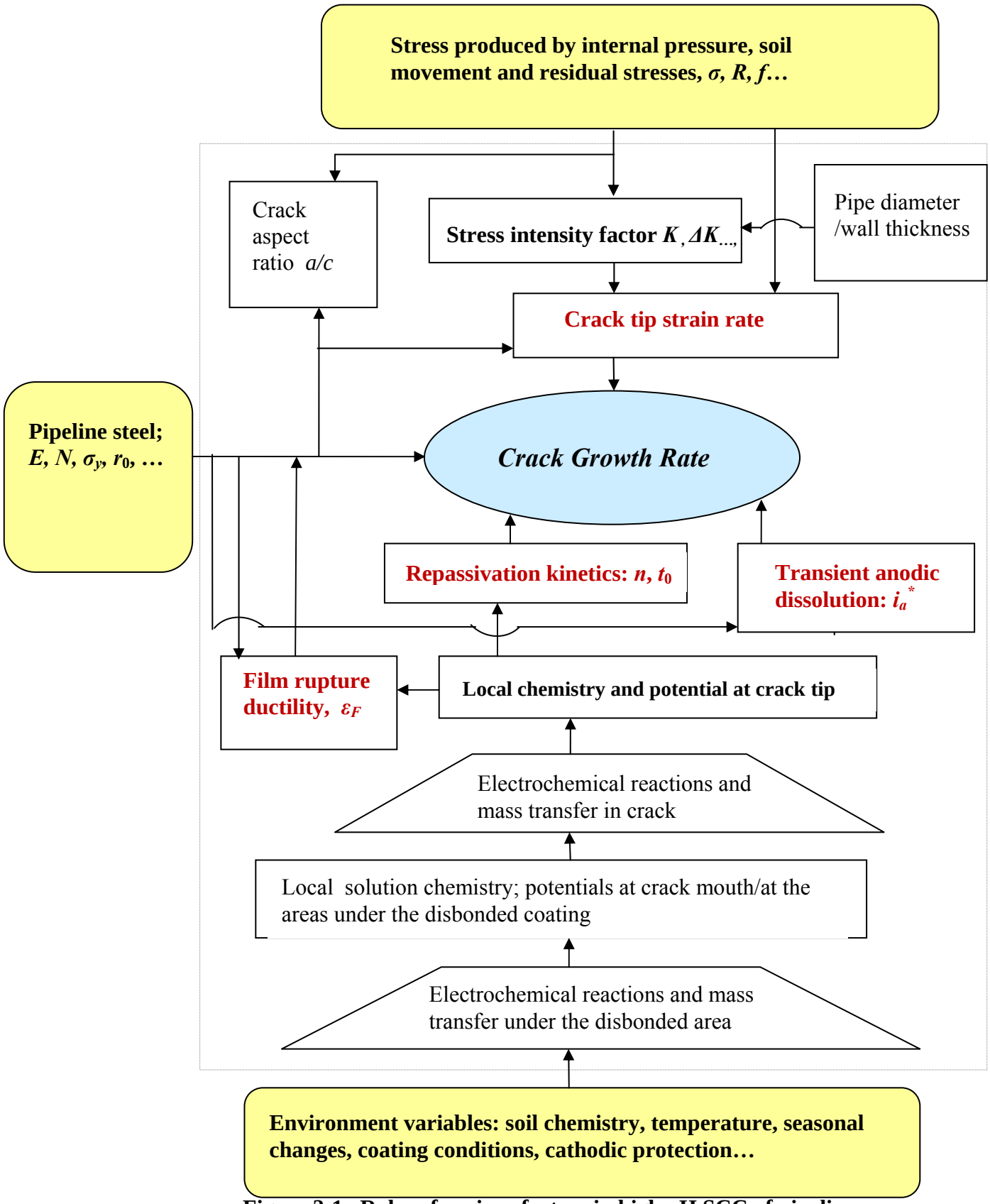

Figure 2-1. Roles of various factors in high pH SCC of pipelines.

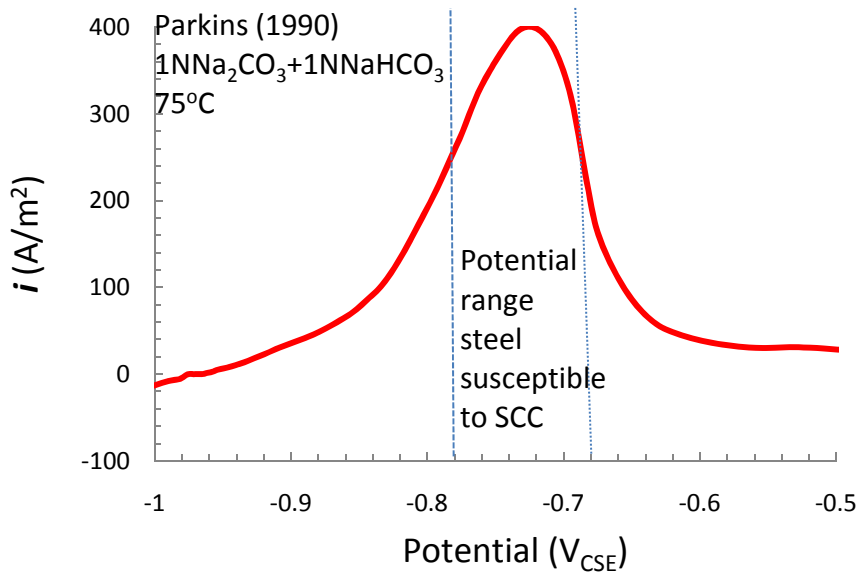

Figure 2-2. Polarization curve of pipeline steel determined with potential scanning rate 1 V/min.

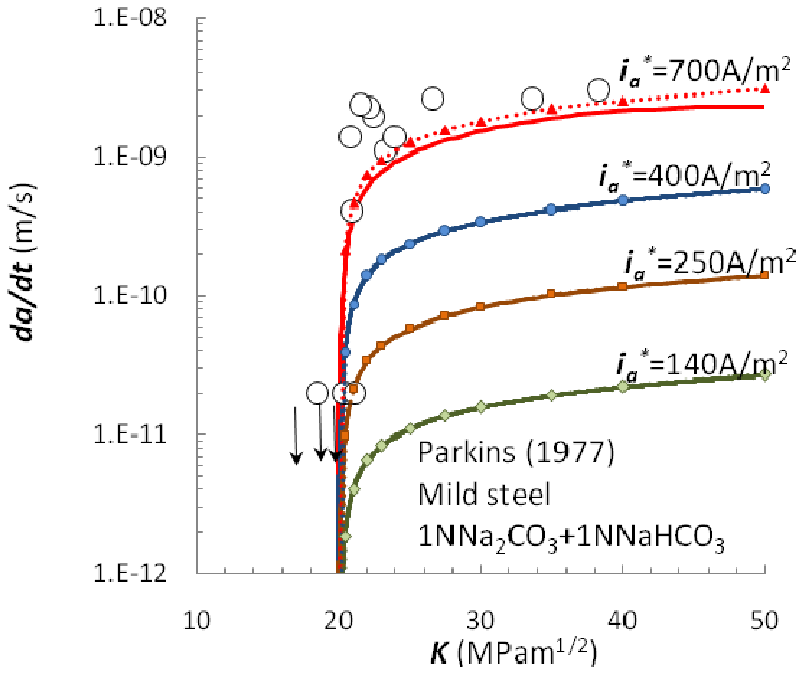

Figure 2-3. Effects of anodic current density over the bare metal surface on CGRs, Solid lines: predicted by Equation 2-6 without mass transfer. Small solid points: with mass transfer effect. Large open circle points: the experimental data Parkins [21] reported.

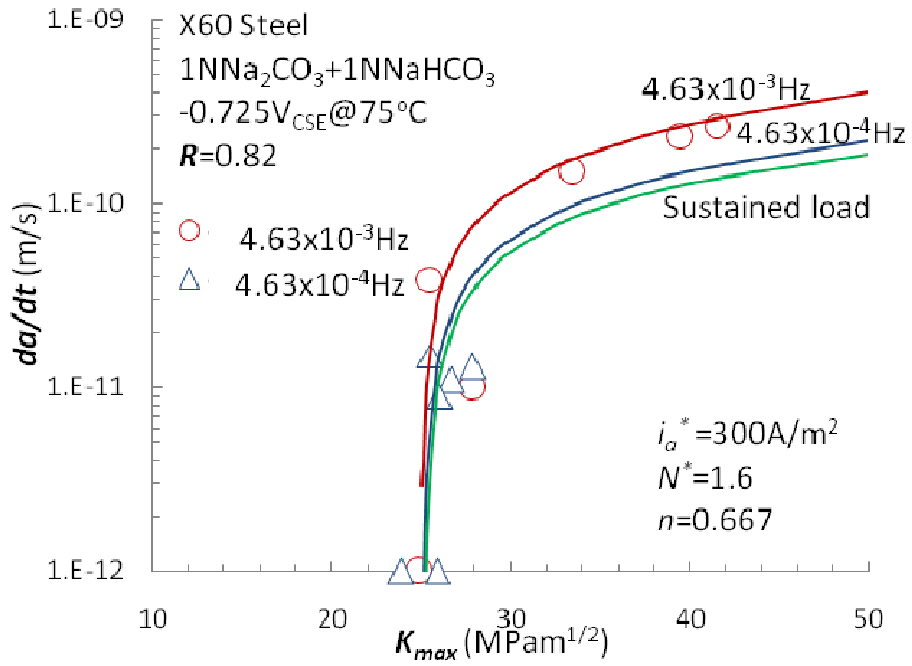

Figure 2-4. Comparison between the crack velocities determined by experiments and predicted by Equation (2-11). Open circle and triangle points: the experimental data Pilkey et al. [22] reported.

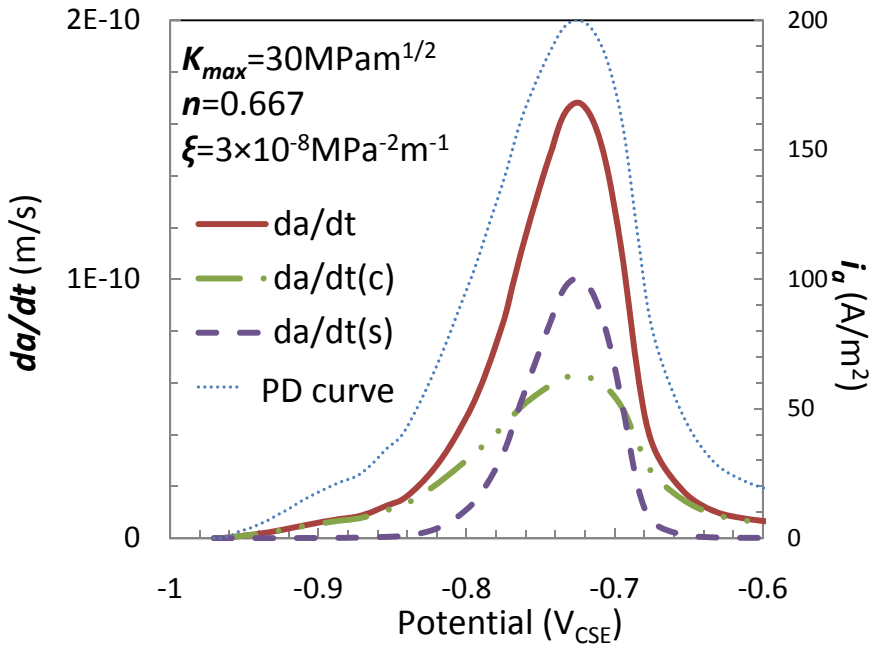

Figure 2-5. Effect of potential on CGR.

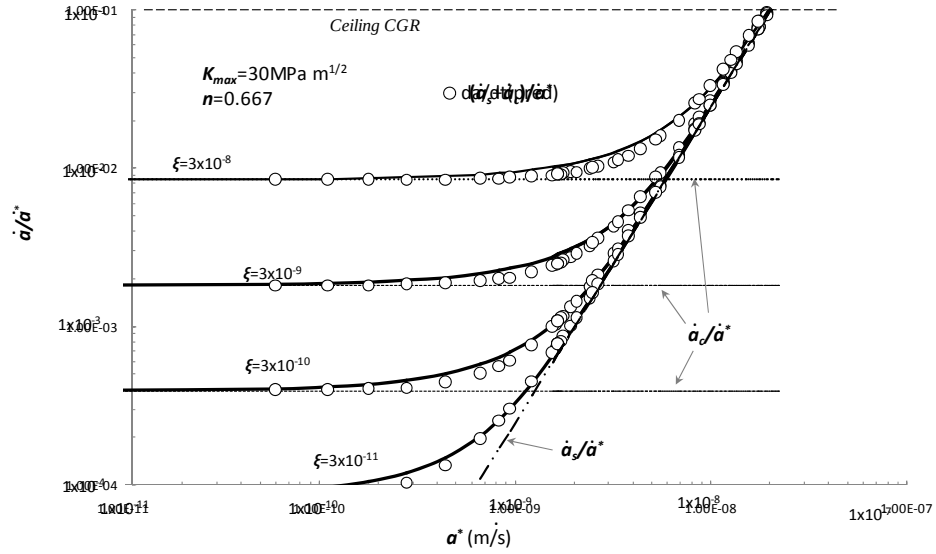

(a)

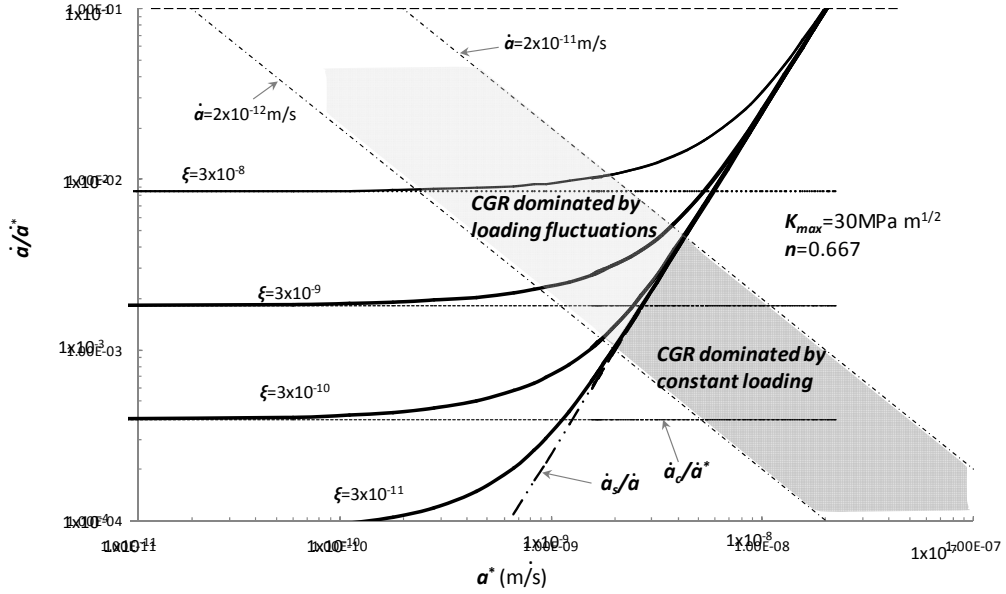

(b)

Figure 2-6. The relative significance of constant load and loading fluctuation on CGR (a) without and (b) with the practical range of CGRs shown.

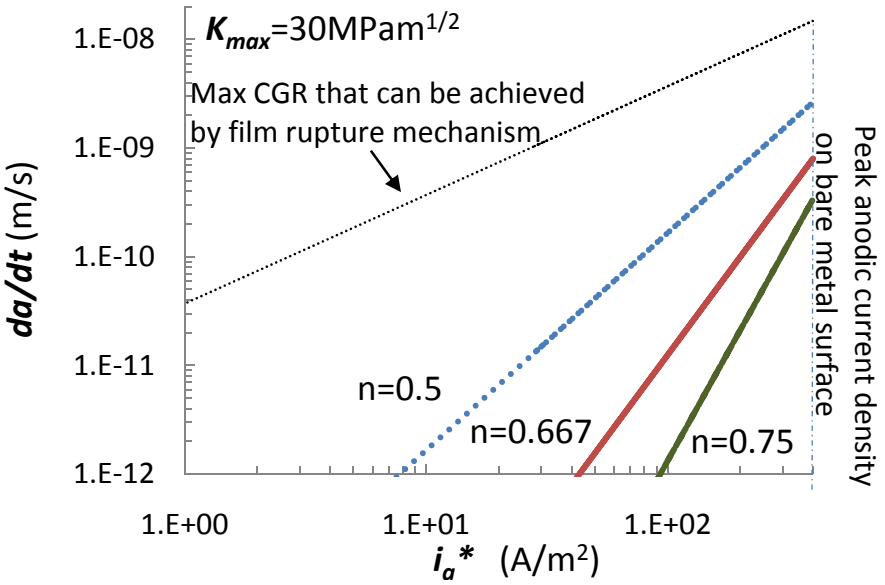

Figure 2-7. Effect of repassivation kinetcs exponent on CGR.

3.0 NEAR NEUTRAL pH CGR MODEL

3.1 Technical Background and Objectives

Laboratory investigations and field observations have indicated that near-neutral pH SCC normally occurs when pipeline steels are exposed to dilute groundwater with a pH in the range of 6-8 [1]. Reviews of near-neutral pH SCC mechanisms [1-2] reveal that crack growth of pipe steels in near-neutral pH environments can be dominated by the hydrogen-assisted cracking (HAC) mechanism [2-4]. Anodic dissolution may also play a role [5-7], although the exact role is not yet clear [8-9]. Experiments have shown that anodic dissolution under constant load can lead to dormancy of cracks [4,8], while others suggested that may assist cracking [10]. For the purpose of this work, the role of anodic dissolution in the near-neutral pH SCC is not considered. HAC is treated to control the crack growth.

Laboratory tests show that near-neutral pH SCC cannot, in general, be reproduced unless the load is cyclic [1-2,8], although a few researchers claimed that they observed crack initiation [11] and propagation [12] under constant loading conditions. Chen and Sutherby [13] observed that cracks that become dormant under constant load can restart propagating when cyclic loads were applied. In service pipelines, cyclic stresses cannot be avoided, owing to internal pressure fluctuations. Thus, cyclic stresses are likely the cause of near-neutral pH crack growth on service pipelines.

Chen and Sutherby [13] regarded cracking of pipeline steels in near-neutral pH environments as true corrosion fatigue. Built on a significant amount of laboratory data, they found that the measured CGR, *da/dN*, could be expressed by a characteristic group of parameters, $K_{max}\Delta K^2 f^{-0.1}$, where K_{max}, ΔK, and f are maximum SIF, during a stress cycle, the difference between maximum and minimum SIF and the stress frequency, respectively. Because the use of this group of parameters can allow for convergence of the scatters of CGR data caused by different K_{max} and different frequencies f, Chen and Sutherby rationalized that the first two terms, $K_{max}\Delta K^2$, may approximately represent crack growth through mechanical fatigue loading, while $f^{-0.1}$ reflects enhanced crack growth by corrosion. Here, the exponent over f, or -0.1, is considered the environmental effect on CGR.

Although a near straight line is shown in a log-log plot between CGR *da/dN* and $K_{max}\Delta K^2 f^{-0.1}$ for two environmental conditions (Figure 3-1) and this plot can allow for the relation between *da/dN* and $K_{max}\Delta K^2 f^{-0.1}$ to be derived from the data fitting, the authors [13] never explicitly provided such a relation. Besides, all the data used in the plots were generated from only two solutions, C2 and NOVATW, of similar chemistry. The possible significant effect of different environments and different levels of imposed cathodic polarizations is not reflected in the previously noted empirical relation.

The objective of this work is to provide an improved CGR model that correlates CGR with environmental factors. Atomistic hydrogen concentration in steel is used in correlating the environmental factors (chemistry and cathodic potential) with CGR.

3.2 Near-Neutral pH SCC CGR Model

A CGR model is developed to include the effect of environmental factors on CGR, including the solution pH and the pipe potential at the crack mouth. This environmental effect is reflected by the atomic hydrogen concentration in steel.

3.2.1 Atomic Hydrogen Concentration Distribution in Steel

Interstitial hydrogen in steel is known to affect CGR for near-neutral pH SCC of buried pipelines. Thus, an understanding of the distribution of interstitial hydrogen in steel is a significant step to include the hydrogen effect in a CGR model.

Based on the derivation given in Appendix 3.A [14-15], the relation with SIF of the maximum hydrogen concentration in steel lattice (free of defects) can be expressed by

$$\frac{C_{H.max}^{Lat.}}{C_0} = \exp\left(\frac{\eta K_{max}}{RT\sqrt{r_{FPZ}}}\right) \tag{3-1}$$

where r_{FPZ} is the size of fracture process zone (FPZ) ahead of the crack tip, η is a material constant, R is universal gas constant, T is absolute temperature, C_0 is atomic hydrogen concentration in bulk steel and $C_{H.max}^{Lat.}$ is critical atomic hydrogen concentration in steel lattice.

To use Equation (3-1) in the CGR model to be developed, it is assumed that the pipe surface is exposed to a corrosive environment long enough before crack initiation. The atomic hydrogen concentration in the bulk steel C_0 is time independent, although it can be affected by the environments, the microstructure, and surface condition of pipeline steels. The crack initiation or growth is related only with the local concentration of atomic hydrogen around the crack tip.

The atomic hydrogen consumed in the embrittlement process can be generated at the internal surface within the crack and from hydrogen diffusion in the bulk steel [16]. The former is produced during the corrosion reactions at the crack walls and at the newly created surface at the crack tip [17-18]. The latter is mainly produced by the reductions of hydrogen ions or water over the pipeline (or specimen) surface out of the crack.

Chen Sutherby [13] measured the CGRs of X-65 steel in simulated soil chemistries with near-neutral pH using compact tensile specimens. They divided specimens into three groups: uncoated, partially coated, and fully coated with a thin layer of insulator. They measured the CGRs to understand the effect of corrosion reactions at the surfaces outside the crack on CGR. The results are shown in Figure 3-2. The CGR of uncoated specimens is shown to be much greater than that of the coated ones, suggesting that the hydrogen atoms generated on the specimen surfaces outside of the crack are likely the dominant source of atomic hydrogen in the steel. Due to the significant effect of atomic hydrogen on CGR, the development of the CGR model will be based on a hydrogen embrittlement mechanism.

3.2.2 CGR Model

The data presented in Figures 3-1 and 3-3 from different sources [13,19] were plotted against stress ratios and loading frequencies. It is shown that *da/dN* and $K_{max}\Delta K^2 f^{-0.1}$ are related by

$$\frac{da}{dN} = B(K_{max}\Delta K^2 f^{-0.1})^2 \quad (3\text{-}2)$$

The coefficient *B* can be obtained by data fitting, and its value is given in Table 3-2, which is shown to vary with solution pH.

When the crack growth is governed by a hydrogen embrittlement mechanism, the atomic hydrogen enriched in the plastic zone ahead of the crack tip can be an important factor in determining the CGR. As suggested by Figure 3-2, when the hydrogen atoms are produced mainly on the surface outside of crack, C_0 in Equation (3-1) represents the atomic hydrogen concentration in the lattice of bulk steel.

The postulation of Thomas and Wei [20] for the relation between the increment of crack size in a loading cycle with the FPZ size (r_{FPZ}) may be generalized from linear to a power law relation as follows:

$$\frac{da}{dN} \propto r_{FPZ}^{\lambda} \quad (3\text{-}3)$$

where λ is an empirical exponent to be determined and "∝" represents "proportional."

By substitution of Equation (3-1) into Equation (3-3),

$$\frac{da}{dN} \propto \left[ln\left(\frac{C_{cr}^{Lat.}}{C_0}\right)\right]^{-2\lambda} \left(\frac{\eta}{RT}K_{max}\right)^{2\lambda} \quad (3\text{-}3a)$$

By a comparison of Equation (3-2) with Equation (3-3a) for K_{max}, $\lambda = 1$ to ensure the same exponent of K_{max}. When the effect of atomic hydrogen on the cracking kinetics is considered and K_{max} in Equation (3-3a) is generalized to the group of parameters in Equation (3-2), Equation (3-3a) may become

$$\frac{da}{dN} = B_0\left[ln\left(\frac{C_{cr}^{Lat.}}{C_0}\right)\right]^{-2} (K_{max}\Delta K^2 f^{-0.1})^2 \quad (3\text{-}4)$$

where f is loading frequency and ΔK is change of SIF, a driving force for crack growth.

$$B_0 = B\left[ln\left(\frac{C_{cr}^{Lat.}}{C_0}\right)\right]^2 \quad (3\text{-}5)$$

3.3 *Critical Lattice Hydrogen Concentration* $C_{cr}^{Lat.}$ *and* B_0 **in Equation (3-5)**

Although the atomic hydrogen concentration in the steel bulk does not vary with crack growth, it varies with and can be determined by the environmental chemistry and the electrochemical potential. Figure 3-4(a) shows the measured C_0 vs. steel potential at different solution pHs around neutral [2]. Simulated groundwater was used in the test and the solution pH was adjusted by the CO_2 partial pressure in a mixed gas purging into the solution[2].

The following formula fits well with the experimental data for the solution with pH 6.3 as shown in Figure 3-4(a):

$$C_0 = X_{6.3}\frac{(5+10\psi_1)*10^{-10}\exp\left(-\frac{\psi_1}{0.03}\right)}{5+10\psi_1-10^{-10}\exp\left(-\frac{\psi_1}{0.03}\right)} \ \text{(mol/cm}^3\text{)} \tag{3-6}$$

where ψ_1 is the potential measured versus $Cu/CuSO_4$ for the solution with pH of 6.3 and it ranges from -0.9 to -0.5 V_{CSE}. $X_{6.3} = 10^{-6}$ is a fitting constant in mol/cm^3.

When Equation (3-6) is used for the other solutions in Figure 3-4(a) with pH ranging from 5.1~8.3, X_{pH} needs to be generalized by

$$X_{pH} = [5 - 0.019(10^{6.3-\text{pH}} - 15.5)^2]\cdot 10^{-6} \ \text{(mol/cm}^3\text{)} \tag{3-6a}$$

and ψ_1 needs to be replaced by ψ. They are correlated with each other by

$$\psi = \psi_1 + 0.052(pH - 6.3)^2 \mp 0.035(pH - 6.3) \tag{3-6b}$$

Assuming Equations (3-6a) and (3-6b) can be generalized for all solutions with pH in the range of 5.1~8.3, Equation (3-6) may be generalized as

$$C_0 = X_{pH}\frac{-(5+10\psi)*10^{-10}\exp\left(-\frac{\psi}{0.03}\right)}{-5-10\psi+10^{-10}\exp\left(-\frac{\psi}{0.03}\right)} \ \text{(mol/cm}^3\text{)} \tag{3-6c}$$

The use of Equation (3-6c) can lead to the convergence of the data obtained at different pHs in Figure 3-4(a) to one curve as shown in Figure 3-4(b).

When Equation (3-6c) is used for the three solutions in Figures 3-1 and 3-3 with different pHs, 7.11 (NOVATW) [13], 6.4 (Beaver 8-2) [19], and 6.26 (C2) [13], the interstitial hydrogen concentration in steel exposed in these solutions can be determined if the potential is known. The experimental data were obtained at open circuit conditions. Even though not all open circuit potential (OCP) data are reported, due to the small difference in pH among the three solutions, it may be assumed that their OCPs are the same and equal -0.665 V_{CSE}. With this information, the atomic hydrogen concentrations in the steel bulk for the three solutions are determined from Equation (3-6c) to be 0.026, 0.268, and 0.348 mol/m^3, respectively. They are given in Table 3-1.

With B obtained directly from Figures 3-1 and 3-3 and with C_0 obtained above, Equation (3-5) allows the determination of the values of B_0 and $C_{cr}^{Lat.}$. Figure 3-5 shows the result that $C_{cr}^{Lat.} \approx 3.3 \times 10^4$mol/m^3 and the values of B_0 are given in Table 3-1.

Figure 3-6 illustrates the CGRs in four different solutions with pHs ranging from 5.89~7.11, measured under fixed equivalent SIF and loading frequency [13]. The predicted CGRs are shown to be greater or more conservative than the experimental data.

3.4 Near-Neutral pH SCC Crack Dormancy

For near-neutral pH SCC, built on laboratory data shown in Figure 3-1, Chen et al. [4] developed the following criteria for crack dormancy:

$$K_{max}\Delta K^2 f^{-0.1} \leq 8500 \text{ MPa}^3\text{m}^{1.5}\text{Hz}^{0.1} \quad (3\text{-}7)$$

When the full-sized pipe CGR data Zhang et al. [21] generated are plotted together with the data in Figure 3-1 and data of others [19], Figure 3-7 is obtained. The data of Zhang et al. were obtained from full-sized 24 in. outer diameter X-65 steel pipe in NS4 solution deaerated by mixed gas consisting of 5% CO_2 and 95% N_2 in volume. The pH of the NS4 solution is 6.3~6.4. The stress in the pipe wall was controlled by hydraulic pressure inside the pipe.

It is clear from Figure 3-7 that this criterion does not capture the full-scale test data of Zhang et al. for near-neutral pH SCC, which were shown experimentally growing. Chen et al. [22] acknowledged the shortcoming of Equation (3-7) by stating that "the full-scale data do not predict a threshold condition of dormancy at around the threshold determined from lab investigation, or may exhibit a threshold condition of dormancy at significantly lower mechanical loading conditions."

Figure 3-7 suggests that there is a gap between the lab test results obtained by using small-scale compact specimens and the full-scale test results. If dormancy is present for the full-sized pipe, which better simulates field conditions, the threshold for dormancy would be significantly smaller. Shown in Figure 3-7, even at $K_{max}\Delta K^2 f^{-0.1} = 1300$ MPa^{3}m$^{1.5}$Hz$^{0.1}$, no sign of dormancy can be observed. The CGR here is already more than 30 times smaller than at the threshold determined from Equation (3-7). If the threshold of $K_{max}\Delta K^2 f^{-0.1}$ further decreases, the CGR would become even smaller and may become negligible relative to the CGR in the region above the dormancy threshold.

With small CGRs at the dormancy threshold for full-sized pipes, the consideration of crack dormancy for pipe life prediction becomes insignificant because the pipe life reduced by considering the dormancy is insignificant. Moreover, if the crack dormancy is neglected, the predicted life would be conservative due to a predicted smaller pipe life than if the crack dormancy is considered.

For this reason, crack dormancy will not be considered in this model.

3.5 Summary

A slightly modified CGR model from prior work of others was presented for near-neutral pH SCC of buried pipelines. The basis of the model is that the crack growth is controlled by hydrogen embrittlement mechanism and the CGR has a power law function with the FPZ size.

An improvement over the prior work is that the model can now account for the effect on CGR by external solution pH and pipe potential. This effect is embedded in a relation developed between them and the atomistic hydrogen concentration in steel.

Crack dormancy and its effect on CGR are discussed. Crack dormancy threshold has been shown by lab-scale tests, while it has not been manifested in tests of full-sized pipe specimens. Because the latter tests better resemble field conditions, crack dormancy will not be considered by the CGR model developed in this work.

3.6 References

1. R. N. Parkins, A Review of Stress Corrosion Cracking of High Pressure Gas Pipelines, Corrosion 2000, NACE International, 2000, paper 363.
2. J. A. Beavers, B. A. Harle, Mechanisms of High-pH and Near-Neutral-pH SCC of Underground Pipelines, Journal of Offshore Mechanics and Arctic Engineering, 123, 2001, 147-151
3. W. X. Chen, F. King, E. Vokes, Characteristics of Near-Neutral-pH Stress Corrosion Cracks in an X-65 Pipeline, Corrosion, 58, 2002, 267-275.
4. R. N. Parkins, W. K. Blanchard Jr., B. S. Delanty, Transgranular Stress Corrosion Cracking of High-Pressure Pipelines in Contact with Solution of Near-Neutral pH, Corrosion, 50, 1994, 394-408.
5. B. T. Lu, J. L. Luo, P. R. Norton, Effects of Dissolved Hydrogen, Anodic Dissolution and Plasticity on Active Dissolution of Pipeline Steel in Near-Neutral pH Groundwater, Acta Materialia, 57(1), 2009, 41-49.
6. F. King, T. Jack, W. X. Chen, M. Wilmott, R. R. Fessler, K. Krist, Mechanical Studies of Initiation and Early Stage Crack Growth for Near-Neutral pH SCC of Pipelines, Corrosion 2000, Paper 361, NACE International (TX), 2000.
7. W. X. Chen, R. Kania, R. Worthingham, G. Van Boven, Transgranular Crack Growth in the Pipeline Steels Exposed to Near-Neutral pH Soil Aqueous Solutions, The Role of Hydrogen, Acta Materialia, 57, 2009, 6200-6214.
8. B. T. Lu, J. L. Luo, P. R. Norton, Environmentally Assisted Cracking of Pipeline Steel in Near-Neutral pH Groundwater, Corrosion Science, 52, 2010, 1787-1795.
9. Z. Wang, J. Wang, E. Han, W. Ke, Influence of Intermittent Loading on SCC Behavior of or an X70 Pipeline Steel in a Near-Neutral pH Solution, Materials and Corrosion, 2007, 583-587.
10. B. Y. Fang, E. H. Han, J. Q. Wang, W. Ke, Stress Corrosion Cracking of X-70 Pipeline Steel in Near Neutral pH Solution Subjected to Constant Load and Cyclic Load Testing, Corrosion Engineering Science and Technology, 42, 2007, 123-129.
11. X. Y. Zhang, S. B. Lambert, R. Sutherby, A. Plumtree, Transgranular Stress Corrosion Cracking of X-60 Pipeline Steel in Simulated Ground Water. Corrosion, 55, 1999, 297-305.

12. W. X. Chen, G. Van Boven, R. Rogge, The Role of Residual Stress in Near-Neutral pH Stress Corrosion Cracking of Pipeline Steels, Acta Materialia, 55, 2007, 43-53.
13. W. X. Chen, R. L. Sutherby, Crack Growth Behavior of Pipeline Steel in Near-Neutral pH Soil Environments, Metall. Trans. A, 38A, 2007, 126-1268.
14. L. J. Qiao, J. L. Luo, X. Mao, Hydrogen Evolution and Enrichment Around Stress Corrosion Crack Tip of Pipeline Steels in Dilute Bicarbonate Solution, Corrosion, 54, 1998, 115-120.
15. W. W. Gerbrich, Y. T. Chen, Hydrogen-Controlled Cracking—An Approach to Threshold Stress Intensity, Metall. Trans. A, 6a, 1975, 271-278.
16. A. Turnbull, Local Hydrogen Generation and Its Impact on Environment-Assisted Cracking and Crevice Corrosion, to be published in Corrosion, 66(5), 2010.
17. M. Gao, M. Lu, R. P. Wei, Crack Path and Hydrogen-Assisted Crack Growth Response in AISI 4340 Steel, Metal. Trans. A, 15A, 1984, 735-746.
18. M. Gao, R. P. Wei, A "Hydrogen Partitioning" Model for Hydrogen-Assisted Crack Growth, Metall. Trans. A, 16A, 1985, 2039-2050.
19. J. Been, R. Eadie, R. Sutherby, Prediction of Environmental Assisted Cracking on Gas and Liquid Pipelines, Intern. Pipeline Conf. IPC 2006, Sept. 25-29, 2006, Calgary, AB, Canada, Paper No. 10345.
20. J. P. Thomas, R. P. Wei, Corrosion Fatigue Crack Growth of Steels in Aqueous Solutions II: Modeling of the Effect of ΔK, Mater. Sci., Eng., A159, 1992, 223-229.
21. W. Zhang, B. Tyson, G. Shen, R. W. Revie, G. Williams, D. Bibby, Effects of Operating Practices on Crack Dormancy and Growth, Report for Gas Research Institute, GPI-05/8668, CANMET, MTL-2005-10, 2005
22. W. X. Chen, R. Kania, R. Worthingham, S. Kariyawasam, Crack Growth Model of Pipeline Steels in Near-Neutral pH Soil**,** Proceedings of the Biennial International Pipeline Conference, IPC2008-64475, Calgary, AB, Canada, 2008, 1-10.

Table 3-1. The Parameters for Crack Growth Kinetics

Solution/pH	B ($MPa^{-6}m^{2}s^{1/5}$)	$(K_{max}\Delta K^{2}f^{-0.1})_{th}$ ($MPa^{3}m^{3/2}s^{1/10}$)	C_0 (mol/m^{3})	B_0 ($MPa^{-6}m^{-2}s^{-1/5}$)
NOVATW /pH7.11[13]	1.0×10^{-15}	8345.45	0.026	1.9×10^{-13}
Beavers 8-2/pH6.4[19]	1.4×10^{-15}	7221.84	0.268	1.9×10^{-13}
C2 /pH6.29[13]	1.5×10^{-15}	6957.66	0.346	1.9×10^{-13}

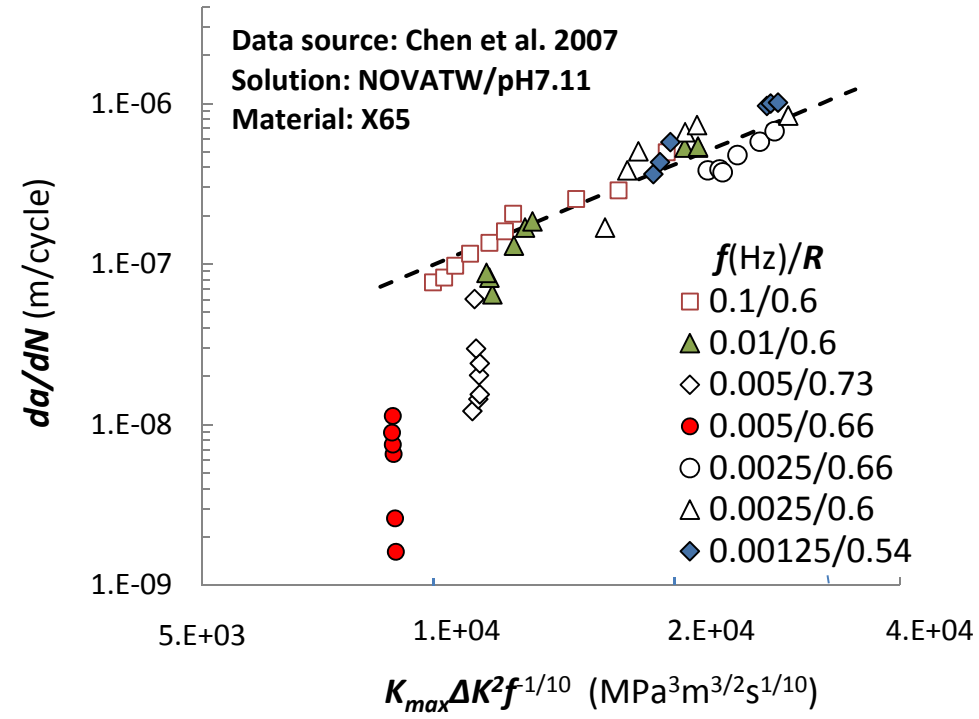

(a)

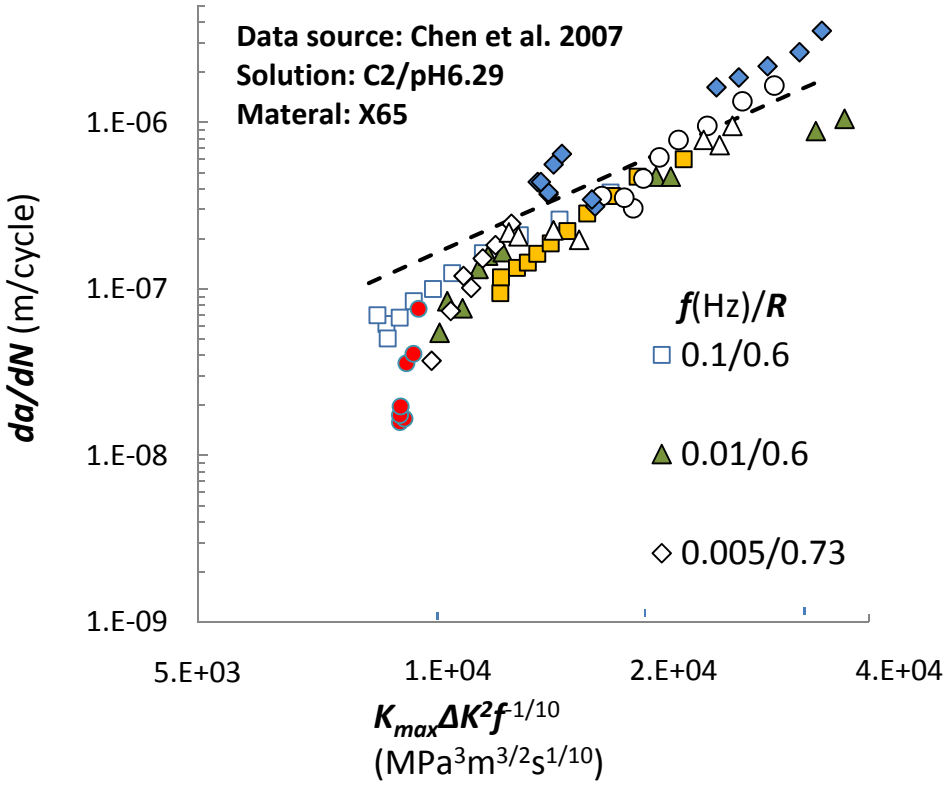

(b)

Figure 3-1. Experimental Data and Crack Growth Curves (the Test Data are Quoted from [13]).

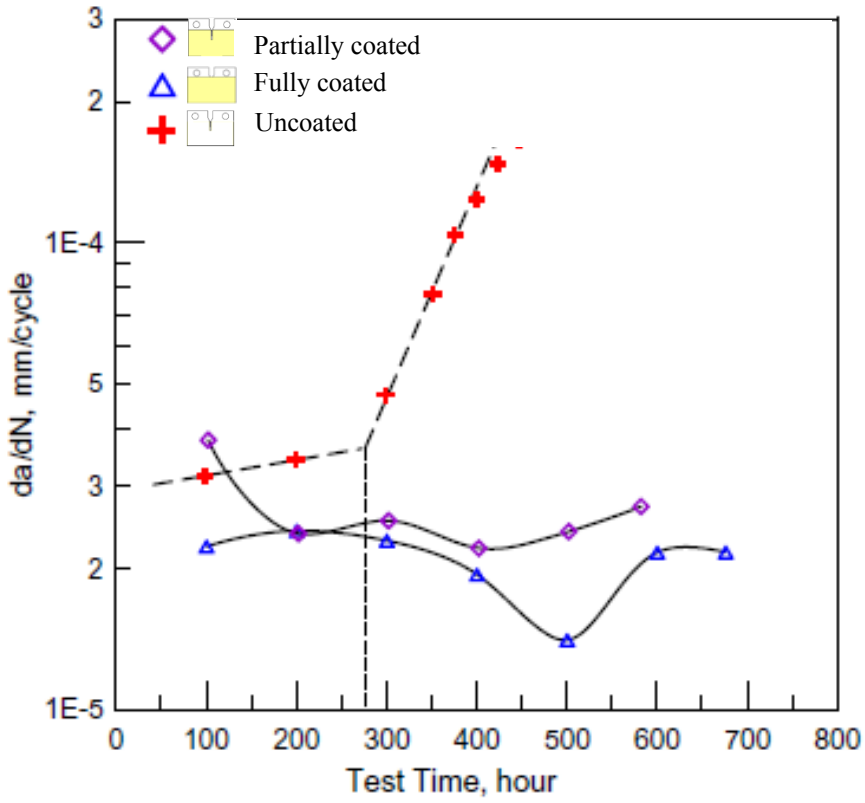

Figure 3-2. Effect of Surface Coating on Crack Growth of X-65 Steel in a Simulated Groundwater (C2). Test Condition: Open Circuit Potential, K_{Imax} = 35.3MPam$^{1/2}$, ΔK_I = 12MPam$^{1/2}$, and f = 0.005Hz [7].

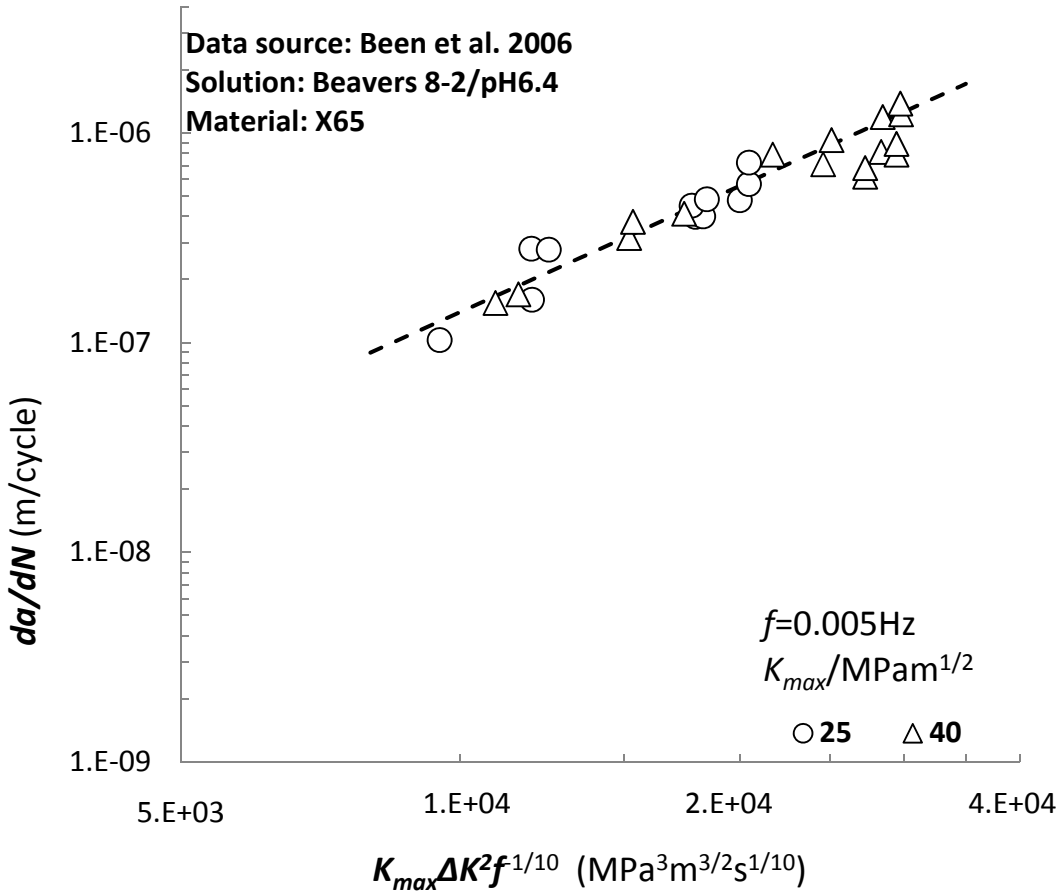

Figure 3-3. Experimental Data and Crack Growth Curves (the Test Data are Quoted from [19]).

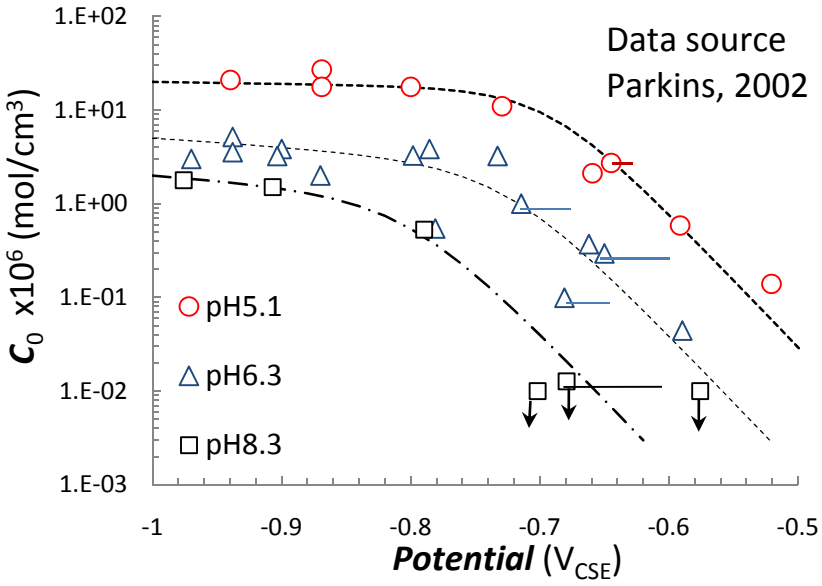

(a)

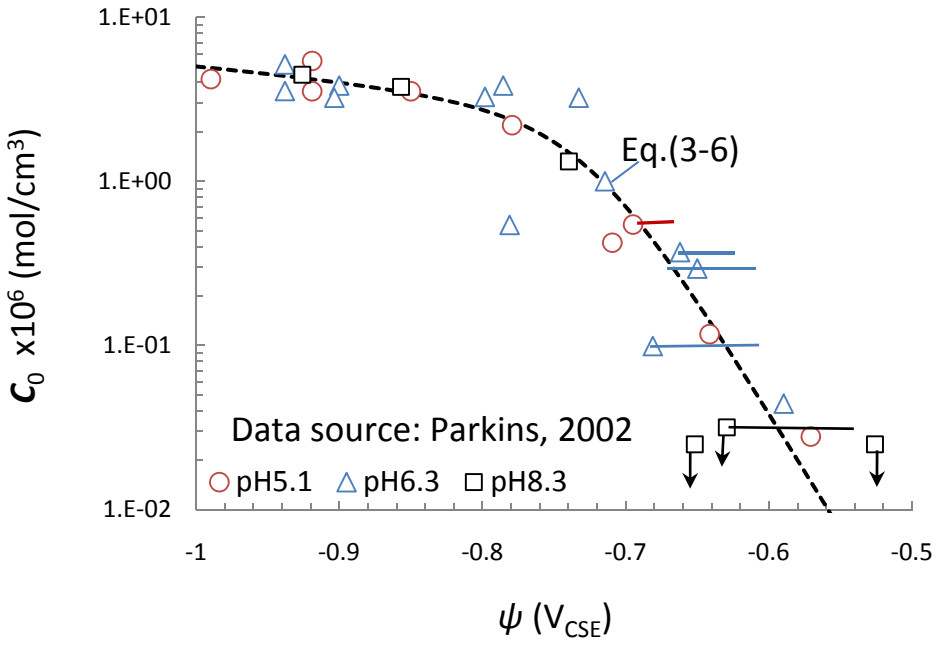

(b)

Figure 3-4. Effects of Potential and Solution pH on Dissolved Hydrogen Concentration in Pipeline Steel. The Original Data are Quoted from [2]. The Test Solution is NS4. The Bars Show the Tests Conducted at the Open Circuit Potential.

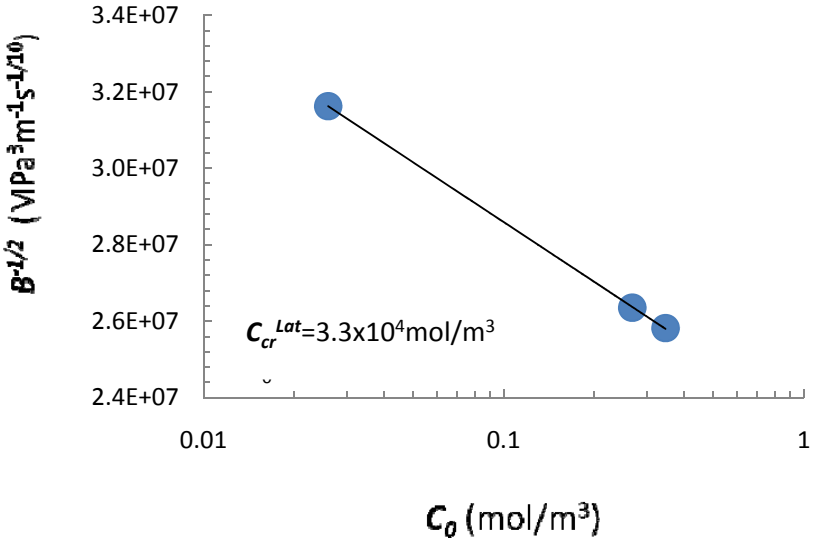

Figure 3-5. Dependence of the Crack Growth Coefficient on the Dissolved Hydrogen Concentration in Steel.

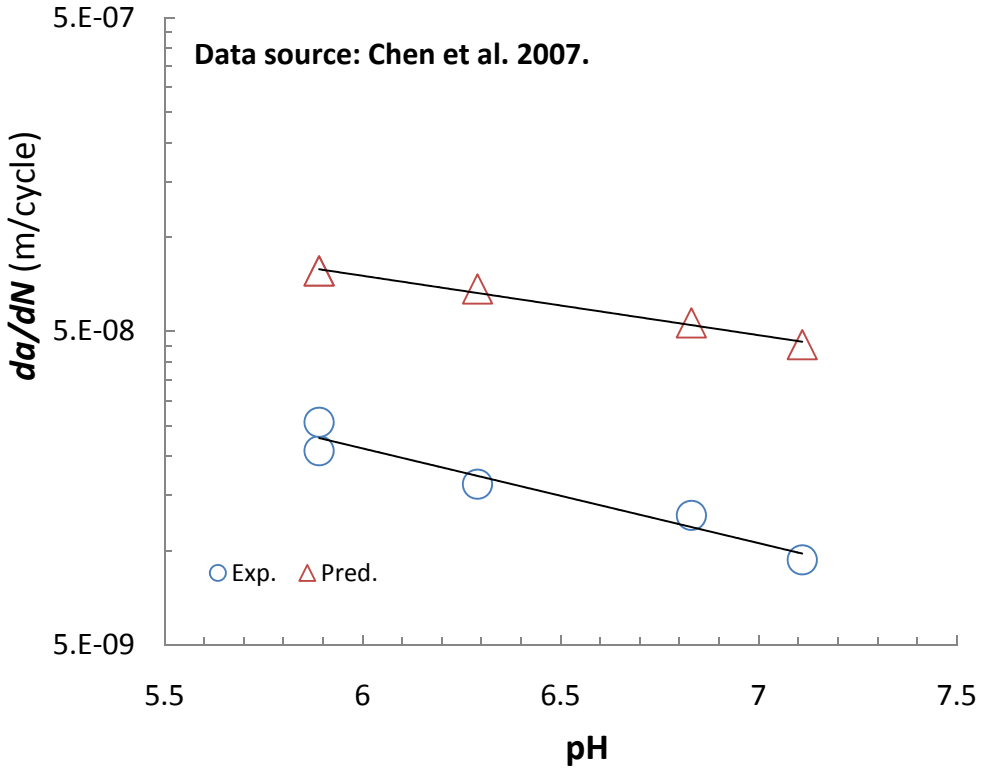

Figure 3-6. Effect of Solution pH on the CGRs. The Test Data are Quoted from [13]. ($K_{Imax} = 35.3$MPam$^{1/2}$, $\Delta K_I = 10.6$MPam$^{1/2}$, and $f = 5 \times 10^{-3}$Hz).

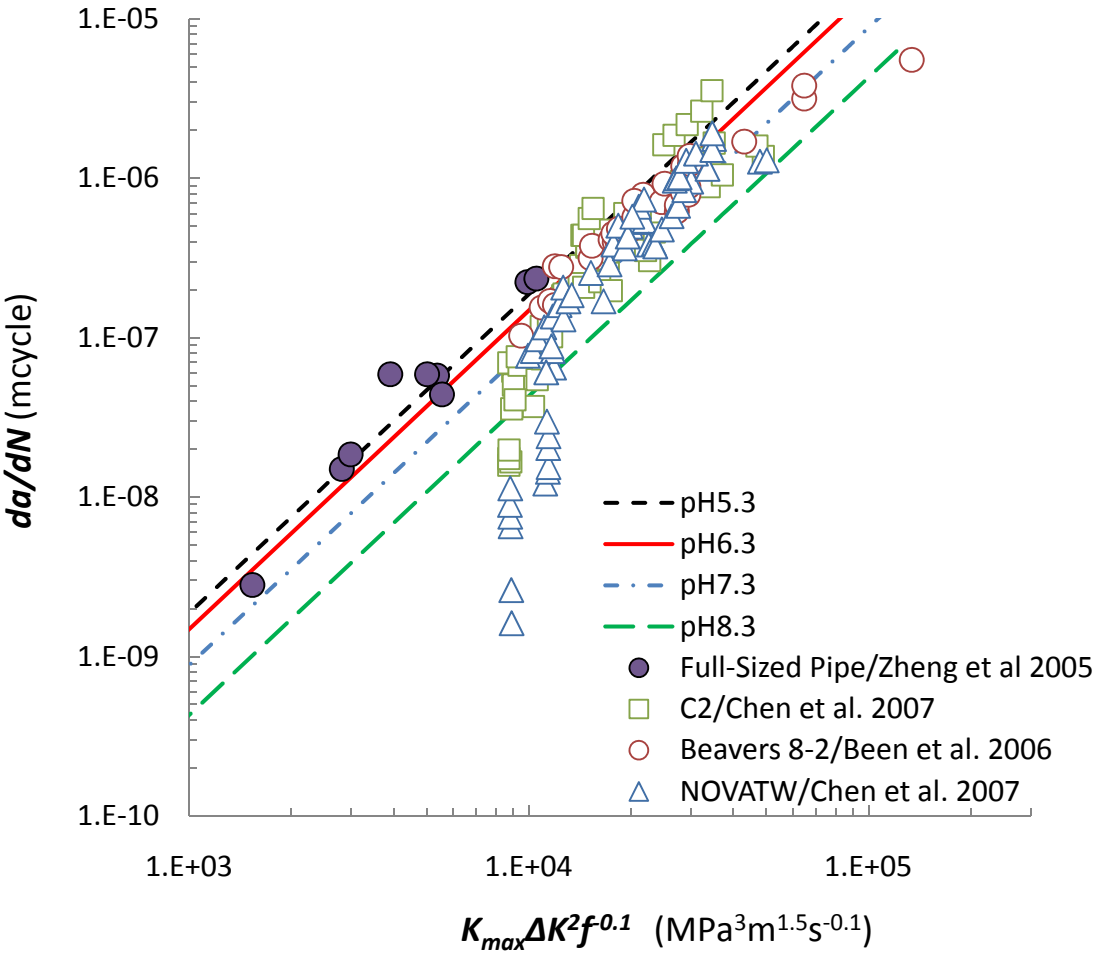

Figure 3-7. The Effect of Solution pH on CGR (the Test Data were Quoted from [13, 19, 21]).

4.0 SUGGESTED PROCEDURES FOR FIELD APPLICATION OF THE MODELS

One important element of this project is to develop tools that may allow for the models of this work to be implemented in field applications. This effort is presented in this section.

Although it would be most beneficial if an example fully built on field data could be provided, the data needed for such an example were unavailable in this project. Even though the procedures for implementing the tools are straightforward, a hypothetical example is provided to demonstrate how the tools can be used step by step.

We will start with the procedures for high pH SCC followed by those for near-neutral pH SCC. For either model, the overall procedure mainly consists of four steps.

The first step is data collection and a feasibility study to determine whether the model is applicable to the conditions for CGR prediction and the data collected are adequate for making the prediction. If it is determined that the model is feasible, the second step is determination of the model parameters from data collected and actual application of the model for CGR prediction given the field conditions. The third step is a reality check of model predictions versus known prior CGRs or field experience and provides suggestions for model improvement. The fourth step is an overall evaluation of all CGRs obtained from this and other methods (e.g., linear extrapolation or a conservative fixed rate) and a determination of the actual CGR to be used for specific applications.

4.1 Procedure for Field Use of the High pH SCC CGR Model –Constant Loading

4.1.1 Step 1: Data Collection and Feasibility Study

In this step, input data required for the model prediction must be collected. Such input data may include (a) pipe design data, such as steel type and composition, pipe diameter, wall thickness, coating type and thickness, and depth of cover; (b) pipe operating history, such as date of commission, duration of operation, operating temperature, pressure, and level of cathodic protection; (c) maintenance data, such as past incidents and root causes, ILI data, hydrotest data, and direct assessment data; (d) soil data, such as soil type, chemical composition, and pH. This step will allow for determining whether the SCC of interest is high pH or near-neutral pH. If the type of SCC is the latter, the method in Section 4.3 is recommended.

Depending on the type of fluids (gas or liquid) transported, a rough estimate of the type of loading, constant or cyclic, may be determined. When necessary, the variation of hoop stress over time is determined, and the stress ratio and frequency are calculated. The results can be used to more accurately determine the loading frequency and stress ratio.

For gas pipelines, normally $R>0.8$ and $f<10^{-5}$ Hz [1], the method developed in this section applies. For liquid pipelines, in the case $R=0.6\sim0.8$ and $f>10^{-5}$ Hz [1], the method in Section 4.2 is recommended.

The ILI tools have a resolution limit in detecting crack depth. The best tool on the market may be limited to 0.5 mm or, in general, 1 mm in depth. At such a crack depth, the crack growth follows deep-crack growing behavior and the models developed in this work are broadly applicable. Table 2.2 already shows the crack depths required to reach a threshold K_{ISCC} at 21 MPa·m$^{1/2}$ [2] for different types of steel, pipe diameters, and wall thicknesses.

Given the pipe operating pressure or loading condition and the crack size, K_{max} may be calculated. K_{max} may be used to compare with K_{ISCC} if available, such as 20 MPa·m$^{1/2}$. If K_{ISCC} is known and $K_{max}<K_{ISCC}$, the CGR may be assumed to be zero. If K_{ISCC} is not known, the model of this work may be used to conservatively estimate the CGR by making K_{ISCC} zero.

When the model is determined to be feasible to use, the second step is to determine the model parameters from available field data and further predict CGR, pipe life, and reinspection interval.

4.1.2 Step 2: Determine Model Parameters from Field ILI Data

Under constant loading, Equation (2-6) may be used for field CGR prediction. With $K_{ISCC} = 0$, the prediction is more conservative or a greater CGR is obtained than if $K_{ISCC}>0$. With $K_{ISCC} = 0$, Equation (2-6) becomes

$$\dot{a} = \lambda_0[ln(K^2) - ln(\lambda_1)]^{\lambda_2} = \lambda_0 P \qquad (4\text{-}1)$$

where $\lambda_2 = 2.8$ (see Appendix 4.A) and $P = [ln(K^2) - ln(\lambda_1)]^{\lambda_2}$. λ_0 and λ_1 are unknown model parameters to be determined from field data.

Two crack depths obtained from a minimum of two ILI runs are required to determine λ_0 and λ_1. The detailed mathematical equations for using this method are presented in Appendix 4.A. Presented next are two hypothetical examples to show how this method can be used in the field. These two examples are developed for one crack, but the number of ILI runs is three and two, respectively. The example with three ILI runs is presented first.

<u>Three Depths of a Growing Crack Obtained from Three ILI Runs</u>

Suppose three depths of a growing crack on an X65 pipe with 20-in OD and 0.24-in wall thickness were reported to be a_1=1 mm, a_2=1.7 mm, and a_3=2.4 mm. It is assumed that these three depths resulted from three consecutive ILI runs with the first inspection interval 7 years and the second interval 5 years. It is given that this pipe is operating at 72% of specified minimum yield strength (SMYS).

The average CGRs during the first and second inspection intervals are $\bar{\dot{a}}_2$=0.10 mm/y and $\bar{\dot{a}}_3$=0.14 mm/y, respectively.

For a one-dimensional crack, under the previously described operating condition, the SIFs at the three crack depths are K_1=17.51, K_2=23.35, and K_3=31.26 MPa·m$^{0.5}$, respectively.

With λ_2=2.8, the two unknown parameters in Equation (4-1), λ_0 and λ_1, can be obtained. λ_1 may be calculated from this equation:

$$\frac{\bar{a}_3}{\bar{a}_2} = \frac{P_3}{P_1} \cdot \frac{P_2+P_1}{P_3+P_2} \tag{4-2}$$

where $P_i = [ln(K_i^2) - ln(\lambda_1)]^{2.8}$.

By an iteration method, λ_1=4.12 (MPa)^2·m. With λ_1 and $\bar{a}_3$, λ_0 can be calculated from

$$\lambda_0 = 0.5\bar{a}_3(P_3^{-1}+P_2^{-1}) \tag{4-3}$$

and the result is λ_0=0.0014 mm/y.

When the more accurate integration method (Appendix 4.A.1) is used to determine λ_0 and λ_1, λ_{1_int}=4.78 (MPa)^2·m and λ_{0_int}=0.0015 mm/y. Because they are close to the values obtained from the averaging method given by Equations (4-2) and (4-3), the approximation of Equation (4-2) to Equation (4-1) is acceptable. These results are summarized in Table 4-1 along with those in Section 4.1.3 from this same method.

Only Two Crack Depths Known from Two ILI Runs

Suppose only the first two ILI runs took place with their inspection interval still 7 years and the crack depths still 1 mm and 1.7 mm, respectively. If the crack age at the first ILI is 25 years and the initiation time can be neglected, the average CGR before the first ILI may be estimated to be $\bar{a}_1$=1 mm/25 years =0.04 mm/y. The average CGR between the two ILI runs is still $\bar{a}_2$=0.10 mm/y.

The following derivation given in Appendix 4.A-2 λ_1 may be calculated from this equation:

$$\frac{\bar{a}_2}{\bar{a}_1} = \frac{4P_2}{P_1+P_2} \tag{4-4}$$

An iteration method may be used to determine that λ_1=17.26 (MPa)^2·m.

With λ_1 and $\bar{a}_2$, λ_0 can be calculated from

$$\lambda_0 = \frac{\bar{a}_2(P_1+P_2)}{2P_1P_2} \tag{4-5}$$

and the result is λ_0=0.0041 mm/y.

When the more accurate integration method (Appendix 4.A.1) is used, λ_{1_int}=10.38 (MPa)^2·m and λ_{0_int}=0.0026 mm/y. Even though there are discrepancies between the predicted results from using the averaging and integration methods, the predicted remaining life of the pipe is close (Section 4.1.3). The previously outlined results are summarized in Table 4-2.

4.1.3 Step 3: Model Predictions and Verification

If the pipe is assumed to fail when the crack depth reaches 70% wall thickness or a_f=4.27 mm, the corresponding SIF is K_f=96.96 MPa·$m^{0.5}$. With the values of λ_0 and λ_1 in Equation (4-1) already determined, the pipe life controlled by the crack growth can be estimated. The pipe life estimation follows, considering three and two ILI runs, respectively.

Life Prediction Based on Three Crack Depths from Three ILI Runs

With use of λ_0 and λ_1 determined from the three ILI runs, the average CGR between the third ILI and at failure can be calculated from the following equation [similar to Equation (4-2)]:

$$\frac{\bar{\dot{a}}_f}{\dot{a}_3} = \frac{P_f}{P_2} \cdot \frac{P_3+P_2}{P_f+P_3} \tag{4-6}$$

where the subscript "f" refers to model properties at failure or here at the crack depth of 70% wall thickness. P_f can be obtained by using K_f.

Solving Equation (4-6) yields $\bar{\dot{a}}_f$=0.241 mm/y, the average CGR between the third ILI and failure. The remaining time to failure is thus determined to be

$$\Delta t_f = t_f - t_3 = \frac{a_f - a_3}{\bar{\dot{a}}_f} \tag{4-7}$$

The result is Δt_f =7.76 years. The total life of this pipeline would be 25+7+5+7.76=44.76 years. This is shown by the symbol "o" in Figure 4-1.

If taking the inspection interval as half of the remaining life, the fourth inspection should be performed at the fourth year.

When the more accurate integration method (Appendix 4.A.1) is used, $\bar{\dot{a}}_f$=0.255 mm/y and Δt_f =7.32 years, which are close to the values from the averaging method. The pipeline life is 44.32 years, shown by the blue "*" in Figure 4.1. The above average CGRs, remaining lives, and total lives obtained from averaging and integration methods can be seen in Table 4-1.

In Figure 4-1, the gray solid curve represents the predicted instant CGR. Understandably, it is always greater than or at least equal to the predicted average CGRs, which are shown by the broken lines. The average CGRs are obtained by the integration of instant CGR over a time interval divided by the time interval.

The average CGR between the first and second ILI run is shown by the broken line in black between the two diamond symbols. These two diamond symbols represent the actual average CGRs estimated from ILI data. The blue broken curve represents the predicted average CGRs from the third inspection to 70% of wall thickness. Each average CGR curve starts from the instant CGR at its cross point to the curve of instant CGR. From this point, the accumulated

increase of crack depth (equal to the integration of instant CGR over time) and increase of time starts to count and the average CGR is calculated by the ratio of these two values.

The accumulated increase of crack depth vs. pipe life is shown in Figure 4-2, where the two dark symbol "*" represent the pipe lives at the second and third ILIs and the blue symbol "*" represents the pipe life at failure. The curves between the three points are the predicted crack depths.

Life Prediction Based on Only the First Two ILI Runs

With only the first two ILI runs performed, the average CGR between the second ILI and at failure can be calculated from the following equation:

$$\frac{\bar{\dot{a}}_f}{\bar{\dot{a}}_2} = \frac{P_f}{P_1} \cdot \frac{P_2+P_1}{P_f+P_2} \tag{4-8}$$

The result is $\bar{\dot{a}}_f$=0.225 mm/y. The remaining time to failure may be calculated as

$$\Delta t_f = t_f - t_2 = \frac{a_f - a_2}{\bar{\dot{a}}_f} \tag{4-9}$$

and the result is Δt_f =11.41 years. The total pipeline life thus calculated is 25+7+11.41=43.41 years. This is shown in Figure 4-3, where the dark broken curve shows the predicted CGR between the first and second ILIs and the blue broken curve shows the same, but between the second ILI and pipe failure. These predictions were performed based on the data shown by the two leftmost black diamonds.

The pipe life is shown in Figure 4-3 by the rightmost blue circle. It is about 1 year less than if it is determined from data of three ILIs.

When the more accurate integration method is used, the remaining life obtained is Δt_f =10.94 years or the total life is 42.94 years. The corresponding average CGR is 0.235 mm/y, shown by the blue "*" symbol in Figure 4-3. By comparison, the nonintegration method is shown to be sufficiently accurate relative to the integration method. The above average CGRs, remaining lives, and total lives obtained from averaging and integration methods can be seen in Table 4-2.

Similar to Figure 4-1, the three diamond symbols in Figure 4-3 represent the actual CGRs, but the two left most were used in determining λ_0 and λ_1, or λ_{0_int} and λ_{1_int}. The broken curves represent the predicted average CGRs starting from their respective cross point, with the gray solid curve representing the predicted instant CGRs.

Model Realism Check and Improvement

When only the first two ILI runs were performed and the model parameters in Equation (4-1) were obtained in Step 2 to be λ_1=17.26 (MPa)^2·m and λ_0=0.0041 mm/y. The model is

used to calculate the average CGR at the fifth year from the second ILI, or at the time of the actual third ILI or Δt_{3x}= 5 years. The following equation is solved to predict the crack depth a_{3x} at the fifth year from the second ILI.

$$\frac{\bar{a}_{3x}}{\bar{a}_2} = \frac{P_{3x}}{P_1} \cdot \frac{P_2+P_1}{P_{3x}+P_2} \tag{4-10}$$

where $\bar{a}_{3x} = \frac{a_{3x}-a_2}{\Delta t_3'}$ and P_{3x} is the SIF corresponding to a_{3x}.

By solving Equation (4-10) with an iteration method, a_{3x}=2.54 mm, and the average CGR is 0.17 mm/y, which is shown in Figure 4-3 by the left empty cycle. This predicted cycle is close to the actual CGR shown by the rightmost diamond. This result suggests that in this case, using only the first two ILI results can reasonably predict crack depth at the third ILI and the average CGR between the second and third ILIs.

Optimization Method to Determine Model Parameters λ_0 and λ_1

When three or more CGRs are available, an optimization method may be used to determine λ_0 and λ_1. This method is presented in Appendix 4.A-3.

4.1.4 Step 4: Final Determination of CGR and Inspection Interval

The pipe life obtained from the model in Section 4.1.3 may be compared with the results obtained if the current industrial practice for estimating pipe remaining life is used.

In the current practice, two methods may be used to estimate the pipe life. In the first method, the average CGR between the second and third ILIs, or 0.14 mm/y, may be linearly extrapolated to 70% wall thickness and the remaining life obtained is 13.3 years or the pipe total life 50.3 years.

For the second method, a conservative CGR of 0.3 mm/y may be used [3]. The remaining life thus obtained is 6.2 years or the pipe total life is 43.2 years. This second method is more consistent with estimated pipe total life from the current model, which gives 44.8 years (based on data of three ILIs) or 43.4 years (based on data of two ILIs).

The model developed in this work may be considered one of the tools for predicting CGR and inspection intervals. It captures the crack growth mechanisms for deep cracks that the CGR tends to increase over time. By comparison, using the linear extrapolation method traditionally implemented in the field, the predicted CGR or inspection interval may be nonconservative or too long. Although in this case the use of the more conservative constant CGR of 0.3 mm/y yields approximately the same pipe life as predicted by the model, the use of constant CGR of 0.3 mm/y may lead to a smaller life and unnecessary inspection cost when the actual CGRs are smaller.

Because all models have their limitations, it would be necessary to obtain and compare all the CGRs available and make decisions by using the best judgment.

4.2 Procedure for Field Use of the High pH SCC CGR Model –Cyclic Loading

Similar to high pH SCC under constant loading, the following four steps are needed to make predictions of CGR and pipe life under cyclic loading.

4.2.1 Step 1: Data Collection and Feasibility Study

This procedure is the same as Section 4.1.1.

4.2.2 Step 2: Determine Model Parameters from Field ILI Data

When the crack growth is dominated by cyclic loading and the crack growth due to constant loading can be neglected, the method of predicting CGR is straightforward and given in Appendix 4.B. The following CGR model may be used:

$$\dot{a} = \beta \xi^n K^{2n} \tag{4-11}$$

where n=0.67 and $\xi = f(1-R)^2$.

When detailed data for pressure fluctuations are available, the detailed stress ratio and frequency can be determined. A hypothetical example is created to show how each step of the method is followed. For this example, simplified stress ratios and frequencies are used.

Suppose a pipeline is ILIed for the first time at the age of 25 years and a 1-mm-deep crack is found. During the next 7 years, the pipe experiences mainly four periods of stress ratios and frequencies:

- R_1=0.7 and f_1=0.0001 Hz for the first 3 years, or a subtotal cycle of m_1= 9,461
- R_2=0.75 and f_2=0.0002 Hz for the fourth year, or a subtotal cycle of m_2=6,307
- R_3=0.65 and f_3=0.00001 Hz for the fifth and sixth year, or a subtotal cycle of m_3=631
- R_4=0.7 and f_4=0.00005 Hz for the seventh year, or a subtotal cycle of m_4=1577

At the 7th year, ILI detected the same crack and the depth increased to 1.7 mm. The average CGR during the 7 years is thus 0.1 mm/y.

The previously described information alone is sufficient to determine the model parameter "β," with

$$\beta = \frac{\Delta a_2 (K_{max,2}^{-2n} + K_{max,1}^{-2n})}{2\sum_{k=1}^{N_2} f_{2,k}^{-1} \xi_{2,k}^{n}} \tag{4-12}$$

where N_2 is the total number of stress cycles during the 7 years, k is an arbitrary cycle with stress frequency $f_{2,k}$ and stress ratio of $R_{2,k}$, and $\xi_{2,k} = f_{2,k}\left(1 - R_{2,k}\right)^2$. The subscript "2" under f or ξ in Equation (4-12) represents the parameter confined between the first and second inspections.

For this example, the denominator on the right-hand side of Equation (4-12) may be simplified as

$$2\sum_{k=1}^{N_2} f_{2,k}^{-1}\xi_{2,k}^{n} = 2\sum_{i=1}^{4} n_{2,i} f_{2,i}^{-1}\xi_{2,i}^{n} \tag{4-13}$$

where i is an arbitrary period of the four; $n_{2,i}$, $f_{2,i}$, and $R_{2,i}$ are the total cycles, stress frequency, and stress ratio during the i^{th} period.

By solving Equation (4-12), β=5.53 (mm/y)·(MPa·$m^{0.5}$)$^{-2n}$. This is consistent with the result from the more accurate integration method (see Appendix 4.B), which gives β_{int}=5.44 (mm/y)·(MPa·$m^{0.5}$)$^{-2n}$. These results obtained from the averaging and integration methods are presented in Table 4-3.

With β obtained, the accumulated time interval from the first ILI to the j^{th} cycle ($1 \le j \le N_2$) and the crack depth $a_{1,j}$ can be determined from the following equations:

$$\Delta t_{2,j} = \sum_{k=1}^{j} f_{2,k}^{-1} \tag{4-14a}$$

and

$$K_{max,2,j}^{-2n} = -K_{max,1}^{-2n} + \frac{2\beta\sum_{k=1}^{j} f_{2,k}^{-1}\xi_{2,k}^{n}}{\Delta a_{2,j}} \tag{4-14b}$$

The average CGR during the j stress cycles after the first ILI is

$$\bar{\dot{a}}_{2,j} = \frac{a_{2,j} - a_1}{\Delta t_{2,j}} \tag{4-15}$$

Figure 4-4 shows the predicted instant CGR (four discontinuous solid curves) calculated from Equation (4-11) and the average CGR (blue broken curve) calculated from Equation (4-15) since the first ILI.

In Figure 4-4, the difference in CGR at different periods reflects the significant effect of stress frequency and ratio. The average CGR equals the integration of instant CGR over a time interval from the first ILI divided by the time interval. The average CGR increases during the first two periods due to the continuous increase of instant CGR over time. This average CGR, however, decreases in the last two periods because of the sudden drop of the instant CGR during the third period (due to the variation of stress frequency and ratio). In the fourth period, there is a sudden increase of instant CGR from the third to the fourth period, because the time interval of integration increases over time. The increase of average CGR is insignificant during the fourth period.

Corresponding to the variation of CGRs, the predicted accumulated crack depth during each period is shown in Figure 4-5. The two filled diamonds are the actual crack depths; the depth in between is predicted from the model. The slope at any point on this curve yields the

instant CGR in Figure 4-4, while the accumulated crack depth from the first ILI divided by the time interval from the first ILI gives the average CGR in Figure 4-4.

4.2.3 Step 3: Model Predictions and Verification

When the third ILI has to be scheduled when the crack size reaches a_f=70%×WT=4.27 mm, given the detailed stress frequency $f_{f,k}$ and stress ratio $R_{f,k}$, with the model parameter "β" known, the total stress cycle after the second ILI, N_f, may be obtained from [similar to Equation (4-12)]

$$\sum_{k=1}^{N_f} f_{f,k}^{-1} \xi_{f,k}^{n} = 0.5 \Delta a_f (K_{max,f}^{-2n} + K_{max,2}^{-2n}) \beta^{-1} \tag{4-16}$$

where the subscript "f" under f and ξ refers to the two variables confined within the time from the second ILI to failure.

When the stress frequency and ratio are constant, such as $f_f=10^{-4}$ /s and R_f=0.65, the total stress cycle may be calculated from

$$N_f = 0.5 f_f \Delta a_f (K_{max,f}^{-2n} + K_{max,2}^{-2n}) \beta^{-1} \xi_f^{-n} \tag{4-17}$$

With N_f, the pipe life can be estimated by

$$t_f = t_2 + \sum_{k=1}^{N_f} f_{f,k}^{-1} = t_2 + N_f f_f^{-1} \tag{4-18}$$

The average CGR between the second ILI and failure is

$$\bar{\dot{a}}_f = \frac{\Delta a_f}{\Delta t_f} \tag{4-19}$$

The pipe life and average CGR are thus determined to be t_f=39.5 years and $\bar{\dot{a}}_f$=0.341 mm/y, which is shown in Figure 4-6 by the rightmost empty circle. These numbers are close to the values obtained from the more accurate integration method (Appendix 4.A-2) shown in the figure by the rightmost symbol "*". Their values are t_{f_int}=38.5 years and $\bar{\dot{a}}_{f\_int}$=0.391 mm/y. If the inspection interval is taken as half of the pipe remaining life, Δt_f=7.5 years from Equation (4-18) vs. Δt_f=6.6 years from integration method, the small nonconservativeness the averaging method predicts (Equation (4-18)) is not significant.

Figure 4-6 also shows the variation of instant CGR (gray solid curve) and average CGR (blue broken curve) vs. pipe life determined from the integration method. The discontinuity of the blue curve results from the fact that after the second inspection, the average CGR starts from a different instant CGR and then averages over time. The corresponding accumulated crack depth is shown in Figure 4-7. The relation between the curve of crack depth and the instant and average CGRs was discussed earlier.

In both Figures 4-6 and 4-7, the predicted average CGR and accumulated crack depth at the fifth year following the second inspection are shown as the empty circle obtained from the averaging method and shown as the symbol "*" obtained from integration method. These two symbols are nearly overlapped, suggesting consistency of the predictions from the averaging and integration methods. The predicted depth from the averaging method is 3.06 mm, and the average CGR is 0.27 mm/y. The depth predicted from the integration method is 3.10 mm, and the average CGR is 0.28 mm/y.

Optimization Method to Determine Model Parameter β

When two or more estimated CGRs from ILIs are available, an optimization method may be used to determine the model parameter β. This method has been presented in Appendix 4.A-3.

If the third ILI was conducted at the fifth year following the second ILI and the crack depth is found to be 1.4 mm, the average CGR between the second and third ILI is 0.14 mm/y. Given the information from the first three ILIs, an optimization method may be used to determine β from

$$\beta = \frac{\sum_{i=1}^{m}\left[0.5\Delta a_{i+1}(K_{max,i+1}^{-2n}+K_{max,i}^{-2n})\cdot\sum_{k=1}^{N_{i+1}} f_{i+1,k}^{-1}\xi_{i+1,k}^{n}\right]}{\sum_{i=1}^{m}\left(\sum_{k=1}^{N_{i+1}} f_{i+1,k}^{-1}\xi_{i+1,k}^{n}\right)^{2}} \tag{4-20}$$

where i is an ILI interval and m is the total number of ILI intervals, equal to the number of ILIs minus 1. N_{i+1} is the total number of stress cycles during the i^{th} ILI interval.

For the example to be demonstrated here, m=2. When i=1 or during the first ILI interval, four periods must be considered as shown earlier. For the second ILI interval, the stress frequency and ratio are still assumed to be $f_3=10^{-4}$ /s and $R_3=0.65$. With an interval of 5 years, the total stress cycles are 15,768.

Equation (4-20) becomes

$$\beta = \frac{\Delta a_2(K_{max,2}^{-2n}+K_{max,1}^{-2n})\cdot\sum_{j=1}^{4}(n_{2,j}f_{2,j}^{-1}\xi_{2,j}^{n})+\Delta a_3(K_{max,3}^{-2n}+K_{max,2}^{-2n})\cdot N_3 f_3^{-1}\xi_3^{n}}{2\left(\sum_{j=1}^{4}(n_{2,j}f_{2,j}^{-1}\xi_{2,j}^{n})+N_3 f_3^{-1}\xi_3^{n}\right)^{2}} \tag{4-21}$$

The result is β=2.15, which is consistent with the predicted value of $\beta_{int}=2.12$ if the more accurate integration method is used. They are significantly different from its value obtained earlier when only two crack depths from the first two ILIs are used. This is because the crack depth at the third ILI (a_3), and the stress frequency and ratio since the second ILI are not at all associated with the β value determined earlier.

4.2.4 Step 4: Final Determination of CGR and Inspection Interval

Following the current industrial practice, if the average CGR between the first and second ILIs, or 0.1 mm/y, is used to linearly extrapolate to 70% wall thickness, the remaining life obtained is 25.7 years or the pipe total life 57.7 years.

If a conservative constant CGR of 0.3 mm/y is used, the remaining life thus obtained is 8.6 years or the pipe total life 40.6 years. This second method is more consistent with the estimated pipe total life from the current model, which gives 39.7 years.

As mentioned in Section 4.1.4, the model developed in this work may be considered an alternative tool for predicting CGRs and reinspection intervals. A comparison of these three methods shows that the linear extrapolation gives a much greater pipe life or reinspection interval than obtained if the more conservative constant CGR of 0.3 mm/y or the current model is used. In final determination of the reinspection interval, field experience may need to be used to select the most appropriate value.

4.3 Procedures for Field Use of the Near-Neutral pH SCC Model

The difference between high pH and near-neutral pH SCCs in predicting CGRs is that the latter would not be likely to occur if the load is maintained constant, such as for gas transmission pipelines. For near-neutral pH SCC, only corrosion fatigue is of concern. The procedure for field prediction of near-neutral pH SCC CGR is similar to that of high pH SCC and consists of the four steps described next.

4.3.1 Step 1: Data Collection and Model Feasibility Study

Similar to the field procedure in Section 4.1 for high pH SCC, the same data in Section 4.1.1 must be collected. After a review and analysis of the data, the type of SCC, high pH or near-neutral pH, must be determined. Only near-neutral pH SCC is of interest here.

Because dormancy may not need to be considered for near-neutral pH SCC following the discussion given in Section 3.5, the method developed here is applicable to predicting CGRs as soon as a crack detected by an ILI is confirmed. This method also accounts for dormancy if it is known to exist. Given the pipe operating pressure or loading condition and the crack size, K_{max} can be calculated. Only when the crack growth is mainly driven by stress fluctuations is the method applicable. Conditions with small stress frequency ($<10^{-5}$ /s) and large stress ratio (>0.8) may not cause any appreciable crack growth for near-neutral pH SCC.

When the model is determined to be feasible to use, the second step is to determine the model parameters from available field data. With the model fully defined, the CGR, pipe life and inspection interval can then be predicted from the following steps.

4.3.2 Step 2: Determine Model Parameters from Field ILI Data

For near-neutral pH SCC, the crack growth mechanism is found to be similar to true fatigue and its rate is controlled by cyclic loading. The method of predicting CGR is nearly exactly the same as given in Appendix 4.B or Section 4.2.2, while the equation of CGR must be modified. For near-neutral pH SCC, the CGR model is

$$\dot{a} = A_H \eta K_{max}^6 \tag{4-22}$$

where $\eta = f^{\frac{8}{10}}(1-R)^4$.

Between i[th] and (i+1)[th] ILIs, Equation (4-22) may be written as

$$\int_{a_i}^{a_{i+1}} K_{max}^{-6}\, da = A_H \sum_{k=1}^{N_{i+1}} f_{i+1,k}^{-1}\, \eta_{i+1,k} \tag{4-23}$$

To avoid integration, the term on the left of Equation (4-23) may be approximated by the Newton-Cores equation [4]:

$$\int_{a_i}^{a_{i+1}} K_{max}^{-6}\, da = \Delta a_{i+1} \sum_{l=1}^{5} (\lambda_l\, K_{max,l}^{-6}) \tag{4-24}$$

where λ_l (l=1 to 5) are core coefficients, equal to $\frac{7}{90}$, $\frac{16}{45}$, $\frac{2}{15}$, $\frac{16}{45}$, and $\frac{7}{90}$ for subscript "l" varying from 1 to 5. Assume $h = \Delta a_{i+1}/4$ and $K_{max,l}$ (l=1~5) corresponds to λ_l at the crack depth $a_l = a_i + h(l-1)$.

The same example given in Section 4.2.2 may be used here to demonstrate step by step how the model may be used to predict CGR for near-neutral pH SCC. Between the first and second ILIs, it is assumed that a pipe experiences the same four periods and the same stress ratio, frequency, and cycles as given in Section 4.2.2. As the crack depth increases from 1 mm at the first ILI to 1.7 mm at the second ILI during a 7-year interval, the average CGR is 0.1 mm/y.

The previously described information can be used to determine the parameter "A_H", with

$$A_H = \frac{\Delta a_2 \sum_{l=1}^{5} (\lambda_l K_{max,l}^{-6})}{\sum_{k=1}^{N_2} (f_{2,k}^{-1}\, \eta_{2,k})} \tag{4-25}$$

where N_2 is the total stress cycles during the 7 years, k is an arbitrary cycle with stress frequency $f_{2,k}$ and stress ratio $R_{2,k}$, and $\eta_{2,k} = f_{2,k}^{\frac{8}{10}}(1-R_{2,k})^4$. The subscript "2" under f or ξ in Equation (4-25) signifies the two parameters confined between the first and second ILIs.

For the example being studied, the denominator on the right-hand side of Equation (4-25) may be simplified as $\sum_{k=1}^{N_2} f_{2,k}^{-1} \xi_{2,k}^{n} = \sum_{i=1}^{4} n_{2,i} f_{2,i}^{-1} \xi_{2,i}^{n}$, where i is an arbitrary period of the four; $n_{2,i}$, $f_{2,i}$, and $R_{2,i}$ are the total cycles, stress frequency, and stress ratio during the i[th] period.

From Equation (4-25) A_H=4.42×10^{-4} (mm/y)·(MPa·m$^{0.5}$)$^{-6}$. This is nearly the same as the value obtained from the more accurate integration method or Equation (4-23), which also gives $A_{H\text{-}int}$=4.42×10^{-4} (mm/y)·(MPa·m$^{0.5}$)$^{-6}$.

With A_H obtained, the accumulated time interval from the first ILI to the jth stress cycle ($1 \le j \le N_2$) and the crack depth $a_{2,j}$ can be determined by

$$\Delta t_{2,j} = \sum_{k=1}^{j} f_{2,k}^{-1} \tag{4-26a}$$

and

$$\Delta a_{2,j} \sum_{l=1}^{5} (\lambda_l K_{max,l}^{-6}) \; + A_H \sum_{k=1}^{j} f_{2,k}^{-1} \eta_{2,k} = 0 \tag{4-26b}$$

where $\Delta a_{2,j} = a_{2,j} - a_1$ and $K_{max,l}$ (l=1~5) corresponds to its value at the crack depth $a_l = a_1 + h(l-1)$ and $h = \Delta a_{2,j}/4$.

The average CGR during the j stress cycles from the first ILI is

$$\bar{a}_{2,j} = \frac{a_{2,j} - a_1}{\Delta t_{2,j}} \tag{4-27}$$

Figure 4-8a shows the instant CGR (four dark solid curves) calculated from Equation (4-22) and the average CGR (the blue curve) calculated from Equation (4-27) at any stress cycle between the first two ILIs. The result is similar to that shown in Figure 4-4. Corresponding to the variation of CGRs, the predicted accumulated crack depth during each period is shown in Figure 4-8b.

4.3.3 Step 3: Model Predictions

When the pipe remaining life is considered to be at the crack size reaching a_f=70%×WT=4.27 mm, given detailed stress frequency $f_{f,k}$ and stress ratio $R_{f,k}$, with the model parameter "A_H" known, the total stress cycle after the second ILI, N_f, can be determined by

$$\sum_{k=1}^{N_f} f_{f,k}^{-1} \eta_{f,k} = \Delta a_f A_H^{-1} \sum_{l=1}^{5} (\lambda_l K_{max,l}^{-6}) \tag{4-28}$$

where the subscript "f" under f and η refers to the two variables confined within the time interval between the second ILI and failure.

When the stress frequency and ratio are constant, such as f_f=10^{-5} /s (10 times lower than that used in Section 4.2.3) and R_f=0.65, the total stress cycle can be calculated from

$$N_f = f_f \eta_f \Delta a_f A_H^{-1} \sum_{l=1}^{5} (\lambda_l K_{max,l}^{-6}) \tag{4-29}$$

With N_f, the pipe life can be estimated by

$$t_f = t_2 + \sum_{k=1}^{N_f} f_{f,k}^{-1} = t_2 + N_f f_f^{-1} \quad (4\text{-}30)$$

The average CGR between the second ILI and pipe failure is

$$\bar{\dot{a}}_f = \frac{\Delta a_f}{\Delta t_f} \quad (4\text{-}31)$$

The pipe life and average CGR are determined to be t_f=35.7 years and $\bar{\dot{a}}_f$=0.693 mm/y, respectively. They are shown in Figure 4-9(a) as the rightmost empty circle. These values are nearly the same as their values obtained from the more accurate integration method shown by the rightmost symbol "*". They are t_{f_int}=35.7 years and $\bar{\dot{a}}_{f\_int}$=0.699 mm/y. These results obtained from the averaging and integration methods are presented in Table 4-4.

Figure 4-9(a) also shows the instant CGR, which increases over time dramatically due to its strong dependence on SIF as shown by Equation (4-22). The instant CGR at the crack depth of 70% wall thickness is incredibly high, more than several hundred millimeters per year. The corresponding accumulated crack depth is shown in Figure 4-9(b), which also increases progressively over time because of the strong dependence of the CGR on SIF.

4.3.4 Step 4: Final Determination of CGR and Inspection Interval

The pipe life obtained from the model in Section 4.3.3 may be compared with the results obtained if the current industrial practice for estimating pipe remaining life is used.

In the current practice, two methods may be used to estimate the pipe life. In the first method, the average CGR between the first and second ILIs, or 0.1 mm/y, may be linearly extrapolated to 70% wall thickness and the remaining life obtained is 25.7 years or the pipe total life 57.7 years. For the second method, a conservative CGR of 0.6 mm/y may be used. The remaining life thus obtained is 4.3 years, or the pipe total life is 36.3 years. The latter is close to the estimated pipe total life from this model, which is 35.7 years.

The CGR predicted from the empirical equation or Equation (4-22) (with A_H=1.5x10^{-15} MPa^{-6}m^{2}s$^{1/5}$ applying only for the growing time of a crack) is very high as soon as the dormancy region Chen et al.[5] defined is passed. With such a rate maintained continuously, the pipe would fail within months if not weeks, as soon as ILI detects a crack. This prediction largely deviates from field observations that the crack can grow at a rate that is one or two orders of magnitude lower. Although Chen et al. developed a crack dormancy theory to counter this discrepancy, and the theory appears to suggest SCC cracks in the field are usually dormant (the only way that a much smaller average CGR can be predicted), this theory contradicts the observation from the full-scale pipe test of Zhang et al. [6], which grows in the dormancy region Chen et al defined. With consideration of the time of crack dormancy, some tedious calculation may be necessary to determine the average CGR. When possible, as an alternative, the CGR obtained from the method of Chen et al. [5] may also be compared in this step.

All of the previously outlined CGRs obtained from different methods need to be evaluated and a decision made to choose the most reasonable rate and inspection interval.

4.4 Summary

Step-by-step procedures were developed for applying the CGR models to predicting field CGRs under both high pH and near-neutral pH SCC conditions. Examples were provided to show how each step of the procedure is actually implemented. The procedures are straightforward and, if selected, should be able to be implemented in the field conveniently.

4.5 References

1. J. A. Beavers, Near-Neutral pH SCC: Dormancy and Re-Initiation of Stress Corrosion Cracks, Final Report for Gas Research Institute, GPI-05/0009, August 2004.
2. R.N. Parkins, B.S. Greenwell, Met. Sci. 11, 1977, 405-413.
3. A.D. Batte, R.R. Fessler, S.C. Rapp, Severity of Stress Corrosion Cracks in Pipelines—Categories and Responses, NACE/2008, paper no. 08675.
4. Q.Y. Li, N.C. Wang, D.Y. Yi, Numerical Analysis (in Chinese), Huazhong University of Science and Technology Press, third edition (1988), 129.
5. W. X. Chen, R. Kania, R. Worthingham, S. Kariyawasam, Crack Growth Model of Pipeline Steels in Near-Neutral pH Soil, Proceedings of the Biennial International Pipeline Conference, IPC2008-64475, Calgary, AB, Canada, 2008, 1-10.
6. W. Zhang, B. Tyson, G. Shen, R. W. Revie, G. Williams, D. Bibby, Effects of Operating Practices on Crack Dormancy and Growth, Report for Gas Research Institute, GPI-05/8668, CANMET, MTL-2005-10, 2005.

Table 4.1. Result Summary from the High pH SCC Model Under Constant Loading Condition; Results based on 2nd and 3rd ILI Data

	Given Crack Depths from ILIs (mm)			Estimated CGR by the ILI data (mm/y)		Model Parameters		Predicted Pipe Life at Failure* (Year)	Predicted CGR at Failure (mm/y)
	1st ILI	2nd ILI	3rd ILI	2nd ILI	3rd ILI	λ_0	λ_1		
Averaging method	1	1.7	2.4	0.1	0.14	0.0014	4.12	44.8	0.241
Integration method	1	1.7	2.4	0.1	0.14	0.0015	4.78	44.3	0.255

* Pipe life at the 3rd inspection is 37 years.

Table 4.2. Result Summary from the High pH SCC Model Under Constant Loading Condition; Results based on 1st and 2nd ILI Data

	Given Crack Depths from ILIs (mm)		Estimated CGR by the ILI data (mm/y)		Model Parameters		Predicted Pipe Life at Failure* (Year)	Predicted CGR at Failure (mm/y)	Predicted CGR at Scheduled 3rd ILI (mm/y)
	1st ILI	2nd ILI	1st ILI	2nd ILI	λ_0	λ_1			
Averaging method	1	1.7	0.04	0.1	0.0041	17.3	43.4	0.225	0.162
Integration method	1	1.7	0.04	0.1	0.0026	10.38	42.9	0.235	0.167

* Pipe life at the 2nd inspection is 32 years.

Table 4.3. Result Summary from the High pH SCC Model Under Cyclic Loading Condition

	Given Crack Depths from ILIs (mm)		Estimated CGR by the ILI data (at the End of 4th Period) (mm/y)	Model Parameter	Predicted CGRs since 1st ILI at the End of (mm/y)			Predicted Pipe Life at Failure* (Year)	Predicted CGR at Failure (mm/y)	Predicted CGR at Scheduled 3rd ILI (mm/y)
	1st ILI	2nd ILI			1st Period	2nd Period	3rd Period			
Averaging method	1	1.7	0.1	5.53	0.12	0.13	0.10	39.5	0.342	0.273
Integration method	1	1.7	0.1	5.44	0.12	0.13	0.10	38.6	0.391	0.280

* Pipe life at the 2nd inspection is 32 years.

Table 4.4. Result Summary from the Near-Neutral pH SCC Model Under Cyclic Loading Condition

	Given Crack Depths from ILIs (mm)		Estimated CGR by the ILI data (at the End of 4th Period) (mm/y)	Model Parameter (mm/y)·(MPa·m$^{0.5}$)$^{-6}$	Predicted CGRs since 1st ILI at the End of (mm/y)			Predicted Pipe Life at Failure* (Year)	Predicted CGR at Failure (mm/y)	Predicted Stress Cycles from 2ILI to Failure
	1st ILI	2nd ILI			1st Period	2nd Period	3rd Period			
Averaging method	1	1.7	0.1	4.42×10^{-4}	0.092	0.101	0.088	35.7	0.533	1159
Integration method	1	1.7	0.1	4.42×10^{-4}	0.092	0.101	0.088	35.7	0.534	1156

* Pipe life at the second inspection is 32 years.

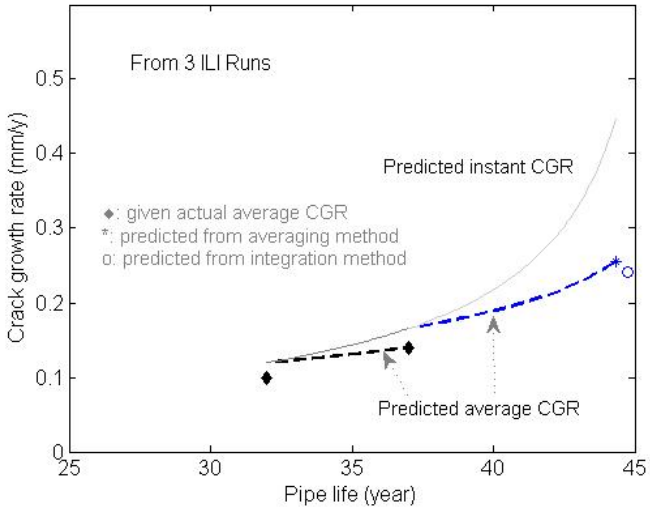

Figure 4-1. Predicted Instant and Average CGR versus Pipe Life By Use of Data from Three ILIs.

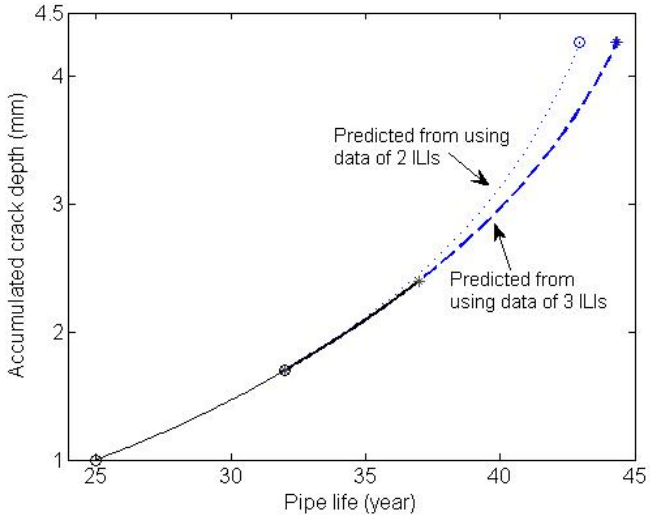

Figure 4-2. Accumulated Crack Depth versus Pipe Life By Use of Data From Three and Two ILIs.

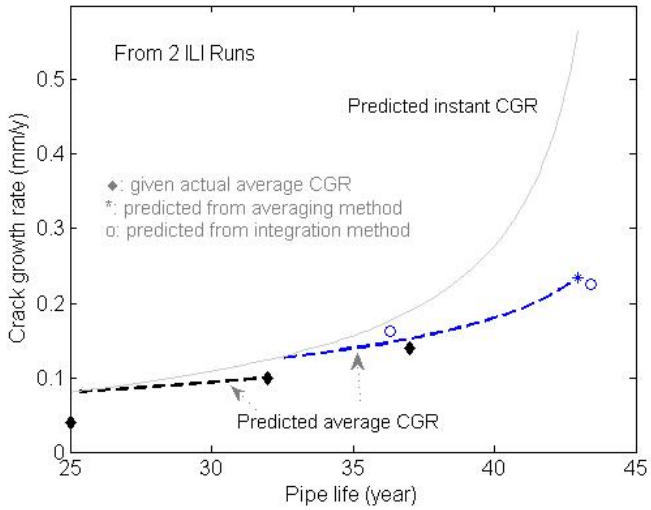

Figure 4-3. Predicted Instant and Average CGR versus Pipe Life By Use of Data from Two ILIs.

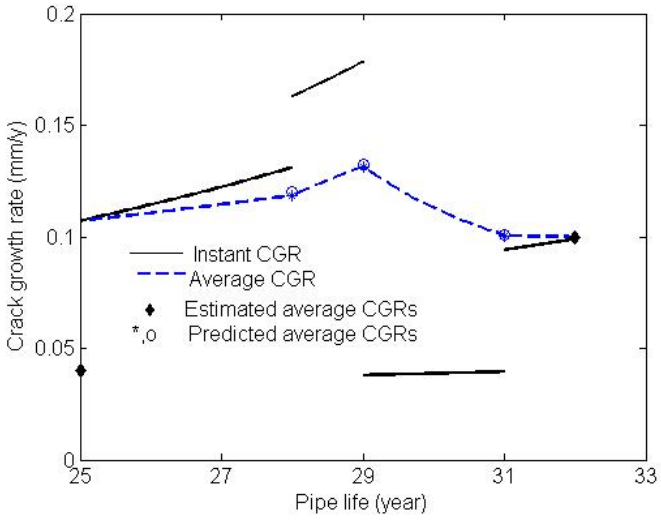

Figure 4-4. Predicted Instant and Average CGR versus Pipe Life Between the First and Second ILIs.

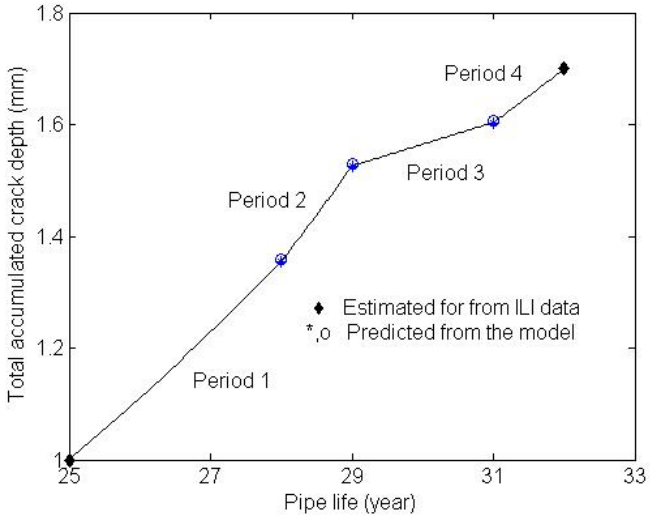

Figure 4-5. Predicted Accumulated Crack Depth versus Pipe Life Between the First and Second ILIs.

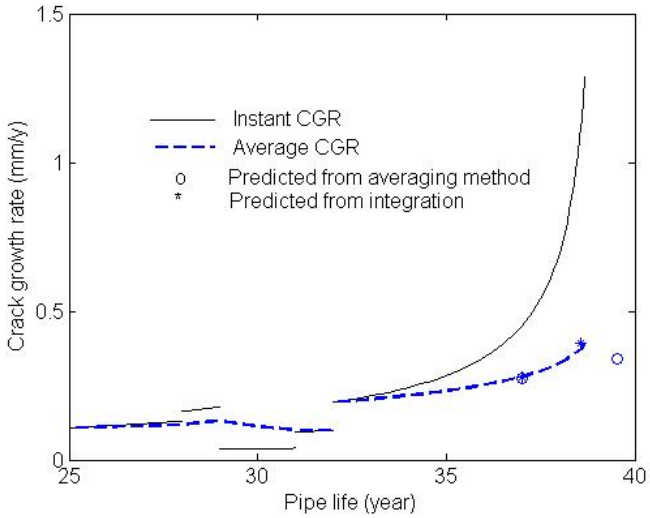

Figure 4-6. CGRs versus Pipe Life Before and After the Second ILI.

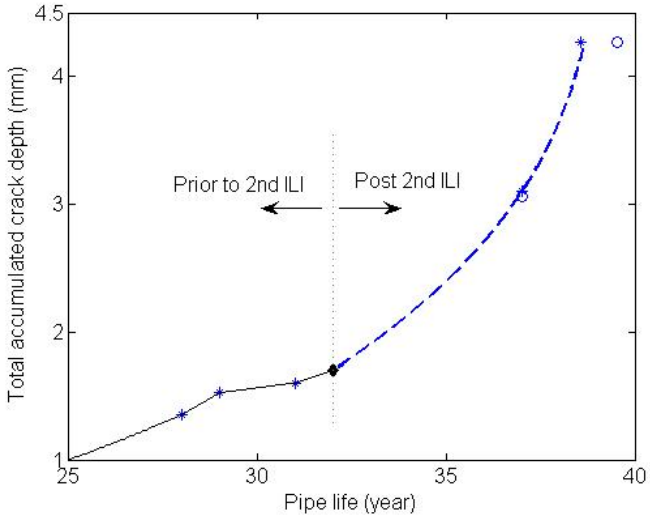

Figure 4-7. Total Accumulated Crack Depth versus Pipe Life Before and After the Second ILI.

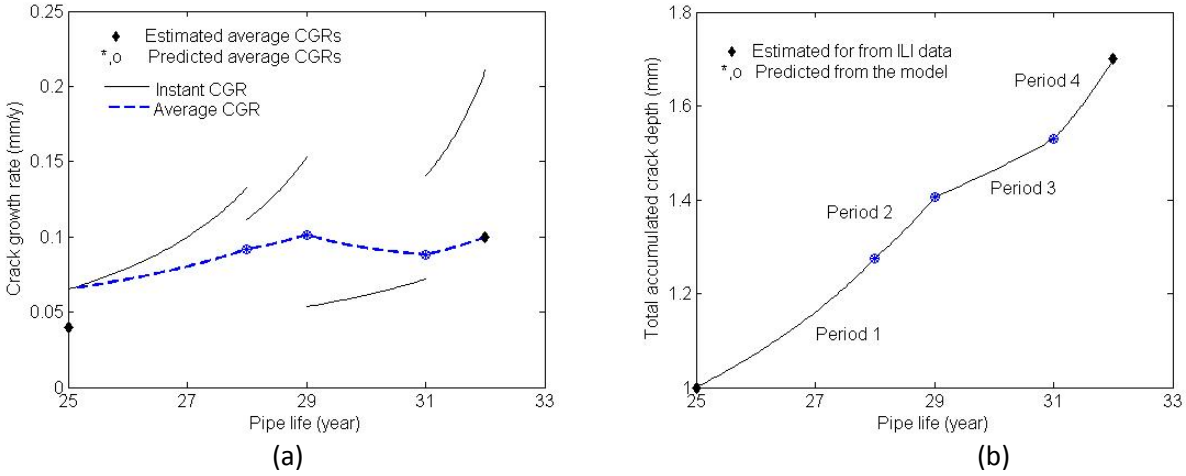

Figure 4-8. (a) Predicted Instant and Average CGR and (b) Accumulated Crack Depth versus Pipe Life Between the First and Second ILIs.

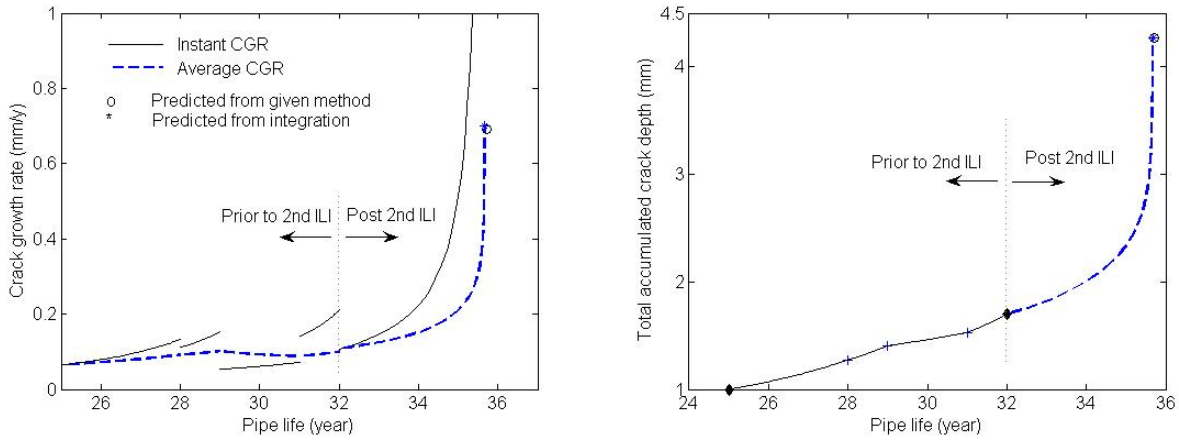

Figure 4-9. (a) CGRs and (b) Accumulated Crack Depth versus Pipe Life Before and After the Second ILIs.

5.0 CONCLUSIONS AND RECOMMENDATIONS

5.1 Conclusions

5.1.1 High pH SCC

Crack growth rate models were developed for predicting pipeline high pH stress corrosion CGRs under both constant and cyclic loading conditions. These models were developed on the basis that the effect of mass transfer within cracks can be neglected for concentrated carbonate and bicarbonate solution buffers often found in field conditions.

Results predicted from the high pH CGR models are shown to be consistent with experimentally measured data for consistent conditions. This consistency suggests that the models are capable of predicting the trends of high pH stress corrosion CGRs and can be used for field application with calibration of field data and experience.

Step-by-step procedures were developed for applying the CGR models to predicting field CGRs. The procedures for constant and cyclic loading conditions were presented separately. Examples were provided for both constant and cyclic loading conditions to demonstrate how each step of the procedure can be conveniently implemented in the field.

5.1.2 Near-Neutral pH SCC

An improved CGR model was presented for near-neutral pH SCC of buried pipelines. The basis of the current model is that the crack growth is controlled by hydrogen embrittlement mechanism.

An improvement over this prior work is that the model can now account for the effect on CGR by external solution pH and pipe potential. This effect is embedded in a relation developed between them and the atomistic hydrogen concentration in steel.

Step-by-step procedures were developed for applying the CGR models to predicting field CGRs. Examples were provided to show how each step of the procedure can be implemented for field prediction.

5.1.3 Workshop

A live on-line workshop was held by PHMSA in June 2011 open to the entire pipeline industry. The aim was to make the widest possible transfer of the technologies developed in this work to the pipeline industry.

5.2 Recommendations

Collect and analyze field data from the pipeline industry for further model validation.

Develop and perform critical experiments to generate high quality data to validate the current models and improve the industry's understanding of cracking mechanisms.

Extension of the current CGR model to include the specific effect of soil chemistry on CGR.

Improve the model for near-neutral pH SCC to include physical mechanisms of crack growth similar to the high pH SCC CGR model.

Appendix 2.A—Film Rupture and Anodic Dissolution Mechanisms

For high pH SCC of pipelines, it has been widely accepted that the crack growth follows film rupture and an anodic dissolution mechanism [1-2] so that the CGR may be formulated in accordance with Faraday's law [3]

$$\dot{a} = \frac{M}{zF\rho} Q \frac{\dot{\varepsilon}_{ct}}{\varepsilon_F} \tag{2.A–1}$$

where F is Faraday's constant; M and z are the molar mass of iron and the moles of electrons to be exchanged when a mole of steel is oxidized, respectively; Q is the electric charge passed between two successive film rupture events; $\dot{\varepsilon}_{ct}$ is the strain rate at the crack tip; and ε_F is the rupture ductility of passive film.

The cyclic period of a film rupture event is the ratio of film rupture strain over the crack tip strain rate written as

$$t_f = \varepsilon_F / \dot{\varepsilon}_{ct} \tag{2.A–2}$$

where ε_f and t_f are film rupture strain and the cyclic period, respectively.

The repassivation kinetics has been found to follow [4-5]

$$i_a = i_a^* \left(\frac{t}{t_0}\right)^{-n} \qquad t \geq t_0 \tag{2.A–3}$$

i_a^* is the anodic current density while the surface is fully activated. The repassivation exponent n is generally in a range of 0.3 to 1 [3]. When $t < t_0$, the bare metallic surface created by the film rupture is film free. The values of repassivation kinetic parameters (i_a^*, n, t_0) are the functions of the local chemical environments at the crack tip, which in turn depend on the corrosion reactions, mass transport, and external corrosive environments [3].

In general, $t_0 \ll t_f$. When the contribution to crack growth by the dissolution within t_0 from the film rupture can be neglected, substituting Equation (2.A–3) into Equation (2.A–1) yields [3]

$$\dot{a} \approx A \dot{\varepsilon}_{ct}^n \tag{2.A-4}$$

where $A = \frac{\dot{a}^*}{1-n} \left(\frac{t_0}{\varepsilon_F}\right)^n = \frac{i_a^*}{1-n} \frac{M}{zF\rho} \left(\frac{t_0}{\varepsilon_F}\right)^n$.

The maximum CGR occurs during the time of t_0 before film repassivation begins. Then, $\dot{a}_{max} = i_a^* \frac{M}{zF\rho}$. The minimum CGR occurs at the time when the crack tip is well passivated. Then, $\dot{a}_{min} = i_p \frac{M}{zF\rho}$, where i_p is the passive current density.

Appendix 2.B—Method of Evaluating Stress Intensity Factor on Pipelines

Before the crack penetrates the pipe wall, it is normally regarded as a partially penetrated half-elliptical surface crack. For a crack with this kind of geometry, its SIF is given by [9]

$$K_I = Y\sigma\sqrt{\frac{\pi a}{E_c}} \tag{2.B–1}$$

The crack shape factor E_c is a square of the completed elliptical integral of the second kind and is approximately given as a function of the aspect ratio of crack a/c

$$E_c = 1 + 1.464\left(\frac{a}{c}\right)^{1.65} \tag{2.B–2}$$

The geometric factor of the crack is a function of the crack and pipe geometry

$$Y = Y\left(\frac{a}{w}, \frac{a}{c}, \frac{w}{R}, \theta\right) \tag{2.B–3}$$

where a and c are the depth and half-surface length of crack, respectively; the angle θ is defined as shown in Figure 2.B–1; and w and R are the wall thickness and the internal radius of pipe, respectively.

For a pipe with a small w/R ratio (for instance, <1/50) subjected to internal pressure, the value of Y is approximately independent of pipe diameter. The pipe containing a surface crack in a longitudinal direction can be approximately treated as a plate with a surface crack subjected to uniform tension.

At the deepest point of surface crack ($\theta = 90^0$), Y can be approximated by ($\frac{a}{w} \le 0.8, \frac{a}{c} \le 1$) [10]

$$Y = B_0 + B_1\left(\frac{a}{w}\right)^2 + B_2\left(\frac{a}{w}\right)^4 + B_3\left(\frac{a}{w}\right)^6 \tag{2.B–4}$$

$$B_0 = 1.0929 + 0.2581\left(\frac{a}{c}\right) - 0.7703\left(\frac{a}{c}\right)^2 + 0.4394\left(\frac{a}{c}\right)^3 \tag{2.B–4a}$$

$$B_1 = 0.456 - 3.045\left(\frac{a}{c}\right) + 2.007\left(\frac{a}{c}\right)^2 + \frac{1.0}{0.147+\left(\frac{a}{c}\right)^{0.688}} \tag{2.B–4b}$$

$$B_2 = 0.995 - \frac{1.0}{0.027+\left(\frac{a}{c}\right)} + 22.000\left(1.0 - \frac{a}{c}\right)^{9.953} \tag{2.B–4c}$$

$$B_3 = -1.459 + \frac{1.0}{0.014+\left(\frac{a}{c}\right)} - 24.211\left(1.0 - \frac{a}{c}\right)^{8.071} \tag{2.B–4d}$$

The aspect ratios of cracks detected in real pipelines are very small. As a result, the cracks can be approximately treated as one dimensional. If we regard the cracks in the pipe

longitudinal direction as a single edge notch tensile panel with width, the SIF is formulated by [9]

$$K_I = Y\left(\frac{a}{w}\right)\sigma\sqrt{w} \tag{2.B–5}$$

where σ is the hoop stress produced by the internal pressure. When $\sigma = \sigma_{max}$, $K_I = K_{Imax}$.

The nondimensional coefficient *Y* is given by

$$Y\left(\frac{a}{w}\right) = \left(0.752 + \frac{0.202a}{w} + 0.37\left(1 - \sin\left(\frac{\pi a}{2w}\right)\right)^3\right)\frac{\sqrt{2\tan\left(\frac{\pi a}{2W}\right)}}{\cos\left(\frac{\pi a}{2W}\right)} \tag{2.B–6}$$

Equation (2.B-5) is applicable for thin-walled-pipes with a large diameter (*D/w* <50). Accordingly, when the pipe wall thickness *w* and the maximum hoop stress σ_{max} (or the maximum internal pressure P_{max}) are constant, K_{Imax} will be solely determined by the crack size *a* (or *a/w*), if the stresses produced by the soil movement play a minor role.

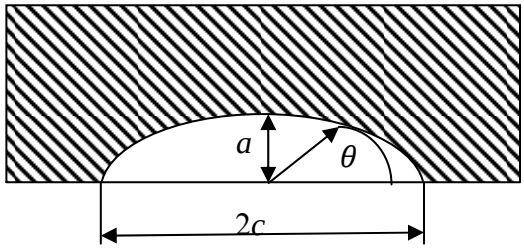

Figure 2.B–1. C–1 Geometry of an Elliptical Surface Crack.

Appendix 2.C—Magnitude Comparison of Components Due To Crack Tip Advance and SIF Change to CTSR Under Constant Load

Under constant load, the crack tip strain rate (CTSR) reported by Shoji and associates [8,11] may be written as

$$\dot{\varepsilon}_{ct} = \left(2\frac{\dot{K}}{K} + \frac{\dot{a}}{r_0}\right)\frac{N^*}{N^*-1}\frac{\sigma_y}{E}\left\{ln\left[\frac{\lambda}{r_0}\left(\frac{K}{\sigma_y}\right)^2\right]\right\}^{\frac{1}{N^*-1}} \quad (2.C\text{–}1)$$

and the equation reported by M.M. Hall [13] is

$$\dot{\varepsilon}_{ct} = \frac{2N}{1+N}\frac{\sigma_y}{E}\left(\frac{pK^2}{r_0\sigma_y^2}\right)^{\frac{N}{N+1}}\frac{\dot{K}}{K} + \frac{2\beta N}{N-1}\frac{\sigma_y}{E}\frac{\dot{a}}{r_0}\left\{ln\left[\frac{\lambda}{r_0}\left(\frac{K}{\sigma_y}\right)^2\right]\right\}^{\frac{N+1}{N-1}} \quad (2.C\text{-}2)$$

Note that Hall [13] missed the factor of "2" when deriving the far right term of Equation (2.C–2).

For a surface crack with small aspect ratio on the external surface of a thin-walled-pipe (*D/w* <50),

$$K = Y\left(\frac{a}{w}\right)\sigma\sqrt{w} \quad (2.C\text{–}3)$$

and

$$Y\left(\frac{a}{w}\right) = \left(0.752 + 0.202a/w + 0.37\left(1 - \sin\left(\frac{\pi a}{2w}\right)\right)^3\right)\sqrt{2\tan\left(\frac{\pi a}{2W}\right)}/\cos\left(\frac{\pi a}{2w}\right) \quad (2.C\text{–}4)$$

The first term in Equation (2.C–1) or (2.C–2) is the CTSR component produced by the change of SIF due to crack propagation, and the second term is produced by crack tip advance. Equation (2.C–2) can also be written as

$$\dot{\varepsilon}_{ct} = \dot{a}\{\emptyset_{\dot{K}} + \emptyset_{\dot{a}}\} \quad (2.C\text{–}5)$$

with $\emptyset_{\dot{K}} = \frac{2N}{N+1}\frac{\sigma_y}{YE}\frac{dY}{da}\left(\frac{pK^2}{r_0\sigma_y^2}\right)^{\frac{N}{N+1}}$ and $\emptyset_{\dot{a}} = \frac{2\beta N}{N-1}\frac{\sigma_y}{E}\frac{\dot{a}}{r_0}\frac{\sigma_y}{E}\left\{ln\left[\frac{\lambda}{r_0}\left(\frac{K}{\sigma_y}\right)^2\right]\right\}^{\frac{N+1}{N-1}}$.

Under constant loading condition and in the range of interest with SIF, it was found that $\frac{Y'}{Y} \ll \frac{1}{r_0}$ (Figure 2.C–1) and $\emptyset_{\dot{K}} \ll \emptyset_{\dot{a}}$ (Figure 2.B–2). Note that $\frac{\dot{K}}{K} = \frac{dK}{da}\frac{\dot{a}}{K} = \frac{Y'}{Y}\dot{a}$. For the previous reason, Equation (2.C–1) can be simplified into

$$\dot{\varepsilon}_{ct} = \frac{\dot{a}}{r_0}\frac{N^*}{N^*-1}\frac{\beta\sigma_y}{E}\left\{ln\left[\frac{\lambda}{r_0}\left(\frac{K}{\sigma_y}\right)^2\right]\right\}^{\frac{1}{N^*-1}} \quad (2.C\text{–}6)$$

and Equation (2.C–2) can be approximated by:

$$\dot{\varepsilon}_{ct} \approx \frac{2\beta N}{N-1}\frac{\sigma_y}{E}\frac{\dot{a}}{r_0}\left\{ln\left[\frac{\lambda}{r_0}\left(\frac{K}{\sigma_y}\right)^2\right]\right\}^{\frac{N+1}{N-1}} \quad (2.C–7)$$

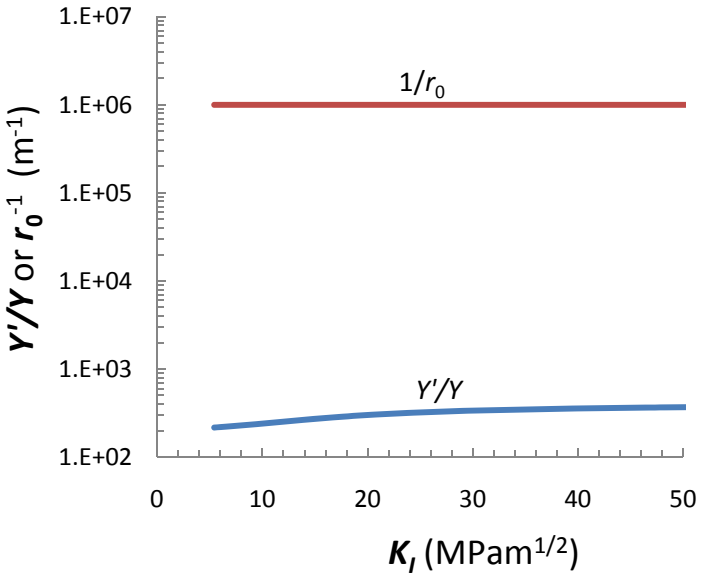

Figure 2.C–1. Comparison of *Y'/Y* vs. $1/r_0$

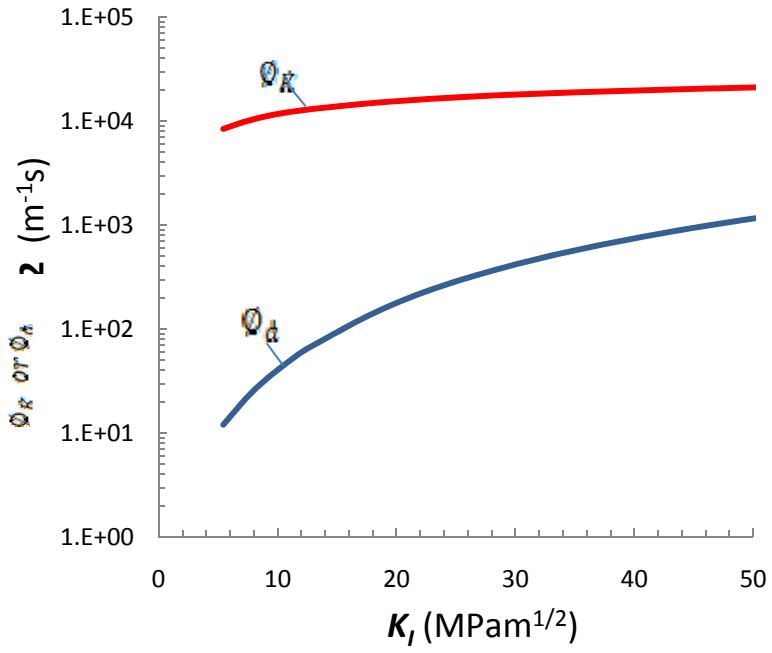

Figure 2.C–2. Comparison of $\phi_k vs. \phi_a$

Appendix 2.D—Crack Tip Strain Rate Under Cyclic Loading

Lidbury recommended the following crack tip strain rate expression [16]

$$\dot{\varepsilon}_{ct} = \varepsilon_0 f \Delta \mathrm{K}^2 = \varepsilon_0 f (1-R)^2 K_{max}^2 \qquad \text{(2.D–1)}$$

where the stress ratio is $R = \frac{K_{min}}{K_{max}}$ and ε_0 is a material constant depending on the environment. In a corrosive environment, incorporation of hydrogen into material or the adsorption of certain species on the surface may alter the mechanical properties of the material.

There is a threshold stress intensity, $K_{ISCC,}$ below which a long crack, under action of either sustained load or cyclic load, stops propagating. To predict CGR including the region of threshold, Equation (2.D–1) needs to be modified.

There is abundant evidence that the crack tip cannot open until the SIF reaches a critical value, during a stress cycle [18]. The SIF can drive a fatigue crack to propagate only when it exceeds the critical value. The crack closure may result from the reversed plastic deformation in the plastic zone ahead of the crack tip, the surface roughness on the crack surface, and the buildup of oxides/corrosion products within the crack enclave [19]. The closure effect for a long crack can be significant (longer than a few mm). This effect declines and eventually disappears as the crack size is reduced [20]. Although a detailed description of crack closure mechanisms is beyond the scope of this work, the concept of crack closure is utilized.

Following McEvily's approach, to include the crack enclosure effect the real crack tip opening displacement can be expressed as follows [18]

$$\Delta\delta_{eff} = \Delta\delta - \Delta\delta_{th} \qquad \text{(2.D–2)}$$

where $\Delta\delta_{th}$ may be regarded as a constant characterizing the critical loading condition to open a long crack in the pipeline during service. The fatigue CGR will be arrested when $\Delta\delta$ is below $\Delta\delta_{th}$.

For a crack exposed to the high pH chemistry of pipelines, a long crack will stop growing when the crack tip strain rate is zero. Therefore, the CTSR is likely to be a function of a function of $\Delta\delta_{eff}$ instead of $\Delta\delta$ [18]. In that case, the CTSR is zero if $\Delta\delta_{eff} \leq 0$. This is to say that a long crack cannot propagate in the corrosive environment if the maximum SIF in a stress cycle follows $K_{max} \leq K_{ISCC}$ [21-22]. Therefore, the role of K_{ISCC} in SCC is quite similar to ΔK_{th} in fatigue crack growth. They both represent the resistance of material against the propagation of a long crack.

Based on the previous discussion, it may be reasonable to assume that $\Delta\delta_{eff}$ is proportional to $\Delta K^2 - \Delta K_{th}^2$ or $\Delta K^2 - \Delta K_{ISCC}^2$. By replacing ΔK^2 with $\Delta K^2 - \Delta K_{ISCC}^2$ and $\dot{\varepsilon}_{ct}$ with $\dot{\varepsilon}_{ct,eff}$, Equation (2.D–1) becomes

$$\dot{\varepsilon}_{ct,eff} = f\varepsilon_0(1-R)^2(K_{max}^2 - K_{ISCC}^2) \qquad (2.D–3)$$

where $\dot{\varepsilon}_{ct,eff}$ is defined as a crack tip strain rate corresponding to $K_{max}^2 - K_{ISCC}^2$.

Appendix 2.E—Effect Mass Transfer in Crack

The electrochemical reaction kinetics at the crack tip depends on the local solution chemistry. To understand the local solution chemistry evolution at the crack tip during crack propagation, a long crack exposed to 1N-1N carbonate-bicarbonate solution at 75 ^{o}C is numerically simulated by using the program originally developed by F.M. Song [4]. In the simulation, the Hall's equation is employed for CTSR calculation. In this concentrated, buffered solution, when the CGR is below 1×10^{-9}m/s (an upper bound CGR known for high pH SCC), very little potential drop within the crack is shown in Figure 2.E–1. The solution pH within the crack also shows a very small variation (Figure 2.E–2). Thus, in such a solution, the effect of mass transfer on CGR may be neglected.

When the anodic current density on the bare metal surface at crack tip can be estimated from the polarization curve measured by the fast potential scanning (1 V/min), Figure 2-3 shows the estimated crack velocities under sustained loading with and without considering mass transfer in the crack. The very small variation between the two conditions further suggests that mass transfer can be ignored.

Note that when the crack velocity exceeds 1×10^{-9} m/s or higher or when the solution is dilute, the variation within a crack may not be small. This is not often the condition recognized for high pH SCC. In these cases, the potential drop in crack can increase sharply with crack velocity and the solution chemistry will change significantly.

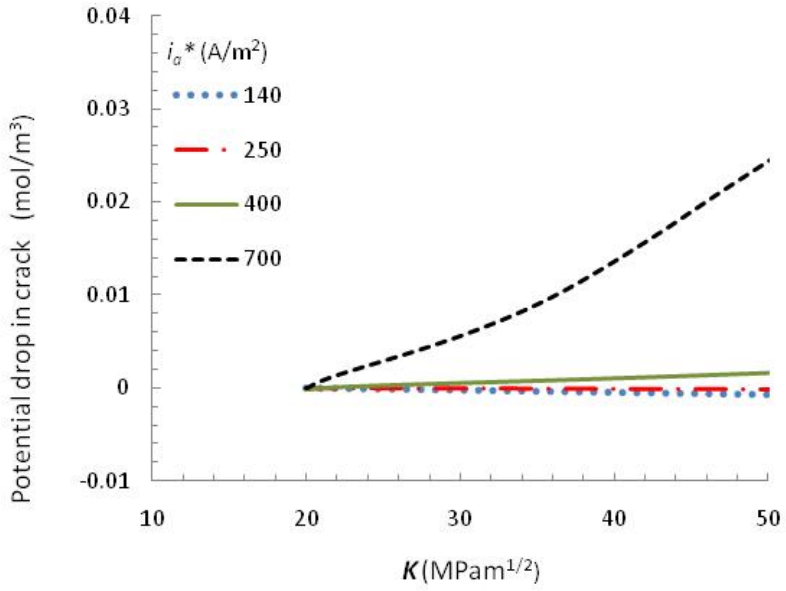

Figure 2.E–1. The Change of Potential During Crack Growth.

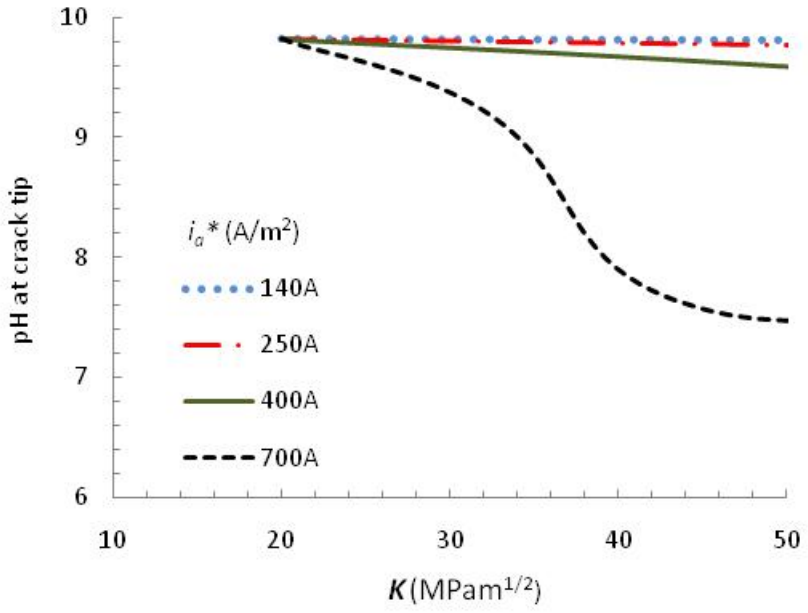

Figure 2.E-2. The Change of Local pH in Crack During Crack Growth.

APPENDIX 2.F—ANALYSIS OF EQUATION (2-13) VS. SUPERPOSITION MODEL

If used for the CGR model in this work under cyclic loading, the superposition model for corrosion fatigue may be written as

$$\dot{a} \approx \dot{a}_s + \dot{a}_c \tag{2.F–1}$$

where the overall CGR under cyclic loading $\dot{a}$ is approximated by sum of the CGR under constant loading $\dot{a}_s$ and the CGR due to loading fluctuation $\dot{a}_c$.

Substituting expressions of $\dot{a}$ with Equation (2-13), $\dot{a}_s$ with Equation (2-8), and $\dot{a}_c$ with Equation (2-11) to Equation (2.F–1)

$$\dot{a} = A(\dot{\varepsilon}_{cts}\frac{\dot{a}}{\dot{a}_s} + \dot{\varepsilon}_{ctc})^n = \dot{a}_s[\frac{\dot{a}}{\dot{a}_s} + \left(\frac{\dot{a}_c}{\dot{a}_s}\right)^{\frac{1}{n}}]^n \tag{2.F–2a}$$

where $\dot{\varepsilon}_{cts}$ and $\dot{\varepsilon}_{ctc}$ are the CTSRs under constant loading and loading fluctuation, respectively.

Equation (2.F–2a) can also be written as

$$\frac{\dot{a}_c}{\dot{a}_s} = [\left(\frac{\dot{a}}{\dot{a}_s}\right)^{\frac{1}{n}} - \frac{\dot{a}}{\dot{a}_s}]^n = (q^{\frac{1}{n}} - q)^n \tag{2.F–2b}$$

where $q = \frac{\dot{a}}{\dot{a}_s}$.

The error resulting from the approximation by Equation (2.F–1) may be defined by

$$\theta = (\frac{\dot{a}_s + \dot{a}_c}{\dot{a}} - 1) \times 100\% \tag{2.F–3}$$

Substitution of Equation (2.F–2b) into Equation (2.F–3) yields

$$\theta = \frac{1+(\dot{a}_c/\dot{a}_s)}{\dot{a}/\dot{a}_s} - 1 = \frac{1+(q^{\frac{1}{n}}-q)^n}{q} - 1 \tag{2.F–4}$$

The maximum error with the approximation of Equation (2.F–1) occurs at the maximum of θ, or θ_{max}. At θ_{max}, the following equation must be satisfied:

$$\left.\frac{d\theta}{dq}\right|_{\theta=\theta_{max}} = 0 \tag{2.F–5}$$

Substituting Equation (2.F–4) into Equation (2.F–5) and reorganization yields

$$(q^{\frac{1}{n}} - q)^{n-1}(q^{\frac{1}{n}} - nq) - (q^{\frac{1}{n}} - q)^n - 1 = 0 \tag{2.F–6}$$

Substituting the solution q_s into Equation (2.F–4) yields the expression of maximum error

$$\theta_{max} = \left(\frac{1+(q_s^{\frac{1}{n}} - q_s)^n}{q_s} - 1 \right) \times 100\% \qquad (2.F–7)$$

The maximum error depends only on the repassivation kinetic exponent "n." For a given n, the q at the maximum error can be calculated from Equation (2.F–6). With the calculated q, the corresponding maximum error can then be calculated from Equation (2.F–7). The result is shown in Figure 2.F–1. Two curves of maximum error are shown, which correspond to different signs of error as labeled. These two curves meet at n = 6.3 with the corresponding error being 7.2 percent. This is the minimum of the maximum errors from Equation (2.F–1) if ignoring the sign of error. The maximum errors regardless of the signs of error are shown by the two solid curves. At n = 0.667 the maximum error is 12.8 percent located in the intersection between the vertical line labeled by n = 2/3 and the solid curve. The maximum error at n = 0.8 is 39.1 percent and at n = 0.5 is 25.0 percent.

Figure 2.F–2 shows two solid curves on which the q values calculated from Equation (2.F–6) reside. Equation (2.F–6) has two valid solutions approximately between n = 0.55 and n=0.75. At n = 0.63, where the minimum of the maximum errors is shown in Figure 2.F–1, the two q values (1.15 and 8.21) are labeled as two empty squares. To the left of this vertical line at n = 0.63, the qs on the lower left solid curve give the maximum error. Conversely, to the right of the vertical line at n = 0.63, the qs on the upper-right solid curve yield the maximum negative error. Between these two solid curves is a curve with zero error. It is known from the error definition of Equation (2.F–4) that at q = 1 the error is also zero. Because the maximum error is positive on the lower left curve, the region sandwiched between these two zero-error lines (limited with n<0.75) is where the range of q values resides that gives positive error. When n≥0.75, the zero-error curve merges with the q = 1 line. The region where q yields a negative error is above this curve, and the maximum error is located at the upper right solid curve.

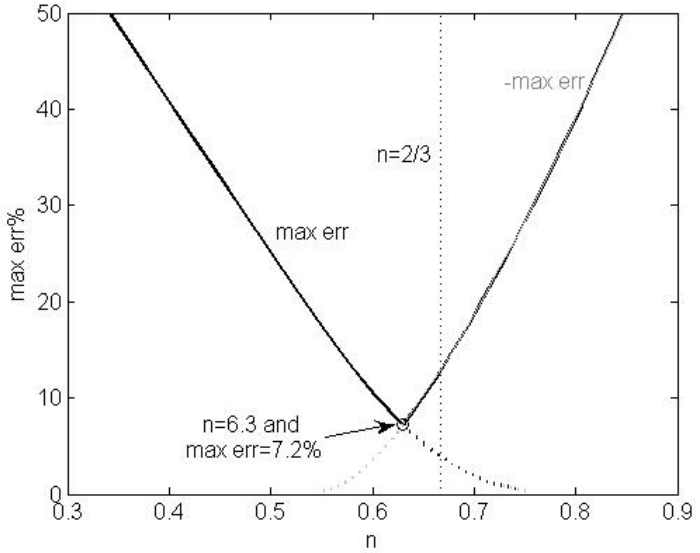

Figure 2.F–1. Maximum Errors at Different ns From Equation (2.F–1).

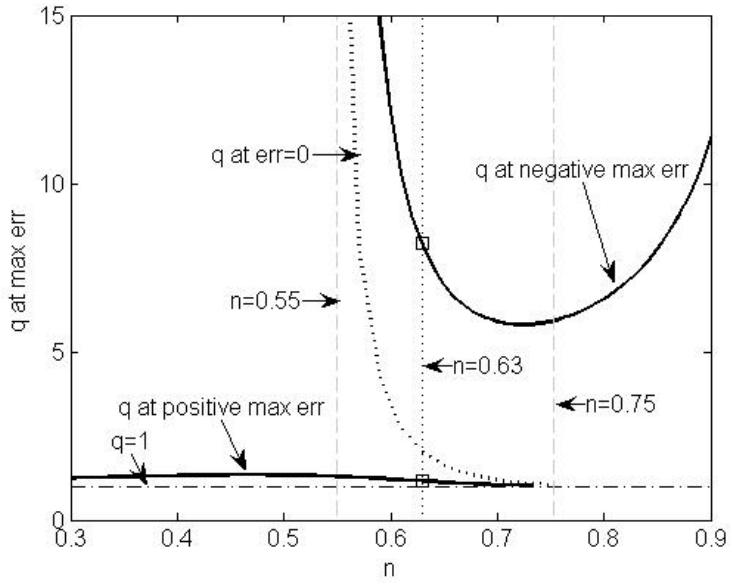

Figure 2.F–2. Calculated From Equation (2.F–6) q Values at Maximum Errors.

APPENDIX 3.A—ATOMIC HYDROGEN DISTRIBUTION IN STEEL

When crack growth is dominated by a hydrogen embrittlement mechanism, the atomic hydrogen concentration in the fracture process zone (FPZ) can play a significant role in the crack propagation process. Due to interactions between the near-tip stress field and the crystalline lattice expansion produced by atomic hydrogen, the hydrogen atoms tend to enrich in the FPZ ahead of the crack tip. The local atomic hydrogen concentration around a stationary crack tip is a function of hydrostatic stress following [14-15]

$$C_H = C_0 \exp\left(\frac{H_B+\sigma_h V_H}{RT}\right) \tag{3.A–1}$$

C_0 is diffusible hydrogen concentration in the lattice of bulk material, V_H is partial molar volume of the hydrogen atom in the material, R is universal gas constant, T is absolute temperature, and $\sigma_h = \frac{1}{3}\sum_{j=1}^{3}\sigma_{jj}$ is the local hydrostatic stress where σ_{jj} $(j = 1,2,3)$ are the principle stresses. The binding energy of hydrogen trap H_B can depend on the nature of the traps.

When defects in the steel are not considered, H_B=0. Equation (3.A–1) is reduced to

$$C_H^{Lat.} = C_0 \exp\left(\frac{\sigma_h V_H}{RT}\right) \tag{3.A–2}$$

where $C_H^{Lat.}$ is under stress hydrogen concentration in steel lattice.

Under cyclic loading, there is no accurate solution for the stress/strain field in the plastic zone. Following linear elastic fracture mechanics, the maximum local hydrostatic stress ahead of the crack tip can be expressed by the maximum SIF, K_{Imax}, or

$$\sigma_h = \frac{2}{3}(1+\nu)\frac{K_{Imax}}{\sqrt{2\pi r}} cos\frac{\theta}{2} \tag{3.A–3}$$

where ν is the Poisson's ratio (≈ 0.3) and r and θ are radius and angle, respectively, from the center of the FPZ.

In Equation (3.A–3), σ_h reaches maximum when $r = r_{FPZ}$ and when the crack propagates along the plane where the maximum tensile stress is applied, $\theta = 0$. This leads to

$$\sigma_h|_{r=r_{FPZ}} = \sigma_{h,max} = \frac{2}{3}(1+\nu)\frac{K_{Imax}}{\sqrt{2\pi r_{FPZ}}} \tag{3.A–4}$$

Substitute Equation (3.A–4) into Equation (3.A–2) to yield

$$\frac{C_{H.max}^{Lat.}}{C_0} = \exp\left(\frac{2(1+\nu)K_{Imax}V_H}{3RT\sqrt{2\pi r_{FPZ}}}\right) = \exp\left(\frac{\eta K_{Imax}}{RT\sqrt{r_{FPZ}}}\right) \tag{3.A–5}$$

where $C_{H.max}^{Lat.}$ is $C_H^{Lat.}$ at $r = r_{FPZ}$ and $\eta = \frac{2(1+\nu)V_H}{3\sqrt{2\pi}}$.

APPENDIX 4.A—A MORE DETAILED PROCEDURE FOR ESTIMATING HIGH pH CRACK GROWTH RATES UNDER CONSTANT LOAD

Under constant load, the CGR model, Equation (2-6), may be used for field application. To be conservative, it is assumed that $K_{ISCC} = 0$. Equation (2-6) becomes

$$\dot{a} = \lambda_0[ln(K^2) - ln(\lambda_1)]^{\lambda_2} = \lambda_0 P \tag{4.A–1}$$

where $\lambda_0 = A^{\frac{1}{1-n}}\left(\frac{2N}{N-1}\frac{\sigma_y}{Er_0}\right)^{\frac{n}{1-n}}$, $\lambda_1 = 3\pi r_0\sigma_y^2$, $\lambda_2 = \frac{N+1}{N-1}\frac{n}{1-n}$, and $P = [ln(K^2) - ln(\lambda_1)]^{\lambda_2}$.

In Equation (4.A–1), λ_2 depends on only material property and the film repassivation kinetics. Given the steel strain hardening exponent, $N \approx 6$, and the repassivation kinetic exponent, $n \approx 0.667$ (measured for pipeline steel in 1N-1N carbonate-bicarbonate solution at 75 °C), it is calculated that $\lambda_2 \approx 2.8$. P is a function of K and thus a function of crack depth "a."

In Equation (4.A–1), λ_0 and λ_1 are model parameters to be determined. They can be obtained from ILI runs. When the depth of a growing crack is measured to be a_j during the j^{th} ILI after the crack was first found to have a depth of a_1 during the first inspection, the SIF, K_j corresponding to a_j, can be calculated. The average CGR between two consecutive inspections, j^{th} and $(j+1)^{th}$, during the interval of

$$\Delta t_{j+1} = t_{j+1} - t_j \tag{4.A–2}$$

can be calculated by

$$\bar{\dot{a}}_{j+1} = \frac{a_{j+1}-a_j}{\Delta t_{j+1}} \tag{4.A–3}$$

Integration of Equation (4.A-1) between time t_j and t_{j+1} yields

$$\int_{a_j}^{a_{j+1}} P^{-1}da = \lambda_0\Delta t_{j+1} \tag{4.A–4}$$

Parameter λ_1 may be obtained by solving

$$\frac{\Delta t_{j+1}}{\Delta t_j} = \frac{\int_{a_j}^{a_{j+1}} P^{-1}da}{\int_{a_{j-1}}^{a_j} P^{-1}da} \tag{4.A–5a}$$

or it can be estimated by

$$\frac{\bar{\dot{a}}_{j+1}}{\bar{\dot{a}}_j} = \frac{P_j^{-1}+P_{j-1}^{-1}}{P_{j+1}^{-1}+P_j^{-1}} = \frac{P_{j+1}}{P_{j-1}}\cdot\frac{P_j+P_{j-1}}{P_{j+1}+P_j} \tag{4.A–5b}$$

Once λ_1 is obtained, λ_0 can be determined from either:

$$\lambda_0 = \frac{\int_{a_j}^{a_{j+1}} P^{-1} da}{\Delta t_{j+1}} \tag{4.A–6a}$$

or estimated from

$$\lambda_0 = 0.5\bar{\dot{a}}_{j+1}(P_{j+1}^{-1}+P_j^{-1}) \tag{4.A–6b}$$

With only two model variables, λ_0 and λ_1, a minimum of two ILI runs or two depths of a growing crack are required to estimate the values of these two variables. It is preferred that three depths of a growing crack are known to more reliably estimate two CGRs needed to determine λ_0 and λ_1.

These two scenarios associated with two or three ILI runs to obtain λ_0 and λ_1 are treated separately next.

4.A.1. Crack Depths of a Growing Crack Known From Three Consecutive ILI Runs

With three consecutive inspections, $\bar{\dot{a}}_2$ and $\bar{\dot{a}}_3$ can be calculated from Equation (4.A–3). Equations (4.A–5a) and (4.A–5b) become, respectively

$$\frac{\Delta t_3}{\Delta t_2} = \frac{\int_{a_2}^{a_3} P^{-1} da}{\int_{a_1}^{a_2} P^{-1} da} \tag{4.A–7a}$$

and

$$\frac{\bar{\dot{a}}_3}{\bar{\dot{a}}_2} = \frac{P_3}{P_1} \cdot \frac{P_2+P_1}{P_3+P_2} \tag{4.A–7b}$$

λ_1 can be calculated from Equation (4.A–7a) or (4.A–7b). λ_0 may be calculated from

$$\lambda_0 = \frac{\int_{a_2}^{a_3} P^{-1} da}{\Delta t_3} \tag{4.A–8a}$$

or estimated from

$$\lambda_0 = 0.5\bar{\dot{a}}_3(P_3^{-1}+P_2^{-1}) \tag{4.A–8b}$$

With λ_0 and λ_1, any instant CGR at a given crack depth can be calculated from Equation (4.A–1).

For a future time interval Δt_x, between t_3 (time of the third inspection) and a future time t_x the average CGR can be predicted by

$$\bar{\dot{a}}_x = \frac{a_x - a_3}{\Delta t_x} = \frac{a_x - a_3}{t_x - t_3} \tag{4.A–9}$$

where a_x is the future crack depth at t_x, to be determined. Because $\bar{\dot{a}}_x$ is related to K_x by

$$\frac{\Delta t_x}{\Delta t_3} = \frac{\int_{a_3}^{a_x} P^{-1} da}{\int_{a_2}^{a_3} P^{-1} da} \tag{4.A–10a}$$

or it can be estimated by

$$\frac{\bar{\dot{a}}_x}{\bar{\dot{a}}_3} = \frac{P_x}{P_2} \cdot \frac{P_3 + P_2}{P_x + P_3} \tag{4.A–10b}$$

the crack depth a_x can be calculated from Equation (4.A–10a) or (4.A–10b) through an iteration method.

Alternatively, given the maximum allowed crack depth $a_x = a_{max}$, the targeted failure time $t_x = t_f$ to reach that depth can be calculated from Equation (4.A–10a) or (4.A–10b) without the need of iteration.

When Equation (4.A–10b) is used to calculate t_f, K_x is calculated first followed by $\bar{\dot{a}}_x$. By substituting $\bar{\dot{a}}_x$ into Equation (4.A–9), t_x is obtained, or

$$t_f = t_x = \frac{a_{max} - a_3}{\bar{\dot{a}}_x} + t_3 \tag{4.A–7}$$

4.A.2. Crack Depths of a Growing Crack Known from Two Consecutive ILI Runs

When a crack found the first time has the maximum depth of a_1 and if the crack initiation time can be ignored, following the current industrial practice, the first average CGR may be estimated by

$$\bar{\dot{a}}_1 = \frac{a_1}{\Delta t_1} \tag{4.A–12}$$

where Δt_1 is the pipe age when the crack was found during the first inspection.

In this case, only a total of two ILIs are required to predict future CGR. From the second inspection with the crack depth given of a_2, the average CGR between the two ILI runs may be determined from

$$\bar{\dot{a}}_2 = \frac{a_2 - a_1}{\Delta t_2} \tag{4.A–13}$$

When the depth of the second ILI is used, Equation (4.A–4) may be written as

$$\int_{a_1}^{a_2} P^{-1} da = \lambda_0 \Delta t_2 \qquad (4.A–14a)$$

and Equation (4.A-14a) may be estimated by

$$\bar{\dot{a}}_2 = \lambda_0 \frac{2P_1P_2}{P_1+P_2} \qquad (4.A–14b)$$

Before the first ILI, integration of Equation (4.A–4) is not straightforward, with the lower integration limit being zero or unknown. Because the crack initiation time is generally believed to be longer than the time of crack growth, when Equation (4.A–4) is used for predicting the average CGR before the first ILI, it is still conservative even if it is assumed the average CGR is half or less than half of the instant CGR at the time of first ILI. Thus, the average CGR before the first ILI may be estimated from Equation (4.A–4) by

$$\bar{\dot{a}}_1 = \int_{a_0}^{a_1} P^{-1} da = \chi \cdot \dot{a}_1 = \chi \lambda_0 P_1 \qquad (4.A–15)$$

where a_0 is the crack size at the time of pipe commission and χ is equal to or greater than 0.5. For this project, it is taken as χ=0.5.

With $\lambda_0 = \Delta a_1/(\chi P_1 \Delta t_1)$ based on Equation (4.A–15), Equation (4.A–14a) becomes:

$$\int_{a_1}^{a_2} P^{-1} da = \Delta a_1 \Delta t_2/(\chi P_1 \Delta t_1) \qquad (4.A–16a)$$

Alternatively, the combination of Equations (4.A–14b) and (4.A–15) to eliminate λ_0 yields

$$\frac{\bar{\dot{a}}_2}{\bar{\dot{a}}_1} = \frac{2P_2}{\chi(P_1+P_2)} \qquad (4.A–16b)$$

λ_1 can be calculated from Equation (4.A–16a) or (4.A–16b), and λ_0 can then be calculated from Equation (4.A–14a) or (4.A–14b).

With λ_0 and λ_1, any future CGRs can be predicted. For instance, to predict the time of failure with the crack depth of a_f, the following equation may be used:

$$\frac{\bar{\dot{a}}_f}{\bar{\dot{a}}_2} = \frac{P_f}{P_1} \cdot \frac{P_2+P_1}{P_f+P_2} \qquad (4.A–17)$$

to calculate $\bar{\dot{a}}_f$ first followed by t_f.

4.A.3. Iteration Method to Calculate λ_1 From Equation (4.A–5)

4.A.3.1 Three ILI Data Available for a Growing Crack

Equation (4.A–5a) may be reorganized as

$$\Delta t_{j+1} \int_{a_{j-1}}^{a_j} P^{-1} da - \Delta t_j \int_{a_j}^{a_{j+1}} P^{-1} da = 0 \quad \text{(4.A–18a)}$$

Newton's downhill iteration method may be used to determine λ_1, and for that, Equation (4.A–18a) is rewritten as

$$f = \Delta t_{j+1} \int_{a_{j-1}}^{a_j} P^{-1} da - \Delta t_j \int_{a_j}^{a_{j+1}} P^{-1} da \quad \text{(4.A–19)}$$

and the derivative of f over λ_1 is

$$f'_{\lambda_1} = -\Delta t_{j+1} \int_{a_{j-1}}^{a_j} P^{-2} P'_{\lambda_1} da - \Delta t_j \int_{a_j}^{a_{j+1}} P^{-2} P'_{\lambda_1} da \quad \text{(4.A–20)}$$

where $P'_{\lambda_1} = -\frac{\lambda_2}{\lambda_1}[ln(K^2) - ln(\lambda_1)]^{\lambda_2 - 1} = -\frac{\lambda_2}{\lambda_1} P^{\frac{2-1}{2}}$.

The iteration equation to calculate λ_1 is written as

$$\lambda_1 = \lambda_1 - \frac{f}{f'_1} \quad \text{(4.A–21)}$$

Equation (4.A–5b) may be reorganized as:

$$\bar{a}_{j+1} P_{j-1}(P_{j+1} + P_j) - \bar{a}_j P_{j+1}(P_j + P_{j-1}) = 0 \quad \text{(4.A–22)}$$

To use Newton's downhill iteration method to calculate λ_1, Equation (4.A–22) is written as

$$f = \bar{a}_{j+1} P_{j-1}(P_{j+1} + P_j) - \bar{a}_j P_{j+1}(P_j + P_{j-1}) \quad \text{(4.A–23)}$$

and the derivative of f over λ_1 is

$$f'_{\lambda_1} = \bar{a}_{j+1}\left[P'_{\lambda_1,j-1}(P_{j+1} + P_j) + P_{j-1}(P'_{\lambda_1,j+1} + P'_{\lambda_1,j})\right] - \bar{a}_j\left[P'_{\lambda_1,j+1}(P_j + P_{j-1}) + P_{j+1}(P'_{\lambda_1,j} + P'_{\lambda_1,j-1})\right] \quad \text{(4.A–24)}$$

4.A.3.2 Two ILI Data Available for a Growing Crack

Equation (4.A–16a) may be reorganized as

$$\chi\Delta t_1 \int_{a_1}^{a_2} P^{-1} da - \Delta a_1 \Delta t_2 P_1^{-1} = 0 \qquad (4.A–25)$$

To use Newton's downhill iteration method to determine λ_1, Equation (4.A–25) is rewritten as

$$f = \chi\Delta t_1 \int_{a_1}^{a_2} P^{-1} da - \Delta a_1 \Delta t_2 P_1^{-1} \qquad (4.A–26)$$

and the derivative of f over λ_1 is

$$f'_{\lambda_1} = -\chi\Delta t_1 \int_{a_{j-1}}^{a_j} P^{-2} P'_{\lambda_1} da + \Delta a_1 \Delta t_2 P_1^{-2} P'_{\lambda_1,1} \qquad (4.A–27)$$

where $P'_{\lambda_1,1} = -\frac{\lambda_2}{\lambda_1}[ln(K_1^2) - ln(\lambda_1)]^{\lambda_2 - 1} = -\frac{\lambda_2}{\lambda_1} P_1^{\frac{2^{-1}}{2}}$.

An iteration equation such as Equation (4.A–21) may be used to determine λ_1.

Equation (4.A–16b) may be reorganized as

$$\chi(P_2 + P_1)\bar{a}_2 - 2P_2\bar{a}_1 = 0 \qquad (4.A–28)$$

To use Newton's iteration method to calculate λ_1, Equation (4.A-28) is written as

$$f = \chi(P_2 + P_1)\bar{a}_2 - 2P_2\bar{a}_1 \qquad (4.A–29)$$

and the derivative of f over λ_1 is

$$f'_{\lambda_1} = \chi\bar{a}_2(P'_{\lambda_1,2} + P'_{\lambda_1,1}) - 2\bar{a}_1 P'_{\lambda_1,2} \qquad (4.A–30)$$

4.A.4. Optimization to Determine λ_0 and λ_1 with Data of Multiple ILI Runs

When data of more than three ILI runs are available, the number of equations to solve for λ_0 and λ_1 is greater than the number of variables. The optimization method may be used to determine λ_0 and λ_1. For the optimization, Equation (4.A–4) may be used and the sum of all squared differences between the predicted Δt_{j+1} and the actual Δt^*_{j+1} should be minimized. The equation of optimization may be written as

$$S = \min\left[\sum_1^n \left(\Delta t_{j+1} - \Delta t^*_{j+1}\right)^2\right] = \min\left\{\sum_1^n \left[\lambda_0^{-1} \int_{a_j}^{a_{j+1}} P^{-1} da - \Delta t^*_{j+1}\right]^2\right\} \qquad (4.A–31)$$

For Equation (4.A-31), the derivatives of S over λ_0 and λ_1 should be set as zero respectively, which yield

$$\sum_1^n \left\{ \int_{a_j}^{a_{j+1}} P^{-1} da \left[\lambda_0^{-1} \int_{a_j}^{a_{j+1}} P^{-1} da - \Delta t_{j+1}^* \right] \right\} = 0 \qquad \text{(4.A–32a)}$$

$$\sum_1^n \left\{ \int_{a_j}^{a_{j+1}} P^{-2} P'_{\lambda_1} da \left[\lambda_0^{-1} \int_{a_j}^{a_{j+1}} P^{-1} da - \Delta t_{j+1}^* \right] \right\} = 0 \qquad \text{(4.A–32b)}$$

Reorganization of Equations (4.A-32a) and (4.A-32b) yields

$$\lambda_0^{-1} \sum_1^n \left(\int_{a_j}^{a_{j+1}} P^{-1} da \right)^2 - \sum_1^n \left(\Delta t_{j+1}^* \int_{a_j}^{a_{j+1}} P^{-1} da \right) = 0 \qquad \text{(4.A–33a)}$$

$$\lambda_0^{-1} \sum_1^n \left(\int_{a_j}^{a_{j+1}} P^{-1} da \right) \left(\int_{a_j}^{a_{j+1}} P^{-2} P'_{\lambda_1} da \right)$$

$$- \sum_1^n \left(\Delta t_{j+1}^* \int_{a_j}^{a_{j+1}} P^{-2} P'_{\lambda_1} da \right) = 0 \qquad \text{(4.A–33b)}$$

By eliminating λ_0 from Equations (4.A–33a) and (4.A–33b), λ_1 may be determined by an iteration method from

$$\frac{\sum_1^n \left(\Delta t_{j+1}^* \int_{a_j}^{a_{j+1}} P^{-1} da \right)}{\sum_1^n \left(\int_{a_j}^{a_{j+1}} P^{-1} da \right)^2} - \frac{\sum_1^n \left(\Delta t_{j+1}^* \int_{a_j}^{a_{j+1}} P^{-2} P'_1 da \right)}{\sum_1^n \left[\left(\int_{a_j}^{a_{j+1}} P^{-1} da \right) \left(\int_{a_j}^{a_{j+1}} P^{-2} P'_1 da \right) \right]} = 0 \qquad \text{(4.A–34)}$$

Once λ_1 is determined, λ_0 can then be obtained from either Equation (4.A–33a) or (4.A–33b).

Alternatively, λ_0 and λ_1 may be determined by using Equation (4.A–4) and by making the total of the squared difference between the reciprocal of predicted $\bar{a}_{j+1}$ and that of the actual $\bar{a}_{j+1}$ be minimum, which yields:

$$S = \min \left[\sum_1^n \left(\frac{1}{\bar{a}_{j+1}} - \frac{1}{\bar{a}_{j+1}^*} \right)^2 \right] = \min \left\{ \sum_1^n \left[0.5 \lambda_0^{-1} (P_{j+1}^{-1} + P_j^{-1}) - \frac{1}{\bar{a}_{j+1}^*} \right]^2 \right\} \qquad \text{(4.A–35)}$$

By taking the derivatives of S over λ_0 and λ_1 to be zero,

$$\sum_1^n \left\{ (P_{j+1}^{-1} + P_j^{-1}) \left[0.5 \lambda_0^{-1} (P_{j+1}^{-1} + P_j^{-1}) - \frac{1}{\bar{a}_{j+1}^*} \right] \right\} = 0 \qquad \text{(4.A–36a)}$$

$$\sum_1^n \left\{ (P_{j+1}^{-2} P'_{\lambda_1, j+1} + P_j^{-2} P'_{\lambda_1, j}) \left[0.5 \lambda_0^{-1} (P_{j+1}^{-1} + P_j^{-1}) - \frac{1}{\bar{a}_{j+1}^*} \right] \right\} = 0 \qquad \text{(4.A–36b)}$$

By eliminating λ_0 from the Equations (4.A-36a) and (4.A-36b), λ_1 can be obtained from

$$\frac{\Sigma_1^n\left[\frac{1}{\bar{a}^*_{j+1}}(P_{j+1}^{-1}+P_j^{-1})\right]}{\Sigma_1^n\left(P_{j+1}^{-1}+P_j^{-1}\right)^2}-\frac{\Sigma_1^n\left[\frac{1}{\bar{a}^*_{j+1}}(P_{j+1}^{-2}P'_{1,j+1}+P_j^{-2}P'_{1,j})\right]}{\Sigma_1^n\left[(P_{j+1}^{-1}+P_j^{-1})(P_{j+1}^{-2}P'_{1,j+1}+P_j^{-2}P'_{1,j})\right]}=0 \qquad (4.A\text{–}34)$$

Once λ_1 is determined, λ_0 can then be obtained from either Equation (4.A–36a) or (4.A–36b).

Appendix 4.B—A Procedure Using Average Operating Conditions To Estimate High pH Crack Growth Rates Under Cyclic Loading

When the fluctuation of cyclic loading controls CGR, the CGR model or Equation (2-11), may be used to predict field CGRs. To be conservative, it is assumed $K_{ISCC} = 0$ and Equation (2-11) becomes

$$\dot{a} = \frac{da}{dt} = \beta \xi^n K_{max}^{2n} \tag{4.B–1}$$

where $\beta = A\varepsilon_0^n$ is a constant and $\xi = f(1-R)^2$.

Given two arbitrary depths of a crack: a_i and a_{i+1} within a time interval between t_i and t_{i+1}, the averaged CGR can be calculated by:

$$\bar{\dot{a}}_{i+1} = \frac{a_{i+1} - a_i}{t_{i+1} - t_i} \tag{4.B–2}$$

Because K_{max} is a function of crack depth "a," when integration is performed for an arbitrary time interval from t_i to t_{i+1} with the corresponding crack depth from a_i to a_{i+1}, Equation (4.B–1) may be rearranged as

$$\int_{a_i}^{a_{i+1}} K_{max}^{-2n}\, da = \beta \int_{t_i}^{t_{i+1}} \xi^n\, dt = \beta \sum_{k=1}^{N_{i+1}} f_{i+1,k}^{-1} \xi_{i+1,k}^n \tag{4.B–3a}$$

where N_{i+1} is the total number of pressure cycles between t_i and t_{i+1}, and the subscripts "i+1" and "k" at the lower right position of f and ξ signal these two variables confined between the i^{th} and $(i+1)^{th}$ ILIs and the k^{th} cycle, respectively.

Equation (4.B-3a) may be estimated by

$$0.5 \Delta a_{i+1} (K_{max,i+1}^{-2n} + K_{max,i}^{-2n}) = \beta \sum_{k=1}^{N_{i+1}} f_{i+1,k}^{-1} \xi_{i+1,k}^n \tag{4.B–3b}$$

The time interval between t_i and t_{i+1} is related to frequency by

$$t_{i+1} - t_i = \sum_{k=1}^{N_{i+1}} f_k^{-1}. \tag{4.B–3c}$$

It requires at least two crack depths to estimate the constant β in Equation (4.B–3). Depending on the availability of detailed pressure fluctuations, different methods can be used to predict future CGRs.

4.B.1. Detailed Loading Frequency and Stress Ratio Available

Assume the detailed real-time internal pressure fluctuation is known between two ILIs and the crack depths were detected to be a_1 and a_2, respectively. Given the age of the pipe at the first two ILIs, t_1 and t_2, the average CGR can be calculated by

$$\bar{\dot{a}}_2 = \frac{\Delta a_2}{\Delta t_2} = \frac{a_2 - a_1}{t_2 - t_1} \tag{4.B–4}$$

where $\Delta a_2 = a_2 - a_1$ and $\Delta t_2 = t_2 - t_1$.

The constant β in Equation (4.B–3a) or (4.B–3b) can be calculated by

$$\beta = \frac{\int_{a_1}^{a_2} K_{max}^{-2n} da}{\sum_{k=1}^{N_2} f_{2,k}^{-1} \xi_{2,k}^{n}} \tag{4.B–5a}$$

where N_2 is the total number of pressure cycles between the two ILI runs.

Equation (4.B-5a) requires the integration of $K_{max,2}^{-2n}$ between a_1 and a_2. Even though this integration can easily be accomplished, to avoid direct integration Equation (4.B-5a) may be approximated by:

$$\beta = \frac{\Delta a_2 (K_{max,2}^{-2n} + K_{max,1}^{-2n})}{2 \sum_{k=1}^{N_2} f_{2,k}^{-1} \xi_{2,k}^{n}} \tag{4.B–5b}$$

Once "β" is known, the instant CGR at the k^{th} cycle can be estimated by:

$$\dot{a}_{2,k} = \beta \xi_{2,k}^{n} K_{max,k}^{2n} \tag{4.B–6}$$

Because the total time between the first ILI run and the j^{th} stress cycle is:

$$\Delta t_{2,j} = \sum_{k=1}^{j} f_{2,k}^{-1} \tag{4.B–7}$$

the average CGR during the first k cycles after the first ILI is:

$$\bar{\dot{a}}_{2,j} = \frac{a_{2,j} - a_1}{\Delta t_{2,j}} \tag{4.B–8}$$

where $a_{2,j}$ may be calculated from either

$$\int_{a_1}^{a_{2,j}} K_{max}^{-2n} \, da = \beta \sum_{k=1}^{j} f_{2,k}^{-1} \xi_{2,k}^{n} \tag{4.B–9a}$$

or

$$K_{max,2,j}^{-2n} = -K_{max,1}^{-2n} + \frac{2\beta\sum_{k=1}^{j} f_{2,k}^{-1}\xi_{2,k}^{n}}{\Delta a_{2,j}} \quad (4.B–9b)$$

When the third ILI has to be performed when the crack size reaches a_3, the total stress cycle after the second ILI, N_3, may be determined from either

$$\int_{a_2}^{a_3} K_{max}^{-2n}\, da = \beta\sum_{k=1}^{N_3} f_{3,k}^{-1}\xi_{3,k}^{n} \quad (4.B–10a)$$

or

$$K_{max,3}^{-2n} = -K_{max,2}^{-2n} + \frac{2\beta\sum_{k=1}^{N_3} f_{3,k}^{-1}\xi_{3,k}^{n}}{\Delta a_3} \quad (4.B–10b)$$

With N_3, the time scheduled for the third ILI can be estimated by:

$$t_3 = t_2 + \sum_{k=1}^{N_3} f_{3,k}^{-1} \quad (4.B–11)$$

where t_2 and t_3 are the pipe ages at the second and third ILI runs, respectively.

The average CGR between the second and third ILIs is

$$\bar{\dot{a}}_3 = \frac{\Delta a_3}{\Delta t_3} = \frac{a_3 - a_2}{t_3 - t_2} \quad (4.B–12)$$

At the j^{th} stress cycle, the time interval since the second ILI is:

$$\Delta t_{3,j} = \sum_{k=1}^{j} f_{3,k}^{-1} \quad (4.B–13)$$

The crack depth at the j^{th} stress cycle, $a_{3,j}$, may be estimated from either

$$\int_{a_2}^{a_{3,j}} K_{max}^{-2n}\, da = \beta\sum_{k=1}^{j} f_{3,k}^{-1}\xi_{3,k}^{n} \quad (4.B–14a)$$

or

$$K_{max,3,j}^{-2n} = -K_{max,2}^{-2n} + \frac{2\beta\sum_{k=1}^{N_3} f_{3,k}^{-1}\xi_{3,k}^{n}}{\Delta a_{3,j}} \quad (4.B–14b)$$

the average CGR during the k cycles after the second ILI is

$$\bar{\dot{a}}_{3,j} = \frac{a_{3,j} - a_2}{\Delta t_{3,j}} \quad (4.B–15)$$

The instant CGR at the j[th] stress cycle since the second ILI is

$$\dot{a}_{3,j} = \beta \xi_{3,i}^{n} K_{max,i}^{2n} \tag{4.B–16}$$

4.B.2 Constant Loading Frequency and Stress Ratio

When the variation over time of the loading frequency and stress ratio can be treated as constants, such as between the second and third ILI runs, Equation (4.B–10) may be written as:

$$\int_{a_2}^{a_3} K_{max}^{-2n}\, da = \beta N_3 f_3^{-1} \xi_3^{n} \tag{4.B–17a}$$

or

$$K_{max,3}^{-2n} = -K_{max,2}^{-2n} + \frac{2\beta N_3 f_3^{-1} \xi_3^{n}}{\Delta a_3} \tag{4.B–17b}$$

Either one of the previous two equations provides a unique relation between the crack depth at the third ILI, a_3, and the total stress cycle between the second and the third ILIs, N_3. Given the value of one variable, the other variable can be computed.

For instance, given the crack depth at the third ILI, N_3 can be determined, and the time interval between the second and third ILI can be calculated to be:

$$\Delta t_3 = N_3 f_3^{-1} \tag{4.B–18}$$

The averaged CGR can be determined from Equation (4.B–12).

If N_3, the total stress cycles between the second and third ILIs, is given, the time interval between the second and third ILIs can be calculated from Equation (4.B-18), and the crack depth at the third ILI can be calculated from Equation (4.B-17a) or (4.B-17b).

4.B.2. Optimization to Determine β in Equation (4.B-1)

When more than two ILIs are performed, the constant β in Equation (4.B–3a) or (4.B–3b) may be better determined from optimization by using all three crack depths from ILIs. For a total of m inspections, the following condition needs to be satisfied for optimization:

$$S = \min \left(\sum_{i=1}^{m} \left(\int_{a_i}^{a_{i+1}} K_{max}^{-2n}\, da - \beta \sum_{k=1}^{N_{i+1}} f_{i+1,k}^{-1} \xi_{i+1,k}^{n} \right)^2 \right. \tag{4.B–19a}$$

or

$$S = \min \left(\sum_{i=1}^{m} \left(0.5(K_{max,i+1}^{-2n} + K_{max,i}^{-2n}) \Delta a_{i+1} - \beta \sum_{k=1}^{N_{i+1}} f_{i+1,k}^{-1} \xi_{i+1,k}^{n} \right)^2 \right. \tag{4.B–19b}$$

The constant β in the previous equation may be calculated from

$$\beta = \frac{\sum_{i=1}^{m}\left[\left(\int_{a_i}^{a_{i+1}} K_{max}^{-2n} da\right)\cdot \sum_{k=1}^{N_{i+1}} f_{i+1,k}^{-1}\xi_{i+1,k}^{n}\right]}{\sum_{i=1}^{m}\left(\sum_{k=1}^{N_{i+1}} f_{i+1,k}^{-1}\xi_{i+1,k}^{n}\right)^{2}} \qquad \text{(4.B–20a)}$$

or

$$\beta = \frac{\sum_{i=1}^{m}\left[0.5\Delta a_{i+1}(K_{max,i+1}^{-2n}+K_{max,i}^{-2n})\cdot \sum_{k=1}^{N_{i+1}} f_{i+1,k}^{-1}\xi_{i+1,k}^{n}\right]}{\sum_{i=1}^{m}\left(\sum_{k=1}^{N_{i+1}} f_{i+1,k}^{-1}\xi_{i+1,k}^{n}\right)^{2}} \qquad \text{(4.B–20b)}$$